THE INFLUENCE OF ADDITIVE MANUFACTURING PROCESS PARAMETERS ON RESIDUAL STRESS OF 17-4 PH STAINLESS STEEL PARTS MANUFACTURED BY LASER POWDER BED FUSION ADDITIVE MANUFACTURING SYSTEM

A THESIS SUBMITTED TO
THE GRADUATE SCHOOL OF NATURAL AND APPLIED SCIENCES
OF
MIDDLE EAST TECHNICAL UNIVERSITY

BY

GÖKHAN ÇELİK

IN PARTIAL FULFILLMENT OF THE REQUIREMENTS
FOR
THE DEGREE OF MASTER OF SCIENCE
IN
METALLURGICAL AND MATERIALS ENGINEERING

JANUARY 2023

Approval of the thesis:

THE INFLUENCE OF ADDITIVE MANUFACTURING PROCESS PARAMETERS ON RESIDUAL STRESS OF 17-4 PH STAINLESS STEEL PARTS MANUFACTURED BY LASER POWDER BED FUSION ADDITIVE MANUFACTURING SYSTEM

submitted by **GÖKHAN ÇELİK** in partial fulfillment of the requirements for the degree of **Master of Science** i**n Metallurgical and Materials Engineering, Middle East Technical University** by,

Prof. Dr. Halil Kalıpçılar
Dean, Graduate School of **Natural and Applied Sciences** _____

Prof. Dr. Ali Kalkanlı
Head of the Department, **Metallurgical and Materials Eng.** _____

Prof. Dr. C. Hakan Gür
Supervisor, **Metallurgical and Materials Eng., METU** _____

Assoc. Prof. Dr. Caner Şimşir
Co-Supervisor, **Metallurgical and Materials Eng., METU** _____

Examining Committee Members:

Prof. Dr. Rıza Gürbüz
Metallurgical and Materials Eng., METU _____

Prof. Dr. C. Hakan Gür
Metallurgical and Materials Eng., METU _____

Prof. Dr. Oğuzhan Yılmaz
Mechanical Eng., Gazi Uni. _____

Assoc. Prof. Dr. Caner Şimşir
Metallurgical and Materials Eng., METU _____

Assist. Prof. Dr. Eda Aydoğan Güngör
Metallurgical and Materials Eng., METU _____

Date: 16.01.2023

I hereby declare that all information in this document has been obtained and presented in accordance with academic rules and ethical conduct. I also declare that, as required by these rules and conduct, I have fully cited and referenced all material and results that are not original to this work.

Name Last name : Gökhan Çelik

Signature :

ABSTRACT

THE INFLUENCE OF ADDITIVE MANUFACTURING PROCESS PARAMETERS ON RESIDUAL STRESS OF 17-4 PH STAINLESS STEEL PARTS MANUFACTURED BY LASER POWDER BED FUSION ADDITIVE MANUFACTURING SYSTEM

Çelik, Gökhan
Master of Science, Metallurgical and Materials Engineering
Supervisor: Prof. Dr. C. Hakan Gür
Co-Supervisor: Assoc. Prof. Dr. Caner Şimşir

January 2023, 162 pages

Laser Powder Bed Fusion (LPBF) process is one of the most well-known additive manufacturing methods for the production of complex and functional parts from metal powder material. Residual stresses cause a major setback in the LPBF process and restrict the serviceability of the parts, particularly in advanced technology applications. Process parameters have a crucial impact on residual stress formation and residual stresses alter the reliability of material properties. Therefore, the influence of process parameters on residual stresses needed to be investigated to provide more accurate mechanical properties for design and production optimization for the LPBF process.

17-4 PH stainless steel is desirable among the stainless steels for various fields, including aerospace, aviation, energy, and chemical industries, due to their superior high strength, hardness, and corrosion properties. Moreover, 17-4 PH stainless steels are easily machinable at solution heat treated condition. Their high weldability with high corrosion resistance properties makes them very attractive for industries.

The process parameters' effect on surface residual stresses could be performed by XRD residual stress measurement method which is very sensitive to surface and subsurface residual stresses. Residual stress specimens produced by LPBF process in as built condition had more than fifty times surface residual stresses compared to the conventionally produced bar specimens which indicated the importance of the investigation of surface residual stresses of LPBF parts.

In this thesis; the influence of scanning strategies, laser power, exposure time, volumetric energy density, hatch distance, point distance, layer thickness, preheating of the baseplate, and separation from the base plate were analyzed for 17-4 Precipitation Hardened (PH) stainless steel parts manufactured by LPBF additive manufacturing system in terms of residual stress accumulation on the surface and close to the very surface region by X-Ray Diffraction (XRD) method. The analyses show that, volumetric energy density (VED), laser power, and exposure time optimization played a crucial role in residual stress minimization. VED parameter optimization was crucial for overall penetration and surface residual stress formation on material. High laser power and less exposure time within the defined parameter range and specified VED value could be the optimum process parameter in terms of residual stress accumulation on the surface of a material. On the other hand, point distance and hatch distance had a slight influence when compared with the effect of volumetric energy density, laser power, and exposure time within the defined ranges. The as built parts' residual stresses could be reduced by up to ~67%. However, the tensile strength and yield strength of a material could also be decreased by 14% and 12%, respectively. Therefore, from an engineering standpoint, a trade-off between lower surface residual stress values and mechanical strength shall be taken into account.

Keywords: Residual Stress, Additive Manufacturing, Laser Powder Bed Fusion, 17-4 PH Stainless Steel

ÖZ

SEÇİCİ LAZER TOZ YATAĞI EKLEMELİ İMALAT YÖNTEMİ İLE ÜRETİLMİŞ 17-4 PH PASLANMAZ ÇELİĞİNDE EKLEMELİ İMALAT PROSES PARAMETRELERİNİN KALINTI GERİLİMLER ETKİSİ

Çelik, Gökhan
Yüksek Lisans, Metalurji ve Malzeme Mühendisliği
Tez Yöneticisi: Prof. Dr. C. Hakan Gür
Ortak Tez Yöneticisi: Doç. Dr. Caner Şimşir

Ocak 2023, 162 sayfa

Lazer Toz Yatak Füzyon (LTYF) prosesi, metal toz malzemeden, karmaşık ve fonksiyonel parçaların üretimi için en iyi bilinen eklemeli üretim yöntemlerinden biridir. Parça üzerinde oluşan kalıntı gerilimleri, LTYF prosesine engel oluşturmakta ve özellikle ileri teknoloji uygulamalarında parçaların kullanılabilmesini kısıtlayabilmektedir. Eklemeli imalat prosesinde, proses parametrelerinin kalıntı gerilimleri üzerine önemli etkisi vardır ve kalıntı gerilimleri malzeme özelliklerinin güvenilirliğini değiştirmektedir. Bu sebeple, tasarım ve üretimde güvenilir mekanik özellikler sağlamak için LTYF prosesinde, proses parametrelerinin kalıntı gerilimleri üzerindeki etkilerinin araştırılması gerekmektedir.

17-4 PH paslanmaz çelik malzemeler, üstün yüksek mukavemet, sertlik ve korozyon dayanım özelliklerinden dolayı uzay, havacılık, enerji ve kimya endüstrileri de dahil olmak üzere çeşitli alanlarda, paslanmaz çelik malzemeler arasında tercih edilmektedir. Ayrıca, 17-4 PH paslanmaz çelikler, çözeltiye alma ısıl işlemi görmüş durumda kolayca işlenebilir. Bu çeliklerin yüksek kaynaklanabilirlik ve korozyon direncine sahip olması, onları endüstride kullanımını cazip kılmaktadır.

Proses parametrelerinin yüzey kalıntı gerilimlerine etkisi, yüzey ve yüzey altı kalıntı gerilimlerine karşı çok hassas olan XRD kalıntı gerilim ölçüm yöntemi ile analiz edilebilir. LTYF prosesiyle üretilen kalıntı gerilimlerinin, geleneksel yöntemlerle üretilmiş olan çubuk malzemeye kıyasla elli kat fazla olması, LTYF ile üretilen parçalarda kalıntı gerilimi araştırılmasının önemini göstermiştir.

Bu tezde; tarama stratejilerinin etkisi, lazer gücü, maruz kalma süresi, hacimsel enerji yoğunluğu, tarama mesafesi, nokta atış mesafesi, katman kalınlığı, alt plakanın ön ısıtması, alt plakadan ayrılma etkisi, LTYF eklemeli imalat yöntemi ile üretilen 17-4 PH paslanmaz çelikleri ile yüzeyde ve çok yüzeye yakın bölgede kalıntı gerilimi birikimi açısından X Işını Kırınım (XRD) yöntemi ile analiz edilmiştir. Analizler, hacimsel enerji yoğunluğunun (HEY), lazer gücünün ve maruz kalma süresi optimizasyonunun kalıntı gerilimin en aza indirilmesinde çok önemli bir rol oynadığını göstermektedir. HEY parametre optimizasyonu, malzeme üzerinde genel penetrasyon ve yüzey kalıntı gerilimi oluşumunda oldukça önemlidir. Tanımlanan parametre aralığı ve belirtilen HEY değeri dahilinde yüksek lazer gücü ve daha az maruz kalma süresi, bir malzemenin yüzeyinde kalıntı gerilimi birikimi açısından optimum işlem parametresi olabilmektedir. Öte yandan, tanımlanmış aralıklar içinde nokta atış mesafesi ve tarama mesafesinin; hacimsel enerji yoğunluğu, lazer gücü ve maruz kalma süresinin etkisine kıyasla daha az bir etkiye sahip olduğu görülmektedir. Üretilen parçalarda proses parametre optimizasyonuyla kalıntı gerilimlerinin ~%67'ye kadar azaltılabileceği ancak, malzemenin çekme ve akma mukavemetinde sırasıyla %14 ve %12'e kadar düşüş yaşanabileceği görülmüştür. Bu nedenle, mühendislik açısından, yüzey kalıntı gerilim değerleri ile mekanik dayanım arasındaki denge dikkate alınmalıdır.

Anahtar Kelimeler: Kalıntı Gerilimi, Eklemeli İmalat, Lazer Toz Yatak Füzyon, 17-4 PH Paslanmaz Çelik

To my beloved and supportive family

ACKNOWLEDGMENTS

I would like to express my deepest gratitude to my thesis supervisor Prof. Dr. C. Hakan Gür for his guidance, valuable feedback, and encouragement throughout this research in all circumstances.

I am grateful to my co-supervisor Assoc. Prof. Dr. Caner Şimşir for his guidance with precious ideas, valuable feedback, constructive criticism, and support throughout this work. I would not have completed this thesis without his support.

I would like to express my sincere thanks to Assist. Prof. Dr. Evren Yasa for her valuable suggestions and comments throughout this research.

I am much obliged to my dear managers Olcay Elmalı Meço and Orkun Umur Önem for their encouragement and support for the realization of this thesis.

I wish to state my deepest appreciation to my supportive colleagues, Mertcan Başkan, Yusuf Alptuğ Polat, Erkan Buğra Türeyen, Tansu Göynük, Andaç Özsoy, Can İhsan Tekinbaş and Ece Kahraman Ulaş for their discussion on characterization, valuable friendship and wonderful companionship throughout this research.

The technical assistance of Yahya Tunç, Hüseyin Ayaş, Ahmet Kösem, and Fatih Altunsaray is gratefully acknowledged.

I would like to thank my friends, Bold Union for their encouragement to finish this thesis.

Finally, I owe deep gratitude to my beloved family who has always supported me throughout my life.

TABLE OF CONTENTS

LIST OF TABLES

TABLES

LIST OF FIGURES

FIGURES

LIST OF ABBREVIATIONS

ABBREVIATIONS	
AISI	American Iron and Steel Institute
AM	Additive Manufacturing
BCC	Body Centered Cubic
BJT	Binder Jetting
CAD	Computer Aided Design
CCW	Counter Clockwise
CMM	Coordinate Measuring Machine
CW	Continues-Wave
DED	Directed Energy Deposition
DMLS	Direct Metal Laser Sintering
DOE	Design of Experiment
EDM	Electric Discharge Machining
EDS	Energy Dispersive Spectroscopy
ET	Exposure Time
FPI	Fluorescent Penetrant Inspection
FWHM	Full-Width Half Maximum
HD	Hatch Distance
HIP	Hot Isostatic Pressing
HV	Vickers Hardness
LOM	Light Optical Microscopy
LPBF	Laser Powder Bed Fusion
LT	Layer Thickness
MEX	Material Extrusion
MJT	Material Jetting
NDT	Non-Destructive Testing
OES	Optical Emission Spectrometer

P	Power (Laser Power)
PBF	Powder Bed Fusion
PD	Point Distance
PH	Precipitation Hardening
PW	Pulsed Wave
RS	Residual Stress
RT	Room Temperature
SEM	Scanning Electron Microscope
SHL	Sheet Lamination
SLM	Selective Laser Melting
VED	Volumetric Energy Density
VPP	Vat Photopolymerization
XRD	X-Ray Diffraction

LIST OF SYMBOLS

SYMBOLS

d	Spacing between the lattice planes in the crystal
E	Modulus of Elasticity [GPa]
M_s	Martensite start temperature [°C]
α	Ferritic
α'	Martensitic
γ	Austenitic
δ	delta
θ	Angle between the incident beam and diffracting planes and also called Bragg angle
λ	X-Ray wavelength
V_T	Shear (transverse) velocity
V_L	Longitudinal Velocity
σ	Stress [MPa]
ρ	Density
ν	Poisson's Ratio

CHAPTER 1

INTRODUCTION

Determining stresses is crucial for a design of a component or assembly and the prediction of the lifetime of a part from an engineering perspective. Analyzing standalone external forces is usually insufficient for stress calculations on material for the reliable mechanical design of components. Residual stresses on materials shall also be considered for effective stress determination.

All manufacturing methods create residual stresses on materials. Among the manufacturing methods, additive manufacturing is famous for crack formation, distortion, delamination, or other defects because of its nature of layer-by-layer production sequence and high residual stress accumulation.

Laser Powder Bed Fusion (LPBF) is one of the most preferred methods among additive manufacturing processes. Detrimental residual stresses are generally formed in the laser powder bed fusion process due to the high thermal gradients and the nature of melting and solidification of each metal powder layer during production.

This study aims to understand the influence of additive manufacturing process parameters on residual stress of 17-4 PH stainless steel parts manufactured by laser powder bed fusion additive manufacturing system. Within this study, 17-4 PH stainless steel specimens were produced with various process parameters. The effect of scanning strategies, layer thickness, preheating of the baseplate, laser power, exposure time, volumetric energy density, hatch distance, point distance, separation from the base plate were analyzed in terms of residual stress accumulation on the surface and close to the very surface region by X-Ray Diffraction (XRD) method.

The XRD method is sensitive to the surface and near-surface region residual stresses. XRD method also has high accuracy compared to barkhausen, ultrasonic, and eddy current residual stress measurement methods in terms of residual stress measurement. Moreover, the XRD method specimen production dimension restriction is not tight as in the hole drilling residual stress measurement method. Therefore, the XRD residual stress measurement method was chosen for analysis and evaluation within this study.

This thesis consists of five chapters. A review on the current literature about additive manufacturing methods of metallic materials, stainless steels, and residual stresses is given in Chapter 2. Firstly, additive manufacturing of metallic material is presented. Notably, Laser Powder Bed Fusion (LPBF) process details in terms of scanning strategies and pulsed-wave mode production process parameter details are given in this chapter. Next, the properties of stainless-steel types are discussed, and a detailed review of precipitation-hardening stainless steel is presented with a focus on the LPBF process. Then, the origins and general characterization of the residual stresses, mechanical behavior's effect, and the residual stress's overview measurement are presented. The current status of literature studies on additive manufacturing and stainless-steel residual stress studies are shared within this chapter. In Chapter 3, experimental procedure details are given. Starting material, experimental setup, sample preparation, characterization technique details, and simulation information are presented. The results and discussion of this thesis is presented in Chapter 4. The influence of process parameters on residual stress of 17-4 PH stainless steel parts manufactured by LPBF process, including scanning strategies, layer thickness, preheating of the base plate, rotation, power, exposure time, volumetric energy density, hatch distance, point distance, sample separation from the base plate by EDM, height and area effect were tried to be analyzed and discussed in Chapter 4. Finally, conclusions and future term studies are presented in Chapter 5.

CHAPTER 2

LITERATURE REVIEW

Additive Manufacturing (AM) is a process for building 3-Dimensional (3D) parts from 3D model data layer by layer from powder, wire, or sheet material. AM is preferred particularly for complex part production with almost no additional tooling, fewer final assembly requirements, and rapid prototyping capability. Metal, polymer, and ceramic parts can be produced by the AM process [1]–[3]. Virtual models and simulations also allow fast feasibility feedback during the design phase of AM parts, making the AM process very attractive [4].

AM is preferred particularly for unique & complex part production due to fewer assembly requirements, rapid prototyping capability, and high-performance benefits [5]. AM also enables lightweight part production with very few swarf and provides design freedom compared to conventional production methods. This process can also be used for the repair application of materials [3].

ISO-ASTM 52900 standard classifies AM technology into seven categories which are namely Material Jetting (MJT), Vat Photopolymerization (VPP), Powder Bed Fusion (PBF), Sheet Lamination (SHL), Material Extrusion (MEX), Directed Energy Deposition (DED) and Binder Jetting (BJT). Among these seven AM methods; PBF, DED, BJT, SHL, and MEX are the used ones for the metal additive manufacturing process [2].

2.1 Additive Manufacturing of Metals

Metallic materials production by AM is increasing due to the design advantages of AM process and increasing material and conventional production costs for less amount production [1], [6]. Compared to the subtractive conventional production

methods for metallic material such as turning and milling, AM directly builds successive layers from Computer Aided Design (CAD) Models. Therefore, Metal AM has got significant attraction of particularly aerospace, defense, medical, energy and automotive industries in the last century mainly for fewer production steps, realization of custom & complex shape designs and weight optimization of parts which can be impractical, unfeasible or too expensive by conventional processes [7] ,[8]. Unique design provides consolidation of many parts with AM. Complex and unique design example of the AM space rocket engine produced by SLM Solutions company is given in Figure 2-1. The rocket engine is manufactured in a single cycle by a unique design of cooling channels with Inconel 718 alloy. Combustion chamber, injector, manifolds, cooling channels produced in a single production cycle [5].

Figure 2-1 Combustion chamber, injector, manifolds, cooling channels produced by AM. Copyright: ©SLM Solutions/ CellCore [5]

2.1.1 Powder Bed Fusion

Metal Powder Bed Fusion (PBF) process is the fusing of the metal powders in a bed by generally laser or electron beam energy sources[3], [6] Most of the steel, aluminum, nickel, cobalt, chrome, copper, titanium-based metal alloys can be produced by PBF process. Power, scan speed, hatch distance, scanning strategy, layer thickness, and preheating of baseplate are the critical parameters for the PBF method [9].

2.1.1.1 Laser Powder Bed Fusion

Laser Powder Bed Fusion (LPBF) is one of the additive manufacturing methods by fully melting metal powders layer by layer in a powder bed with a focused laser beam used as the heat source of the process [2], [6], [7]. The LPBF process is also known by the trade name of ‘‘Selective Laser Melting (SLM)’’ or ‘‘Direct Metal Laser Sintering (DMLS)’’[6].

During the LPBF process basically, the first CAD model of the part is prepared. Then, the CAD model is uploaded to the LPBF machine and the process starts. Part is formed by the micro welding process of each layer by the laser heat source. Powder bed descends with predetermined layer thickness and metal powders are recoated by a recoater, wiper, or roller mechanism. The laser melts the powder on the base plate of the installed CAD model section, and the process repeats until the part building is completed. The process is performed under an inert gas atmosphere or vacuum environment to avoid oxidation of the material [7]. The schematic of the LPBF process is given in Figure 2-2 [10].

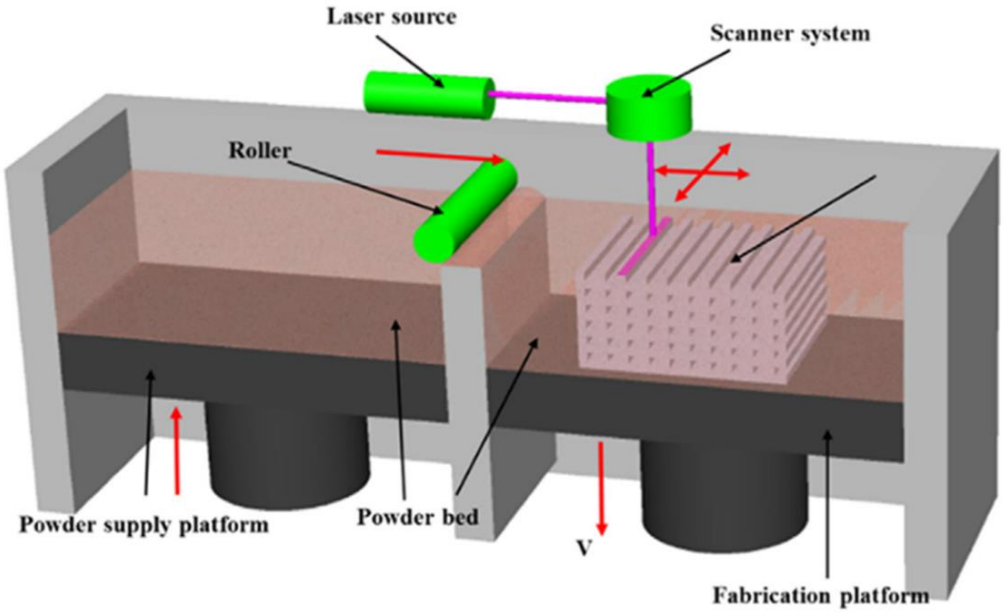

Figure 2-2 Laser powder bed fusion system schematic [10].

The part is removed mechanically or chemically from the support structure if the support structure is used during production. Support structures are usually needed for downskins of the parts features. The function of the support structures is mainly for printability of a part, part balance, and to be able to produce engineering parts with minimum distortion due to thermal effects and gravitational forces. The support structure used metallic part example is given in Figure 2-3 . The support structure is removed from the part by post-processes [5].

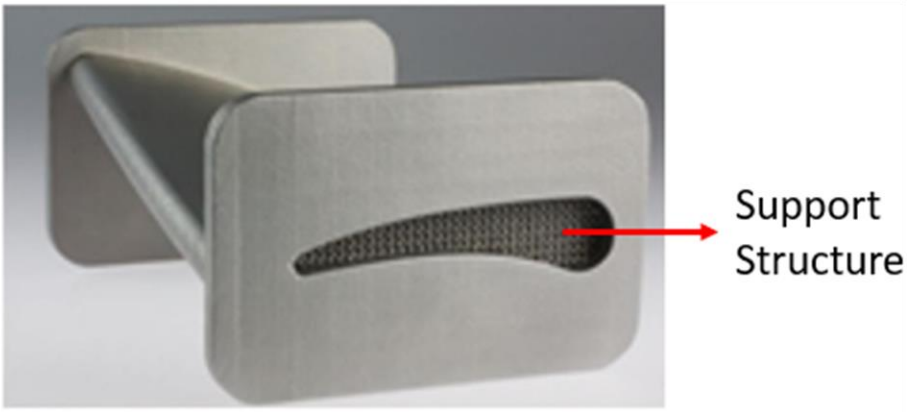

Figure 2-3 Support structure demonstration for a metallic part [5]

There have been several support methods for metal AM, mainly lattice support, unit cell support, cellular support and, pin support structures. Support structure application for downskin structure of an additive manufactured part is given in Figure 2-4 [11].

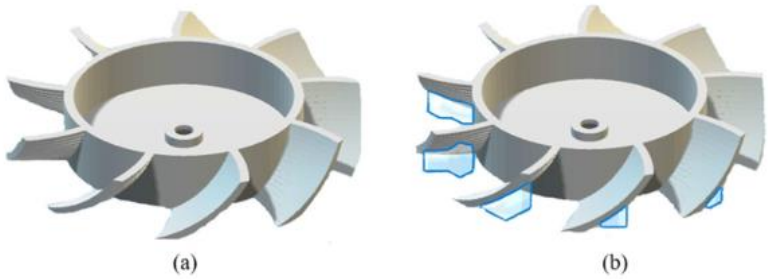

Figure 2-4 Support structure application for downskin structure of an additive manufactured part. (a) an engineering part to be built and support structure for downskins of an engineering part. [11]

The processed part can be removed from the base plate by Electric Discharge Machining (EDM) since EDM usually has minor effects on the formation of additional residual stresses compared to mechanical removal processes such as band saw machines or abrasive cutters. After the removal of the part form baseplate, additional post processes such as laser polishing, laser peening, abrasive flow machining (AFM), electropolishing, electro chemical surface treatment can be used to improve the surface quality of the part [12], [13].

Hot Isostatic Pressing (HIP) is accepted as thermal post processing. HIP can be applied to the as built part to heal or eliminate the defects and particularly porosities formed in a material during production. The HIP process has a positive impact on the fatigue life of AM parts. However, before applying the HIP process, material heat treatment conditions shall be considered. Abnormal grain growth for some materials might be observed during the HIP process which might change the mechanical properties of materials. The dimensions of engineering materials can change due to high pressure applied from all directions in a closed and high-temperature environment. Therefore, the HIP process is carefully handled, and dimensions of the parts are remeasured after the HIP process [12].

The baseplate of the LPBF is usually chosen with the same or similar material as the powder that is used to minimize residual stresses on the as built part. Otherwise, thermal conductivity differences on the part can cause residual stresses, distortions, delamination or other defects on as built structures.

During the process of part production by LPBF. Some satellites can be formed on powders and some of the powder's shape can be changed from spherical particles to other undesired forms. However, the unmolten powder is sieved and can be reused several times for part building [14]. Shape, particle size, surface roughness distribution changes mainly affect the consolidation of the proper powder layer during recoating and which significantly affects the joining kinetics of powders. Therefore, the morphological properties of powder have an impact on the material properties and densification behavior of a material. Particle morphology is controlled by Sieve Analysis, Microscopy, Laser Light Diffraction, and other methods. Particle Chemistry can be checked by Energy Dispersive Spectroscopy [15]. The powder properties are regularly checked to establish repeatability and reliability of the production. The typical particle range utilized for LPBF is 15μm – 80μm. The powder size range is critical for dense part production. Finer particles contribute to higher densification due to the capability of filling pores. However, for larger particles more empty spaces are observed during recoating process of powders by wiper, as it can be seen in Figure 2-5. Although finer particles are better for filling pores for each layer, there is a limitation for fine particle size. When the powder size gets finer than the predetermined range, agglomerations are observed which has a detrimental effect on part production. Agglomeration of metal powders restricts proper flow behavior in the LPBF process [15].

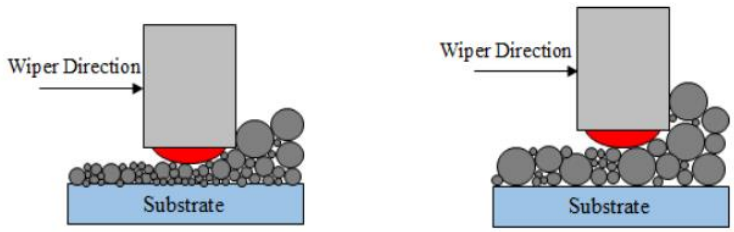

Figure 2-5 Particle size densification effect for layers [15]

The chemical composition of the powder particles used in AM is also essential as the morphology of the powders. Therefore, the chemical composition of the particles is checked before usage for particle production or certified powders are used for AM.

Commercial simulations can also be used to optimize of the production of the parts. Thermo-mechanical simulations can be performed to understand the effect of process parameters [16]. Moreover, fast modeling and residual stress prediction methods are trying to be developed for the LPBF process with some assumptions [17].

However, usually calibration data is needed to perform simulation and the simulation data is limited for some fundamental scanning process parameter limitations. Cantilever parts are required to be produced on at least 0° and 90° with optimized process parameters as given in Figure 2-6. The obtained distortion analysis data is used for calibration data of additive simulation applications which takes some time [18], [19].

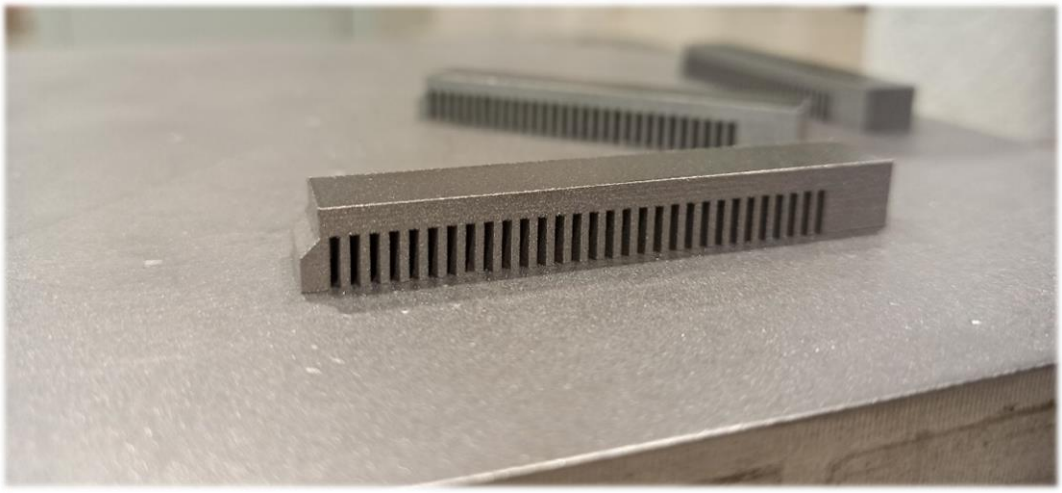

Figure 2-6 Cantilever parts for process parameter simulation calibration data property determination

The LPBF process has the following significant advantages compared to traditional metal subtractive processes such as turning and milling [5], [20];

I. Allowing multi-scale complex geometry design and part production, which allows lightweight designs,
II. Rapid prototyping,

III. High buy to fly ratio in aviation (with conventional production methods, complexity causes an increase in the cost of the part due to additional assembly requirements. However, in production by AM, complexity almost does not affect the cost of the part),
IV. Less investment cost for new and less amount of part production.

However, the LPBF process has the following disadvantageous compared to traditional processes [1], [20];

I. High residual stresses,
II. Usually, strong anisotropy formation occurs due to build up direction limitation,
III. Possibility of formation of undesired phases,
IV. Difficulty of microstructure control,
V. Mechanical property uncertainties,
VI. Additional post-process requirements.

In order to get better and desired mechanical properties, almost fully dense structures are tried to be obtained by developing process parameters in the LPBF process. Almost fully dense structures can be achieved by cautiously controlling the most dominant process parameters such as volumetric energy density (VED), layer thickness (LT), power and scanning strategies [21] [22] [23].

There are two types of laser power systems for the LPBF process which are namely Continuous-Wave (CW) mode laser and Pulsed-Wave (PW) mode laser. The laser is always on for CW mode, while subsequent laser point shots are applied for PW mode [24]. PW mode properties are mainly focused on and discussed within the scope of this thesis.

VED (J/mm^3) is calculated by *Equation 1* where μ is the fractional loss factor due to reflectivity of the powder bed and other losses such as conduction and radiation due to powder properties, P (W) is the laser power, V (mm/s) is the continuous laser

scanning speed, HD (mm) is the hatch distance and LT (mm) is layer thickness for Continuous-Wave (CW) mode for LPBF process [21] [24].

$$\text{(CW) } VED = \frac{\mu \, x \, P}{v \, x \, HD \, x \, LT} x 10^3 \qquad \textit{Equation 1}$$

*VED: volumetric energy density (J/mm^3), μ: loss factor, P: laser power (W), v: scanning speed (mm/s), HD: hatch distance (µm), LT: layer thickness (mm),

Pulsed-wave (PW) mode laser process of LPBF requires replacement of V (mm/s) with Exposure Time (ET) and the Point Distance (PD) between two pulses as given in *Equation 2*.

$$\text{v} = \frac{PD}{ET} x 10^{-3} \qquad \textit{Equation 2}$$

* PD: point distance (µm), ET: exposure time (µs)

By replacement of ET (µs) and PD (µm) values with V (mm/s) *Equation 3* is obtained for Pulsed-Wave (PW) mode LPBF process.

$$\text{(PW) } VED = \frac{\mu \, x \, P \, x \, ET}{PD \, x \, HD \, x \, LT} \qquad \textit{Equation 3}$$

The distance between two pulse centers on scanning direction can be described as Point Distance (PD) and the distance between the two-scanning line can be described as Hatch Distance (HD). PD and HD illustrations of a top view and PD illustration from the isometric view are shown in Figure 2-7 and Figure 2-8 respectively.

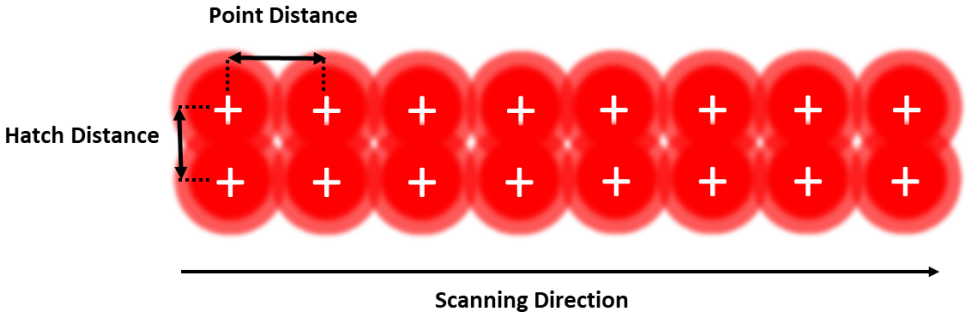

Figure 2-7 Point Distance (PD) and Hatch Distance (HD) illustration (top view)

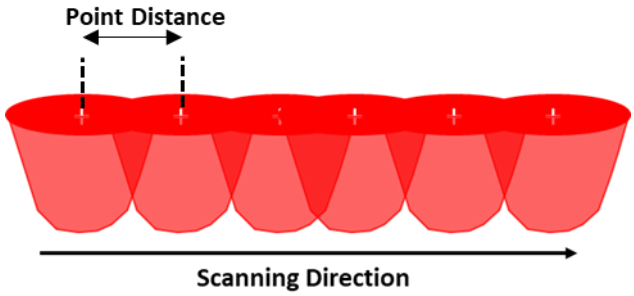

Figure 2-8 Point Distance (PD) illustration (isometric view)

Exposure time can be described as the duration of the pulse when the laser is on and it forms waves as shown in Figure 2-9 [24]. Process parameters given in *Equation 3* are optimized in accordance with material properties and design requirements for the LPBF process.

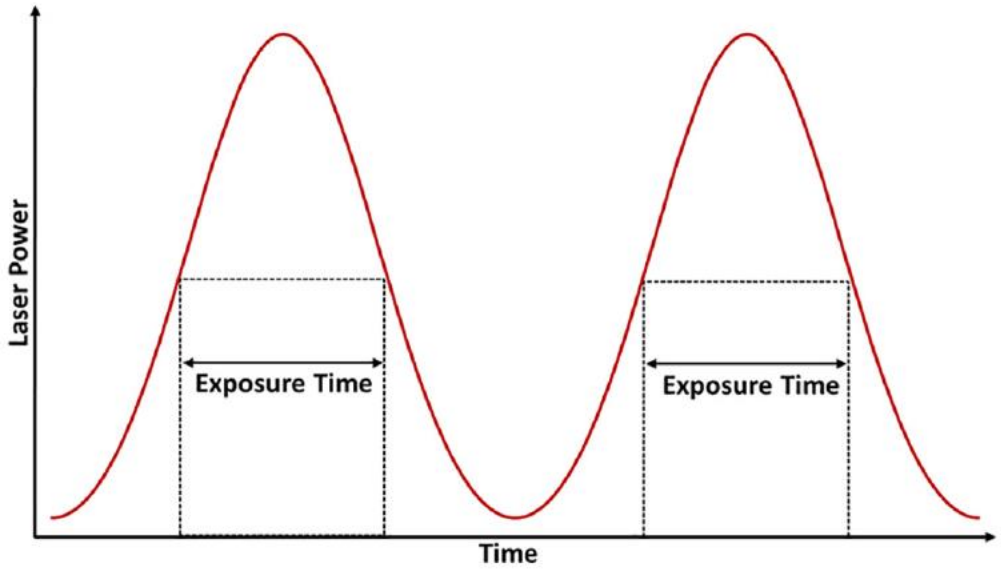

Figure 2-9 Exposure Time (ET) illustration for pulsed-wave mode for LPBF [24].

Process parameters in the LPBF process are very crucial in order to obtain fully dense parts. An illustration of VED optimization is given in Figure 2-10. Keyhole porosities are observed in the low scanning velocity and high source powers due to high energy input. When source power is low, and scanning velocity is high, lack of fusion porosities is observed due to low energy input. When both scanning velocity

and source power are higher than the optimum value, the balling effect is observed on the powder material which deteriorates the structure of the part [25]. Therefore, process parameter optimization is required to get almost fully dense parts.

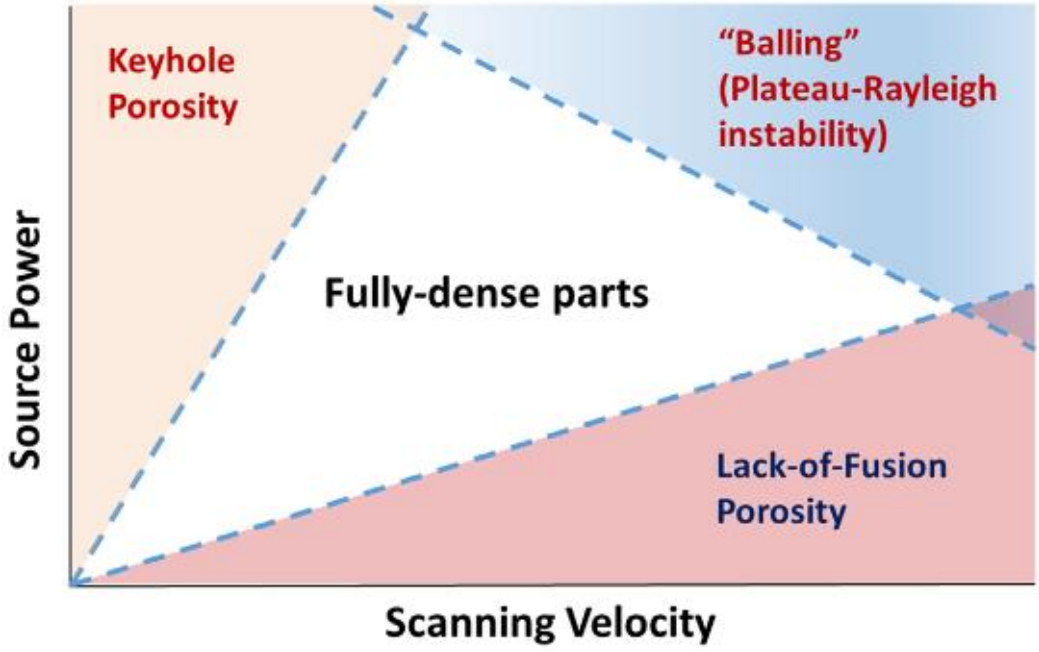

Figure 2-10 Fully dense structure optimization by source power and scanning velocity process parameters [25]

Layer thickness and scanning strategy information of LPBF of Renishaw AM400 Equipment are described below [26];

I. Layer Thickness:

   Layer thickness is the slice thickness of each additive manufacturing layer in the Z direction demonstration of layer thickness is given in Figure 2-11.

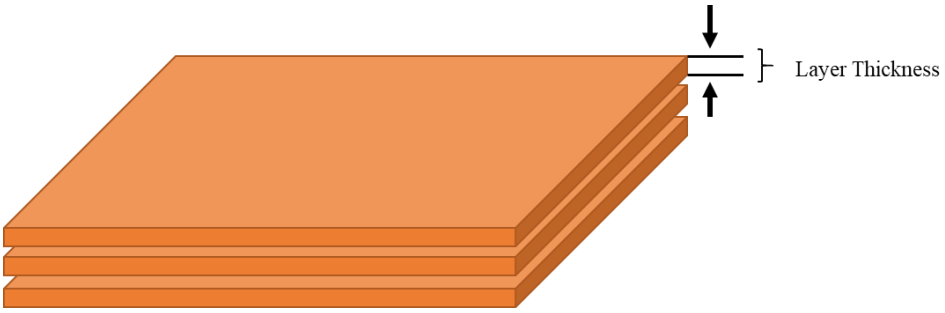

Figure 2-11 Layer thickness demonstration

II. Hatch Distance:

Hatch distance, also known as hatch spacing, can be defined as the distance between the two adjacent layers. A demonstration of hatch distance is given in Figure 2-12. Hatch distance is also a critical process parameter by influencing thermal energy induced on the powder line. When the powder line is very close to each other, high thermal stresses occur due to high energy input. If the hatch spacing is too high between the neighbor lines, powders cannot form a strong bonding, and high porosity formation occurs [27].

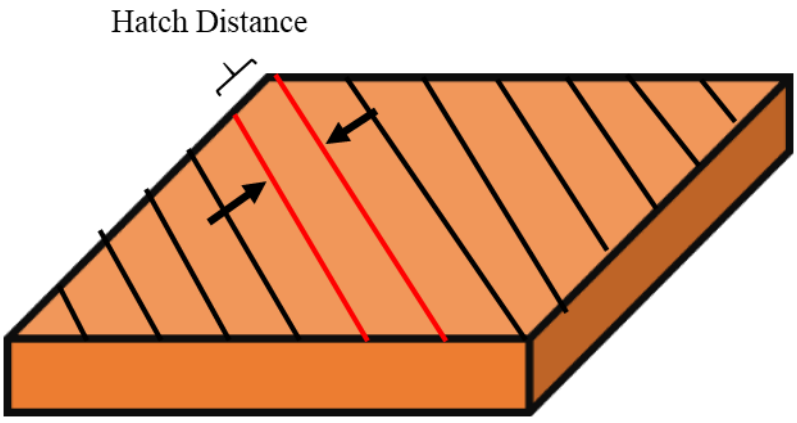

Figure 2-12 Hatch distance demonstration

III. Meander Scanning Strategy:

Meander scanning strategy is the complete filling of the top layer by straight line vector paths like snake patterns from each side of the border. A demonstration of the

meander scanning strategy is given in Figure 2-13. It is accepted as a quick and efficient way for pulse mode additive manufacturing.

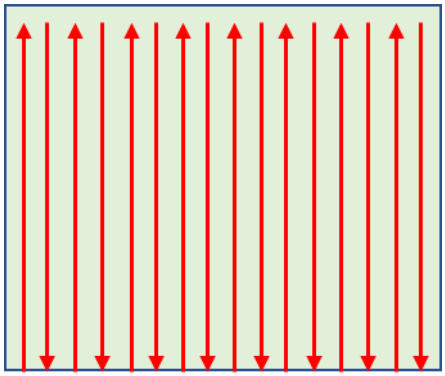

Figure 2-13 Meander scanning strategy demonstration

IV. Stripe Scanning Strategy:

Stripe scanning strategy technique is similar to the meander scanning strategy. The difference between meander and stripe is that the border area of the layer is split into small areas. Scanning is completed within those defined splits, as given in Figure 2-14. This scanning strategy is slower than the meander scanning strategy due to more jump requirements.

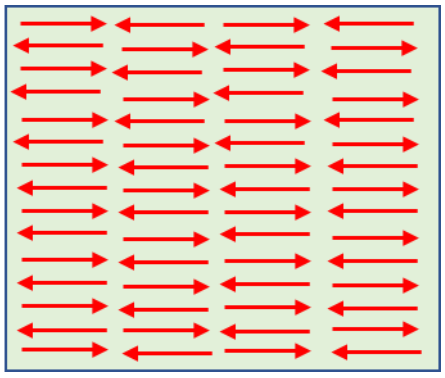

Figure 2-14 Stripe scanning strategy demonstration

V. Chessboard Scanning Strategy:

Chessboard scanning strategy is similar to the stripe scanning strategy. The difference between the stripe and chessboard scanning strategy is splitting the stripes

into squares like a chessboard, as given in Figure 2-15. Each square in the chess board structure is rotated by 90°. This method is significantly slower than the stripe scanning strategy. This method is not commonly used in industry because of creating additional borders, which might be detrimental for an additive manufactured part.

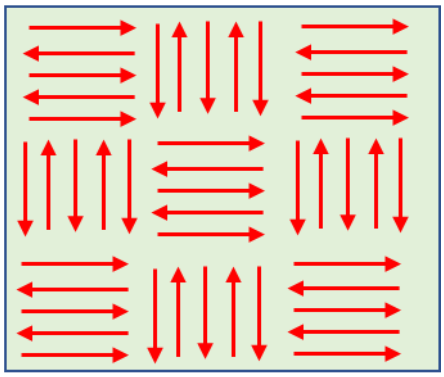

Figure 2-15 Chessboard scanning strategy demonstration

VI. Total Fill

Total Fill scanning strategy is used for the support structure production of materials. Support structures are usually removed from the main part to be produced. Therefore, the Total Fill scanning strategy is a kind of loose production strategy and almost never preferred for main part production.

VII. Rotation:

Rotation for the LPBF process is applied for each layer in order to prevent material deterioration. A representative rotation demonstration of additive manufacturing of each layer is shown in Figure 2-16. The rotation angle can be arranged by the user, and it is usually determined as an angle of 67° to minimize layers overlapping on the same angle generation. Repeating the overlapping angle might negatively affect the mechanical properties of additive manufactured material properties.

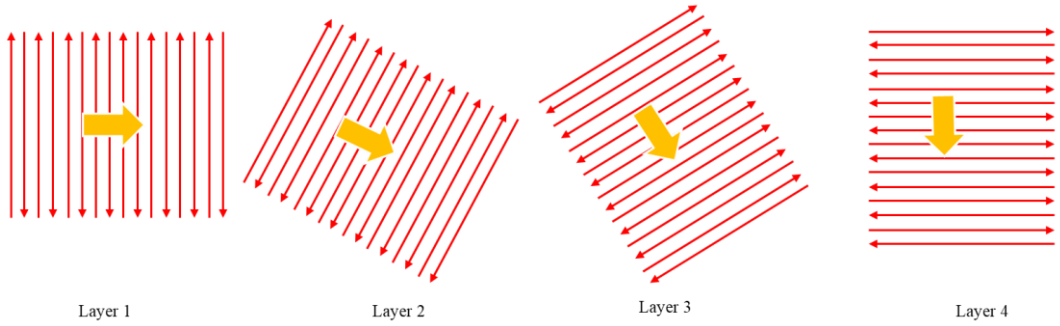

Figure 2-16 Rotation demonstration for additive manufacturing layers

2.1.1.2 Electron Beam Melting

Laser Powder Bed Fusion (LPBF) and Electron Beam Melting (EBM) use almost the same metal joining principle. LPBF and EBW are distinguished mainly by energy source, process environment, and process capability. Typically, electron beam source powder hoppers and a metal rake are used with hot powder surrounding the environment in EBM, while laser source with lenses, scanning mirror to maneuver for melting the target area, and soft blades to distribute homogenous powder across layers are used in LPBF [1], [7]. Focused electron beams melt the powders in a powder bed in the EBM process. Conductive and non-ferromagnetic materials can be produced by the EBM. Otherwise, overcharging occurs and deflection of electron beams is observed due to the nature of the EBM process. The EBM process is performed close to the sintering temperature of powder materials that are to be used. This preheating operation prevents the flying of powders in a powder bed due to electrostatic forces. Therefore, by preheating the powder bed powders are slightly sintered in the powder bed. This sintered block powder is called a “cake” type structure. Processing at high temperatures and slow cooling reduces high-temperature gradients and residual stresses. However, satellites on powders are formed due to the sintering process which increases the porosities in a material, decreases the density and increases the surface roughness of a part [28]. The schematic structure of EBM is given in Figure 2-17 [1].

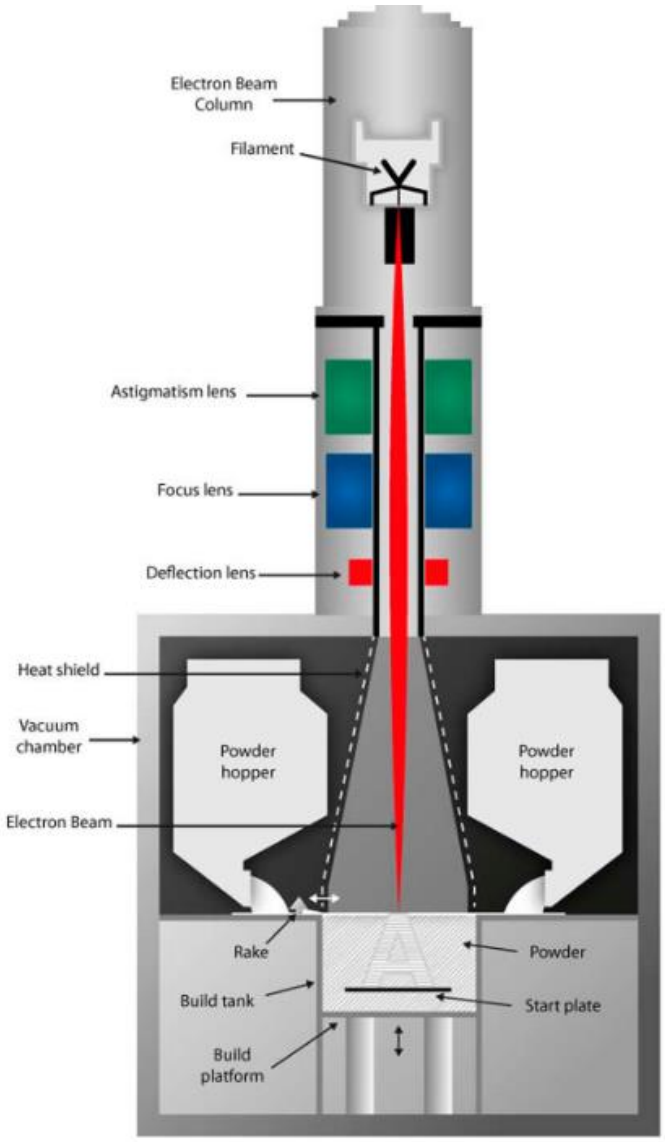

Figure 2-17 Electron beam melting schematic [1].

2.1.2 Directed Energy Deposition

Directed energy deposition (DED) is an AM process where metal is deposited by spray or metal wire feedstock through a focused heat source [9]. In DED, several types of heat sources can be used which are mainly electric arcs, laser beams and electron beams. DED process. The heat source of DED process generally operated

by a CAD file integrated into automated motion software and powder or wire material deposited to build the object [5]. Residual stresses also accumulate on materials at the critical level by the DED method depending on material type and process parameters [29].

Materials that have cracking resistance during or after solidification can usually be processed by DED. The weldability of the alloys can be accepted as the main criterion for DED application. Therefore, most of the weldable superalloys, titanium alloys, ferrous alloys and aluminum alloys can usually be produced by the DED process. The DED process environment is closely monitored against oxidation of materials as in the welding operation of materials. The DED process is also suitable for the repair application of materials due to its easier applicability like in welding operations [3]. The DED operation usually allows bigger part production. Space rocket nozzle extension (1,52-meters in diameter and 1,78 meters in height) was produced in 90 days by NASA as shown in Figure 2-18. [5].

Figure 2-18 Space rocket nozzle extension [5]

2.1.3 Binder Jetting

Binder jetting process uses powder material mixed with liquid-based binding agent. Metals, ceramics, and polymers can be produced by the binder jetting [9]. This process is mainly used prototyping for metallic materials. Generally sintering shrinkage occurs as nature of the process. Moreover, warpages and grain growth can be observed for metallic materials due to the sintering process. However, the binder jetting process is rapidly developing. Mainly the produced objects have isotropic properties [3].

The binder jetting basic process map is given in Figure 2-19. Firstly, the powder material is homogeneously mixed with a binding agent, then a 3D object is built like inkjet printing. The build object is called the green part. The green part is then dried

or cured usually in an ambient environment. Before the sintering operation, the part is heated to burn out the binder material and by heating brown part is obtained. After that, the part is sintered and a denser final structure is obtained. The binder jetting process equipment working principle is similar to powder bed fusion process equipment. A schematic of the binder jetting process is given in Figure 2-20 [30].

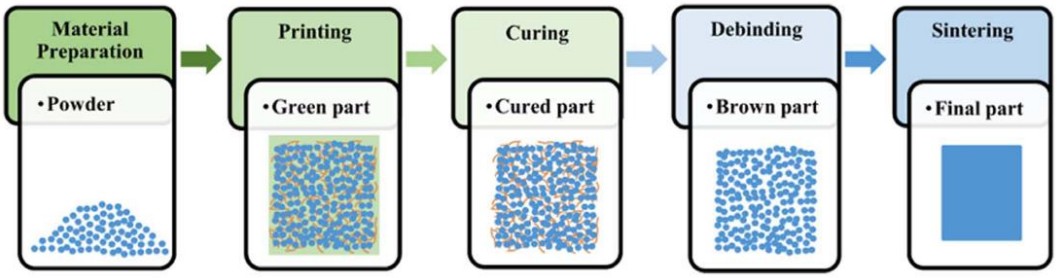

Figure 2-19 Binder jetting basic process map [30]

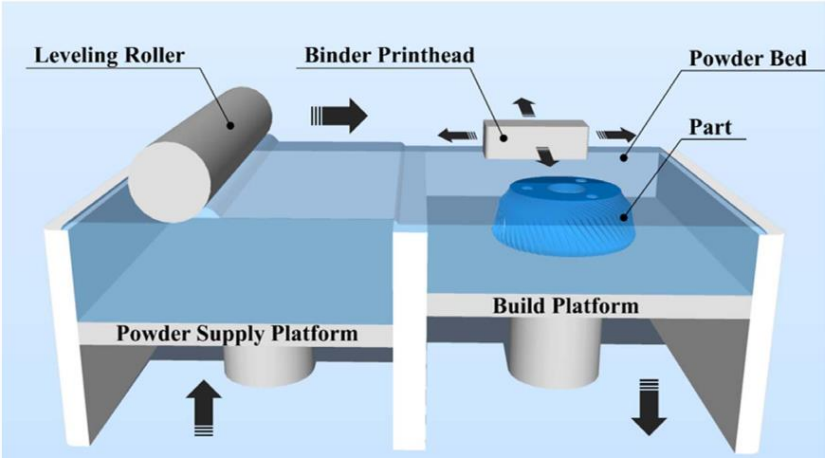

Figure 2-20 Binder jetting system schematic [30]

2.1.4 Material Extrusion

Material extrusion (MEX) of metallic materials is performed by metallic filament extrusion through a die or nozzle [9]. This process is usually compared with the conventional metal injection molding process since this AM process is based on well-known traditional extrusion technology [3]. Metal extrusion AM process can

be classified into three main classes depending on the feeding system, which are screwed (a), plunger (b) and filament (c) based as given in Figure 2-21 [31].

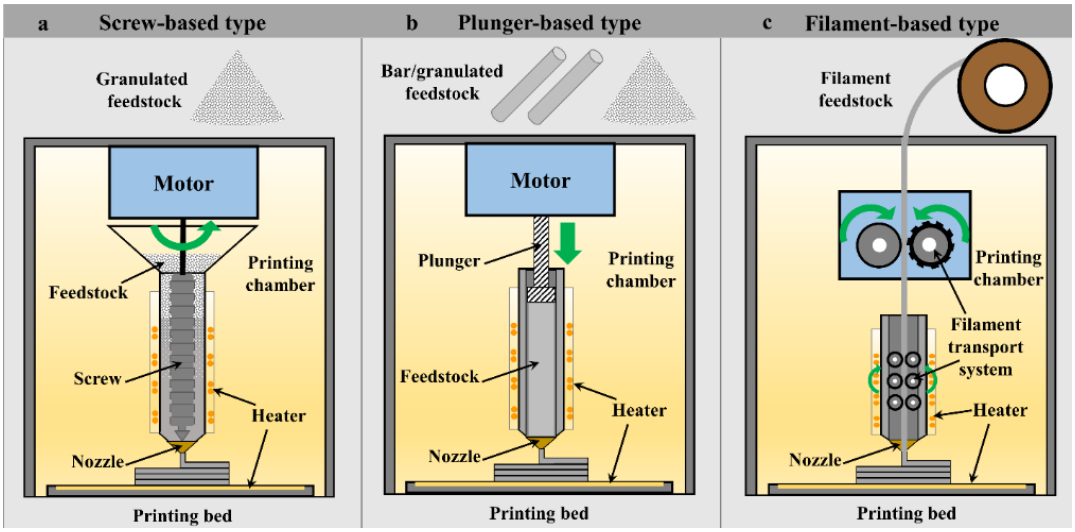

Figure 2-21 Metallic material extrusion types [31]

Metallic part building by ME type AM basic principle is firstly, metal powders homogeneously mixed with liquid binder. The object is shaped via a material extrusion process. Then, the degrading process is performed by heating and releasing binder material. Finally, the material is sintered, and part fabrication is completed, as the process map is given in Figure 2-22 [32].

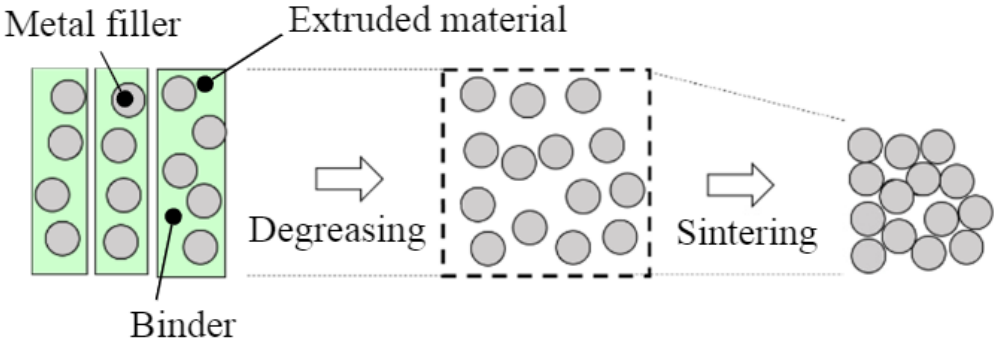

Figure 2-22 Metallic material extrusion type AM process map [32]

2.1.5 Sheet Lamination

Metallic sheet lamination process is basically performed by cutting layers of sheets of materials, adding each of them together to desired shape and bonding them together [9]. Generally ultrasonic or laser heat sources are used for the sheet lamination AM process for the bonding process. The sheet lamination AM process has advantages for bigger parts production due to faster production rates compared to other metallic AM processes. Material properties and layer thickness play a crucial role in bonding together layers. When the process parameters cannot not be optimized, unexpected delamination might occur at the interface of each layer where the part usually is weaker. The sheet lamination AM process has also design limitations of complex part production when compared with other AM methods [33].

2.2 Stainless Steels

Literature information for stainless steels is given within the scope of this thesis and particularly precipitation-hardened steels are discussed. Stainless steels are an important class of metallic materials with a variety of usage areas from home tools, furniture, food, automotive, construction, medical, and aerospace to very sophisticated space applications. Stainless steels consist of at least 11 % chromium (Cr) as a main element. Chromium in stainless steel provides very thin layer of the passive film, which retards corrosion formation. Besides the main element Cr, other alloying elements such as molybdenum (Mo) and nickel can also be added for enhancing pitting and obtaining austenitic properties to ferritic stainless steels respectively. When Ni and Cr content exceeds Fe content, the material type changes to other classes rather than being a steel [34], [35]. Schaeffler diagram can be used, which is given in Figure 2-23 to show stable phases at room temperature by Cr and Ni equivalent wt% calculation of stainless steel while heating to 1050°C for half an hour and then water quenching. Cr_{eq} (wt%) and Ni_{eq} (wt%) are given in Equation 4 and Equation 5 respectively [35].

Cr_{eq}: %Cr + 2%Si + 1.5(%Mo) + 5(%V) + 5.5(%Al) + 1.75(%Nb) + 1.5(%Ti) + 0.75 (%W) *Equation 4*

Ni_{eq}: %Ni + %Co + 30(%C) + 25(%N) + 0.5(% Mn) + 0.3(%Cu) *Equation 5*

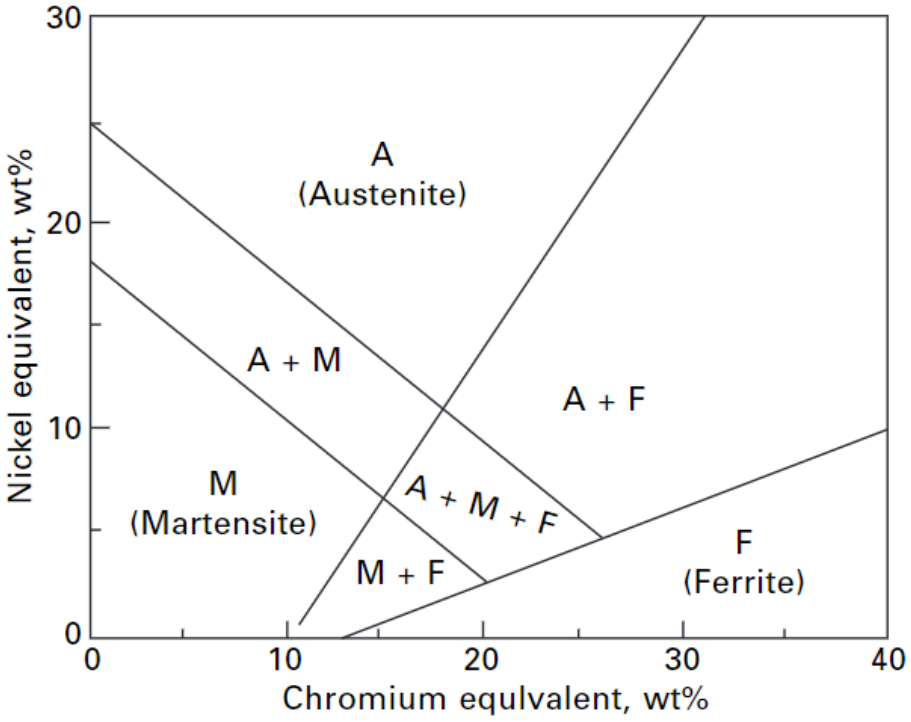

Figure 2-23 Schaeffler diagram for stainless steel stable phase determination [35]

Brief literature information and material properties of ferritic (α), martensitic (α'), austenitic (γ), duplex and precipitation hardening stainless steels are mentioned in below sections.

2.2.1 Ferritic Stainless Steels

Ferritic stainless steels have a body-centered-cubic (BCC) structure and they are ferromagnetic type stainless steel due to their crystal structure. Chromium is the main

element for ferritic steels and this type of steel almost does not contain nickel element which is an austenite stabilizer. The austenite phase does not occur for ferritic stainless steels when heated which makes them non-heat treatable. Ferritic stainless steel room temperature strength values are close to austenitic stainless-steel type but their elongation values are usually less than austenitic stainless type. Therefore, the toughness properties of ferritic stainless steel are lower than austenitic stainless steel. Ferritic stainless steels have limited high and low temperature usage due to drastic material property changes compared to austenitic stainless steels. Therefore, generally ferritic stainless steels are not preferred much by aviation and space applications where there exist low and high temperature requirements. Ferritic stainless steel is usually designated as 4XX grade in accordance with American Iron and Steel Institute (AISI) notation. 409, 446, 434, and 430 grades are the most common types [36].

2.2.2 Martensitic Stainless Steels

Martensitic stainless steel has body-centered-tetragonal (BCT) structure and it has high strength and wear resistance properties. Cr element is kept lower to get martensite structure, as it is indicated by Figure 2-23. Carbon element content can be between 0.05-1-2%. Low carbon content martensitic stainless-steel type is weldable and it is tried to be kept under 0.4% carbon content. Generally, higher than the 0.4% carbon content martensitic stainless steels are preferred for wear resistance application requirements. In accordance with AISI notation; 410 and 440 grades are the most common types of martensitic stainless steels. Although martensitic stainless steels have lower and limited corrosion resistance, weldability, and formability, they are preferred for high strength and wear resistance applications compared to austenitic and ferritic stainless-steel types [35], [36].

2.2.3 Austenitic Stainless Steels

Austenitic stainless steels are one of the most preferred stainless-steel types due to high temperature stability, cryogenic usage capability and high corrosion resistance properties. Austenitic stainless steels have face-centered-cubic (FCC) crystal structure which makes them non-magnetic material. Ni is added as an austenite stabilizer to austenitic stainless steels. Nitrogen of up to %0,2 can be added to stabilize the austenite (γ) phase and increase the yield strength. Austenitic stainless steel is usually designated as 2XX and 3XX grade in accordance with AISI notation. 304, 316, 321 and 347 grades are the most common types of them. Usually, 2XX grades contain N and Mn as an austenite stabilizer to be cheaper than 3XX grades which use Ni as austenite stabilizer. However, 3XX grade austenitic stainless steels are more corrosion-resistant than the 2XX grades. Low carbon grades of austenitic stainless steels are coded with L notation, such as 304L and 316L [36].

2.2.4 Duplex Stainless Steels

Duplex stainless steels are formed with almost equal percentage of ferrite and austenite phase. Duplex stainless steels are preferred mainly for oil & gas, nuclear, chemical etc. industries. One of the main advantages of duplex stainless steels over austenitic stainless steels is having high stress corrosion resistance. Therefore, for above mentioned industries, duplex stainless steels can be preferred rather than 3XX type austenitic stainless steel to avoid high Ni usage. Duplex stainless steels can be divided into three major types which are namely super-duplex, lean-duplex standard-duplex [37].

2.2.5 Precipitation Hardening Stainless Steels

Precipitation Hardening (PH) stainless steels can be in martensitic, austenitic, semi-austenitic and stable δ (delta) ferritic microstructure at ambient temperatures. The

most common PH stainless steels used in industries are 17-4 PH (UNS S17400), 15-5 PH (UNS S15500), PH 13-8 (UNS S13800), and 17-7 PH (UNS S17700) [38].

Due to its outstanding high strength, hardness, and corrosion properties, 17-4 PH stainless steel is a popular choice among these PH stainless steels in various industries, including chemical, aerospace, and energy sectors. Additionally, 17-4 PH stainless steels are particularly desirable to industries because they are simple to machine under solution heat treatment condition and easily weldable with strong corrosion resistance qualities [39].

17-4 PH stainless steels formed by solution heat treatment followed by age (precipitation hardening) heat treatment. Copper, molybdenum, aluminum, and titanium contribute precipitation formation by age heat treatment. Copper firstly dissolved in the matrix during the solution heat treatment process, and supersaturated phase is obtained. During the age heat treatment process, copper-rich precipitates hinder and make difficult the dislocation motion in a material and increase the strength of a material. When the particle size is less than the critical size cutting mechanism becomes active. Dislocations cut the precipitates which require extra energy. When the particle size is larger than the critical size, the bowing mechanism becomes active. A symbolic drawing for critical radius is given in Figure 2-24 [40]. Dislocation lines deformed and form loops around the particles leaving a loop around the dislocation [41].

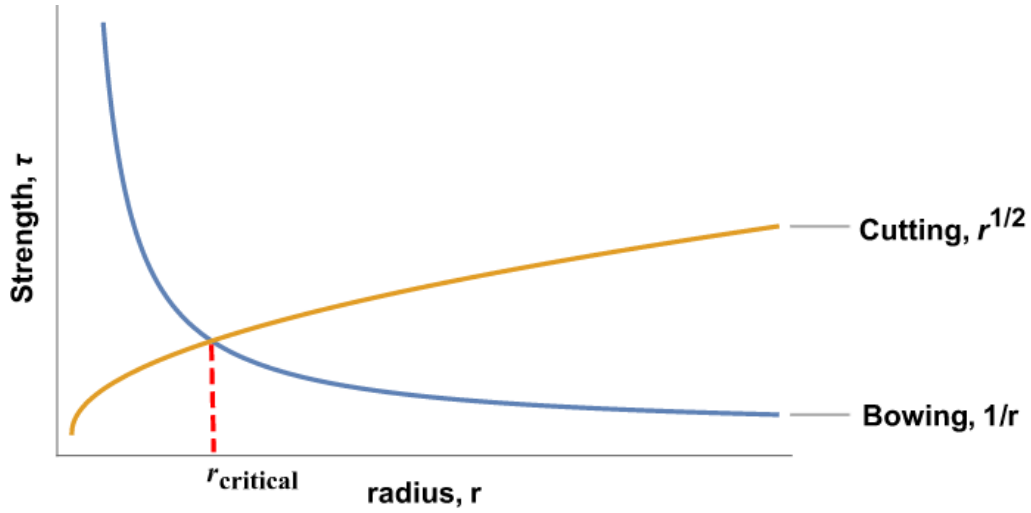

Figure 2-24 Critical radius for cutting and bowing mechanisms [40]

Desired mechanical properties can be obtained by following ASTM A564 (Standard Specification for Hot-Rolled and Cold-Finished Age-Hardening Stainless-Steel Bars and Shapes) heat treatment procedures. Solution heat treatment for 17-4 PH stainless steel is performed at 1040°C ± 15°C as required to below 32°C (usually polymer, oil, or air cooling) and the age hardening between 480°C-620°C following by air cooling can be performed depending on the mechanical properties requirements as stated in ASTM A564 [20], [34], [42]. Typical mechanical properties in accordance with ASTM A564 of mainly used PH stainless steels are given in Table 2-1 [42].

Table 2-1 Mechanical Properties After Precipitation Hardened Condition

Type	**Heat Treatment Condition**	***Tensile Strength (MPa)***	***Yield Strength (MPa)***	***% Elongation***	***Hardness (HRC)***
17-4 PH	H900	1310	1170	10	40
17-4 PH	H925	1170	1070	10	38
17-4 PH	H1025	1070	1000	12	35
17-4 PH	H1075	1000	860	13	32
17-4 PH	H1100	965	795	14	31
17-4 PH	H1150	930	725	16	28
17-7 PH	RH950	1280	1030	6	41
17-7 PH	TH1050	1170	965	6	38
15-5 PH	H900	1310	1170	10	40
15-5 PH	H925	1170	1070	10	38
15-5 PH	H1025	1070	1000	12	35
15-5 PH	H1075	1000	860	13	32
15-5 PH	H1100	965	795	14	31
15-5 PH	H1150	930	725	16	28
13-8 PH	H950	1515	1415	10	45
13-8 PH	H1000	1415	1310	10	43
13-8 PH	H1025	1280	1210	11	41
13-8 PH	H1050	1210	1140	12	40
13-8 PH	H1100	1035	930	14	34
13-8 PH	H1150	930	620	14	30

Chemical composition requirement by weight (wt) % of 17-4 PH stainless steel is given in Table 2-2 in accordance with ASTM A564 [42].

Table 2-2 ASTM A564, chemical composition requirement for 17-4 PH stainless steel by wt%.

Element	***Min***	***Max***
Chromium	15.00	17.50
Nickel	3.00	5.00
Copper	3.00	5.00
Carbon	-	0.07
Manganese	-	1.00
Silicon	-	1.00
Phosphorus	-	0.040
Sulfur	-	0.03
Columbium + Tantalum	0.15	0.45
Iron	Balance	

Mechanical properties of 17-4 PH stainless steel produced by LPBF process were tried to be investigated by Mahmoudi et al. for different orientations and heat treatment conditions [43].

2.3 Residual Stress

Residual stresses are defined as stresses that remain in a material at equilibrium with its surroundings after machining, forging, surface enhancement, heat treating, or other processes and changes which cause materials yielding non-uniform plastic deformation [44]. Residual stresses might be reduced by turning, shot peening, or post processing such as heat treatment. However, it becomes generally too late to remove excessive residual stresses for AM parts since the parts might have already been distorted or cracked that cannot even be repaired [44] [45].

Having knowledge about the remaining residual stresses is crucial, particularly for safe and accurate part design. Life prediction of materials depends on residual stress determination of the body, or component. Due to the nature of additive

manufacturing, parts might be distorted or high residual stresses accumulated in a material which can cause production failures or inaccurate design predictions. Unexpected failures can occur while production by LPBF or during service life of a material [46].

Residual stresses are also highly dependent on material properties in addition to the process and its parameters. The changes in material characteristics also highly affect residual stress formation [47]. Even post-processes such as heat treatment which brings additional production cost and time, might not be a solution for the recovery of a material [44]. Therefore, it is essential to understand residual stress phenomena and investigate residual stresses by critical process parameters such as laser power, scanning speed, hatch distance, scanning strategy, layer thickness, and preheating of the baseplate for pulsed mode laser powder bed fusion additive manufacturing system.

2.3.1 Origins and General Characterization of The Residual Stresses

Mechanical, thermal, and metallurgical incompatibilities can be accepted as origins of residual stresses. Generally, plastic flow changes, phase transformations, density changes, cooling/heating rates, and thermal property dissimilarities cause residual stresses.

Residual stresses are formed in a material at different scales. Residual stresses can be varied from macro scale which might affect all body or component to the atomic scale which might only have a local effect [1], [44]. Therefore, residual stresses are usually classified into three categories which are given as follows:

i. *Type I:* This type of stresses are macroscopic scale stresses that might affect all part geometry and can cause distortion of material. Type I stresses is usually observed for LPBF processed parts. Macroscopic stresses might have detrimental effects on the bulk material of LPBF parts.

ii. *Type II:* Type II stresses are micro stresses which affect individual grains and microscopic residual stresses are balanced over several grains. Local grain to grain differences such as slip orientation misalignment can cause this type of stress.

iii. *Type III:* This type of residual stress is observed at the atomic scale. Lattice stresses due to dislocations or other crystalline defects such as vacancies or substitutional atoms can be given as examples for Type III stresses.

Illustrations and typical examples for three main types of residual stress classes are given in Figure 2-25 [44].

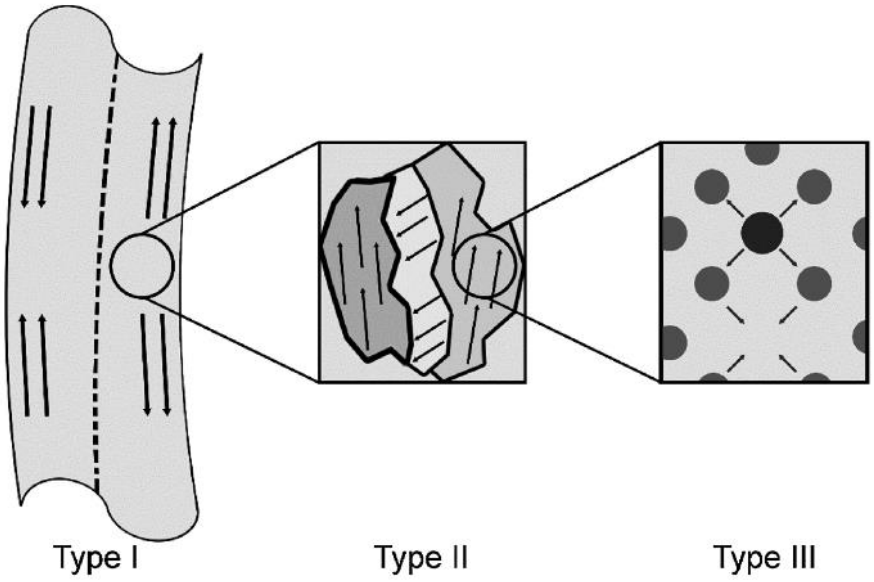

Figure 2-25 Typical examples for three type of residual stress categories [44]

2.3.2 Effect on Mechanical Behavior

Residual stresses might deteriorate the structure and can affect the performance and life of a body. These stresses affect fatigue life, tensile strength, corrosion under tensile stress and dimensional stability properties. Beneficial residual stresses might also be created on material intentionally by the shot peening process. Compressive

residual stresses are formed on a material to increase the component's fatigue life [44], [48].

Laser melts the powder layers with an intense energy that is focused on the target area. Laser source causes thermal expansion during solidified phase occurring. Shrinkage occurs while the melt pool cools down and tensile stress occurs at the re-melting region and compressive stress forms in the interior of the material [20]. Residual stresses are generally formed in AM materials due to high thermal gradients. High thermal gradients cause AM parts distortion when the local yield strength of the material is exceeded. AM parts' mechanical properties are adversely affected due to changes in grain structure. Cracking or other catastrophic defects can be observed when the local stresses are higher than the material's ultimate tensile strength [1] [49].

Quality control of each designed part is very complex and as a drawback, safety factors are kept higher than the conventionally produced parts, which causes an increase in weight at critical applications to prevent unexpected failures due to residual stresses. Residual stresses determine the fatigue life of a material, its resistance to corrosion, distortion effects, and its dimensional stability. Therefore, investigation of residual stresses on parts manufactured by laser powder bed fusion additive manufacturing system is crucial to ensure the reliability of mechanical properties [20]. Therefore, understanding and investigating residual stress phenomena is essential for avoiding and mitigating residual stresses.

2.3.2.1 Studies on Residual Stresses in Laser Powder Bed Fusion Process

Parts manufactured by Laser Powder Bed Fusion (LPBF) processes are prone to residual stress formation due to the nature of melting and solidification of each metal powder layer [20]. Residual stresses formed and accumulated in material during production deteriorate the mechanical properties of materials. Generally, as the closed volume of the part increases, residual stresses formed in material are also

increased due to more energy input to the material. Limitation of part geometry, size, and material alternatives to avoid accumulated residual stresses retards the further application of the laser powder bed fusion process. Unfortunately, residual stresses can be observed, and production failure can occur even for small-sized parts depending on process parameters such as scanning speed, laser power, scanning strategy, and layer thickness as given in Figure 2-26 for the LPBF process.

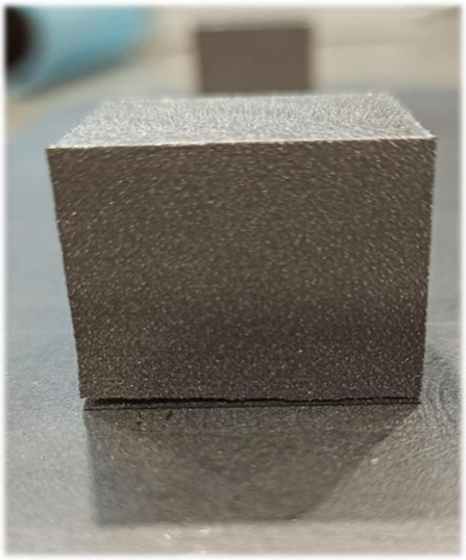

Figure 2-26 Delamination observed on 17-4 PH specimen produced by LPBF

From powder to solid transformation layer by layer causes non-uniform thermal plasticity and non-uniform microstructure, which leads to high residual stresses that deteriorate the mechanical properties of materials. During production by LPBF, each layer has experienced intense cycling loads due to heating and cooling that generates sophisticated phase transformation and thermal stress fields. Similar phenomena of the unsteady thermodynamic state of the solidified phase can also be observed in multi-pass laser welding of a material. Melting and cooling demonstration of each layer by LPBF process is shown in Figure 2-27 [20]. Residual stress source in the LPBF process resembles the multi-pass fusion welds [50]. Preheating the baseplate material is expected to positively affect the residual stresses by reducing the thermal gradients [51].

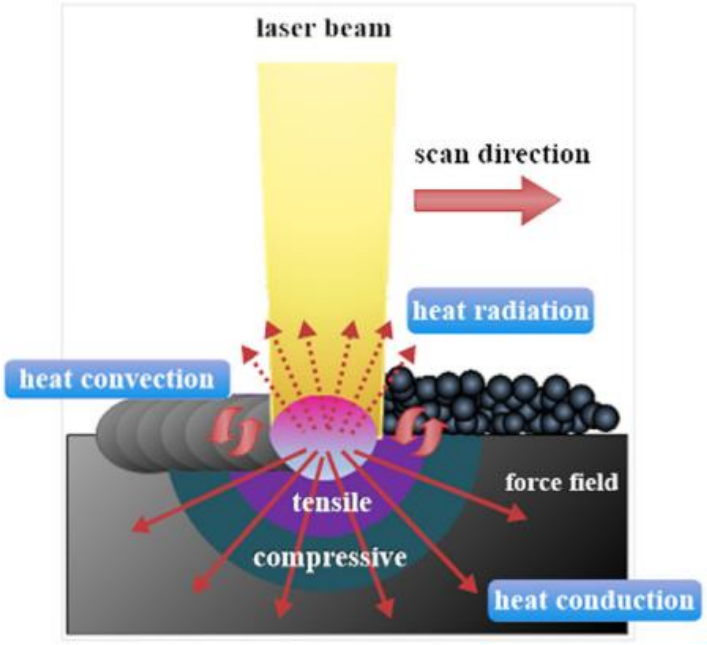

Figure 2-27 Melting and cooling process of LPBF process [20]

Laser Powder Bed Fusion (LPBF) process results in anisotropic and considerable residual stresses which affect mechanical properties of materials, particularly fatigue life. Residual stresses created on material might also cause geometric distortion [44]. During the heating and cooling of each layer of the LPBF process, residual stresses are created. Melted top layer has an interaction with the underlying body by melting into it which creates strong bonding between the new layer and the underlying body. During heating, the new layer would like to expand and the underlying cooler part tries to restrict the expansion of the new layer. Therefore, compressive stresses are formed at the new layer and tensile stress is created at the underlying part of the material. During the cooling process, the cooling rate of the new layer will be higher and it will try to contract and the underlying part restricts the contraction. As a result, tensile stresses are formed at the new layer and compressive stresses are formed at the underlying part of the material as given in Figure 2-28 [44]. As described above, parts produced by the LPBF process have gradual residual stresses due to each neighboring layer's interactions and high-strain accommodation. The magnitude of

the residual stresses even can pass yield strength of a material which distorts the structure.

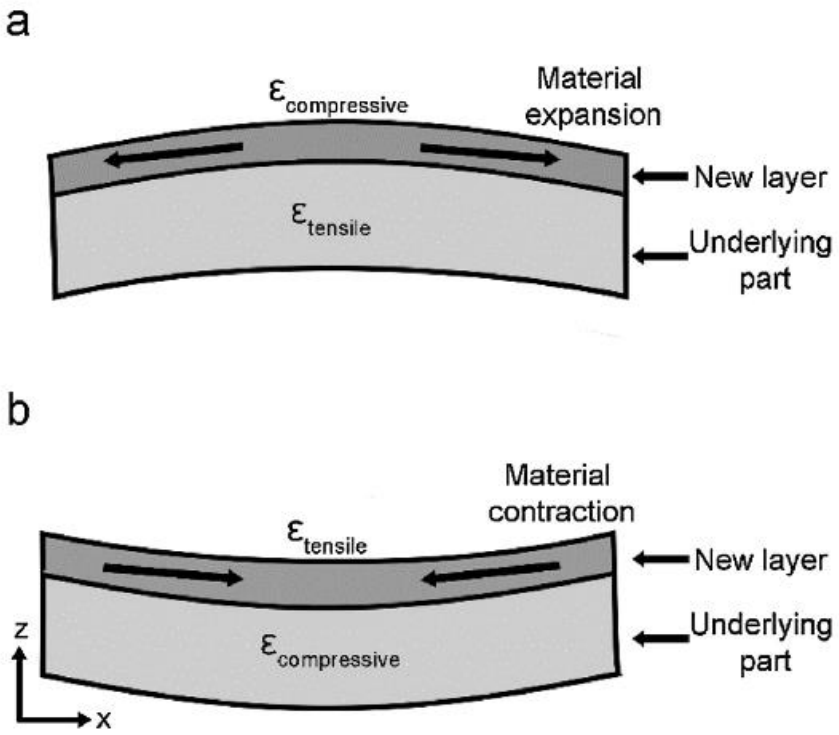

Figure 2-28 Residual stress formation (a) during heating and (b) during cooling of LPBF process [44]

Basically, two zones of residual stress formation are expected for the LPBF process. These zones are intense tensile stresses at the top and bottom of the processed body and large zones of intermediate compressive stress between the top and bottom of the body. Residual stress profile in terms of magnitude can depend on the material properties, shape of the part and process parameters for the LPBF process [52] [53].

T. Simson et al. examined the formation and the effect of residual stresses by XRD measurements on the LPBF process by samples produced by AISI 316L austenitic stainless steel. This study shows that the surface residual stresses slightly increase and then decrease slowly when residual stresses are measured from the top layer to the bottom layer. Layers were removed by the electropolish process for each measurement [27]. Wu et al. examined the speed and energy process effects on

residual stresses by 316L stainless steel by L-shaped specimens. The residual stress measurements were performed by neutron diffraction method. Tensile stresses near the surfaces and compressive residual stresses at the center of the specimens were observed [54]. Song et al. tried to investigate the scanning strategy effect on residual stresses in titanium alloy (Ti6Al4V) produced by the LPBF process. Tensile and compressive stresses were specified on the produced specimens by XRD residual stress measurement method [55]. Parry et al. tried to investigate geometrical effects on the LPBF process by modeling. They found that the distribution and orientation of scan vectors had a relation with macro scale stresses [56]. Mugwagwa et al. researched the influence of porosity formation on residual stress relaxation [57]. Although there have been these kind of recent studies regarding residual stress examination, there is a lot to be investigated for precise control and development of the LPBF process.

2.3.2.2 Studies on the Residual Stresses of 17-4 PH Stainless Steel Manufactured by Additive Manufacturing

17-4 PH stainless steel is very demanded in the industry as mentioned in detail in section 2.2.5. Due to its high mechanical properties and suitability of production by the Laser Powder Bed Fusion (LPBF) process, it is worth investigating process parameters' effect on residual stresses occurring on 17-4 PH stainless steel parts manufactured by pulsed mode LPBF additive manufacturing system. M. Masoomi et al. carried out a study about residual stresses on 17-4 PH stainless steel manufactured by additive manufacturing via neutron diffraction. In this study, optimized process parameters of PHENIX PM-100 Selective Laser Melting equipment for 17-4 PH steel were used for residual stress measurement investigation. Residual stress measurement was focused on the center of the specimen with the advantage of the neutron diffraction residual stress measurement capability. However, the details of process parameters' changes effect have not been mentioned. Moreover, residual stress measurements have not been compared with the other

residual stress measurement methods such as X-Ray Diffraction [58]. M. Leitner et al. examined residual stresses on 17-4 PH stainless steel parts in order to reveal the effect of the surface layer and its properties on fatigue strength of laser powder bed fusion process. In this study the tests were performed with optimized parameters and surface residual stresses were measured by X-Ray Diffraction method. However, the process parameters' effect on residual stresses has not been analyzed [59]. A. Hemmasian Ettefagh et al. searched for the residual stresses effect on corrosion properties on stainless steel parts. This study shows that residual stresses cause pit initiation sites due to distortion in the parts. However, this study also does not show general process parameters' effects on residual stresses on 17-4 PH stainless steel manufactured by the LPBF process [60]. For these reasons, it is necessary to work on process parameters effect on 17-4 PH stainless steel parts manufactured by pulsed mode LPBF additive manufacturing system surface residual stress formation. Therefore, this thesis is focused on the investigation of process parameters' effect on residual stresses occurring on 17-4 PH stainless steel parts manufactured by pulsed mode LPBF additive manufacturing system.

2.3.3 Measurement of Residual Stress

Residual stresses can be measured by destructive or non-destructive methods. Ring core, hole drilling, contour, sectioning, and bending deflection are accepted as destructive type residual stress measurement methods. The destructive residual stress measurement techniques generally measure the change in the internal forces that cause local strains of the material while relaxing it. X-Ray diffraction (XRD), neutron diffraction, magnetic (barkhausen noise inspection), eddy current, ultrasonic techniques, laser holography, raman spectroscopy can be accepted as non-destructive residual stress measurement methods. Non-destructive techniques use the relatedness between crystallographic parameters and residual stress [48], [61], [62], [63]. These methods have advantages and disadvantages compared to each other.

While determining surface and near-surface stresses are critical for the fatigue and corrosion resistance of a material, measuring the bulk stresses are more important for distortion and dimensional stability check [64].

Barkhausen, ultrasonic, and eddy current residual stress measurement methods can provide qualitative residual stress measurement. Neutron Diffraction and sectioning methods are not usually good at surface residual stress measurements. Hole drilling and X-Ray Diffraction (XRD) methods can measure surface and near-surface residual stresses. Hole drilling can be accepted as destructive residual stress measurement method while XRD method can be accepted as non-destructive or semi-destructive depending on electropolish usage. Residual stress measurement comparison for most preferred methods is given in Table 2-3 [65].

Table 2-3 Residual stress measurement method comparisons

Method	Penetration	Destructive	General Properties
X Ray Diffraction	<50μm (Al) <5μm (Ti) <1mm (with electropolish layer removal)	No	High Accuracy (±20MPa). Sensitive to surface stresses
Hole Drilling	1.2x hole diameter ~ 500μm-5mm depth	Yes	±50MPa Sensitivity
Neutron Diffraction	200mm (Al), 25mm (Fe), 4mm (Ti)	No	Sensitive to inner stresses Spatial resolution: 500μm Access difficulties Costly process
Magnetic	10mm	No	10% Accuracy Only for magnetic materials
Ultrasonics	>10cm	No	10% Accuracy Spatial resolution: 5mm

2.3.3.1 Theory of X-Ray Diffraction Stress Measurement Method

X-Ray Diffraction (XRD) method is one most preferred residual stress measurement methods. The basic principle of XRD is the measurement of internal stresses based on elastic deformations within a polycrystalline body. Radiation diffraction within a crystal structure representation is given in Figure 2-29 [66]. For a perfect crystalline material, the intensities of scattered waves are summed up in accordance with *Equation 6* which is called Bragg's Law where n is an integer for multiple of wavelength, d is spacing between the lattice planes in the crystal, λ is X-Ray wavelength and θ is the angle between the incident beam and diffracting planes and also called Bragg angle where constructive interference occurs.

$$n * \lambda = 2 * d * sin\theta \qquad \textit{Equation 6}$$

When the condition of Bragg's Law is fulfilled, constructive interference occurs by X-Ray diffraction. Bragg's Law allows finding spacing between the lattice planes.

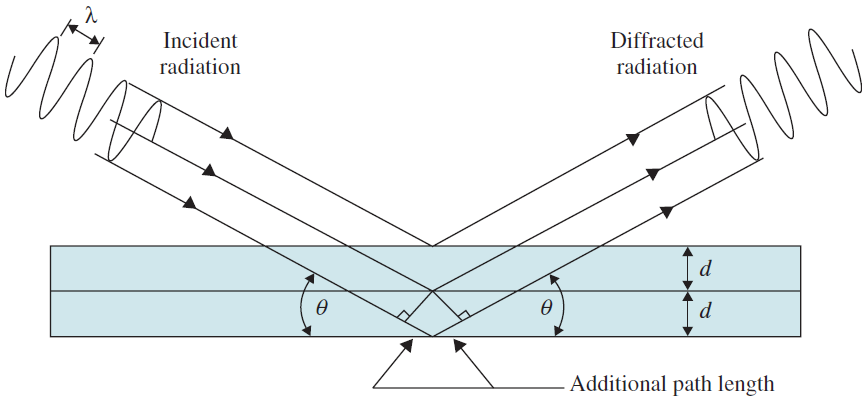

Figure 2-29 Radiation diffraction within a crystal structure representation [66]

X-Ray beams hit a sample and scatter by the atoms in the crystal structure. X-Rays scatter constructively or destructively and create a diffraction pattern. X-Ray waves are summed up when constrictive interface occurs and amplified waves are observed in diffraction patterns. However, when the peaks are not lined up with each other

destructive interference is observed. In order to create constructive interference peaks, the wavelengths of the incident waves shall match the atomic distance. X-Rays have a wavelength in the range of 0,01-10nm, energies in the range of 100eV to 100keV and frequencies in the range of $3x10^{16}$ – $3x10^{19}$ [67].

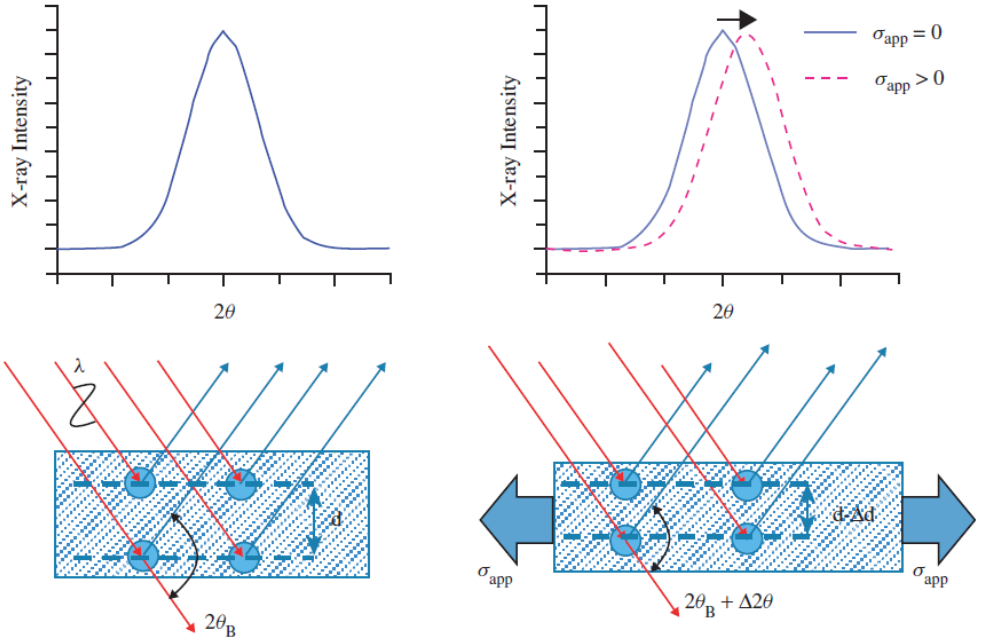

Figure 2-30 Peak position and d spacing shift demonstration under tensile stress [66]

The peak positions are affected by the atomic structure of the sample. The peak intensity is affected by the structural chemistry of the crystal or where the atoms are located within the crystal. The peak shape is affected by the size of the grains and defects in crystal structure. When a material has tensile or compressive stress, d spacing between the atoms changes, and the peak position shifts [66].

CHAPTER 3

EXPERIMENTAL PROCEDURE

3.1 Starting Material

Commercially purchased 17-4 PH stainless steel additive manufacturing powders with the particle size distribution of D_{10}: 21µm, D_{50}:30µm, and D_{90}:41 was used. The particle size distribution graph of the starting 17-4 PH stainless steel powder particle is given in Figure 3-1 Dynamic image analyzer (Camsizer X2, Microtrac, Osaka, Japan) is used for particle size measurement.

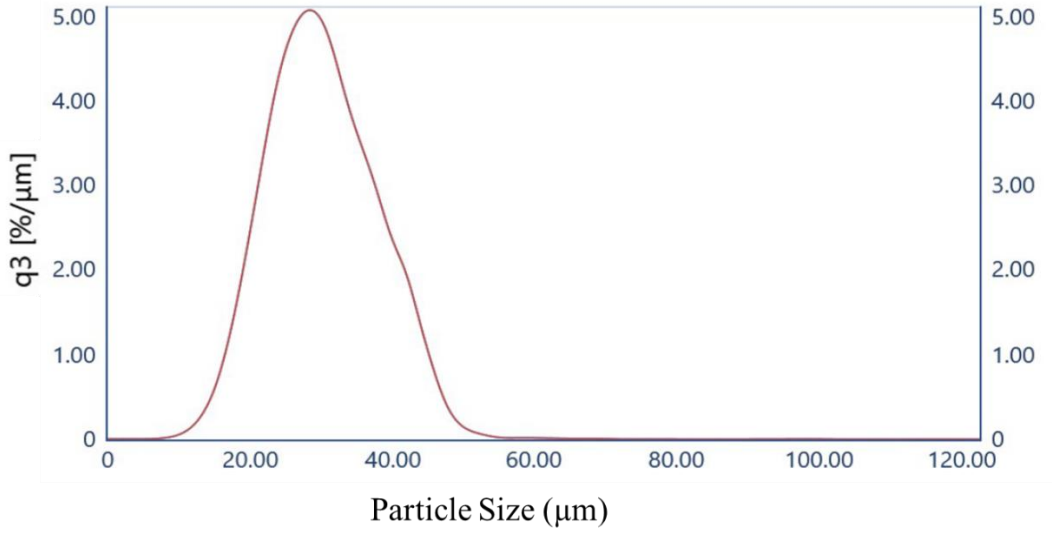

Figure 3-1 Particle size distribution curve

17-4 PH stainless steel additive manufacturing powders Scanning Electron Microscope (SEM) (FEI Nova Nano SEM 43) images were taken in order to check powders' sphericity. It is observed that most of the powders are spherical with some satellites. A sample of SEM images of the unused 17-4 PH stainless steel additive manufacturing powders and the chemical composition of the powders are given in

Figure 3-2. The chemical composition of the used powder material complied with Table 2-2 ASTM A564 chemical composition requirements.

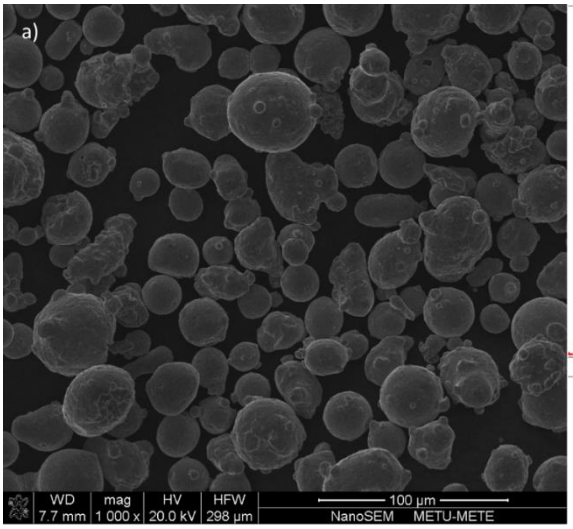

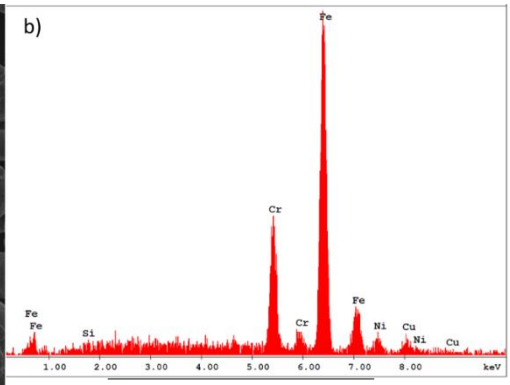

Element	Wt. %	At. %
Ni	4.51	4.23
Cr	17.08	18.10
Cu	4.86	4.21
Fe	71.87	70.88
Si	0.99	1.94

Figure 3-2 a) Powder SEM image b) Chemical composition of the 17-4 PH powder material

Powder analysis also was performed with X-Ray Diffraction (XRD) method. Rigaku MiniFlex 600 X-Ray Diffraction equipment with theta-theta goniometer is used for measurement. Copper K-alpha (Cu K-α) radiation is set between 20°-120° scan angle and scan speed 2°/min for all examinations. The calculated data and standard 17-4 PH powder material result is shown in Figure 3-3.

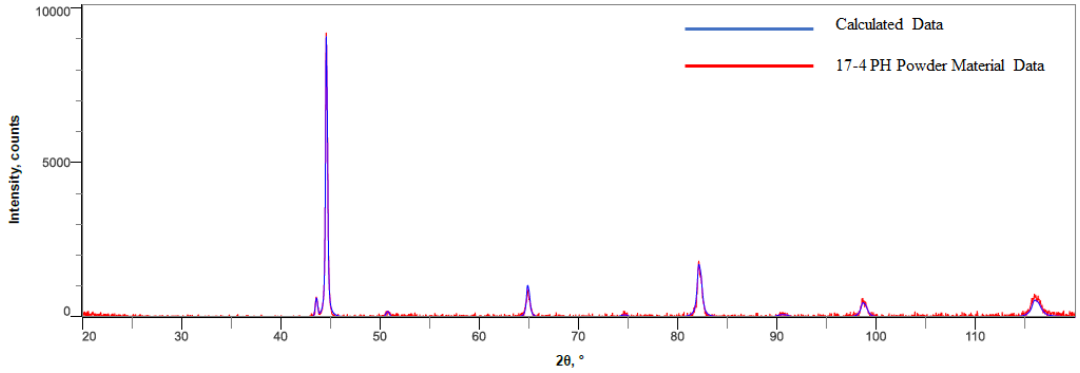

Figure 3-3 17-4 PH powder XRD analysis

3.2 Experimental Setup

3.2.1 Laser Powder Bed Fusion Equipment

Laser Powder Bed Fusion (LPBF) equipment which is given in Figure 3-4 (AM400, Renishaw, United Kingdom) was used to produce 17-4 PH alloy, residual stress measurement specimens. The build platform dimensions for Renishaw AM400 equipment are 250mm x 250mm x 300mm (width x height x depth). The interior of the equipment chamber can be seen in Figure 3-5. The interior of the platform is always protected from dirt and usage of other than 17-4 PH metallic powders is not allowed. Production of all specimens was performed under argon gas to keep oxygen level below 100ppm.

Figure 3-4 Renishaw AM400 laser powder bed fusion additive manufacturing equipment

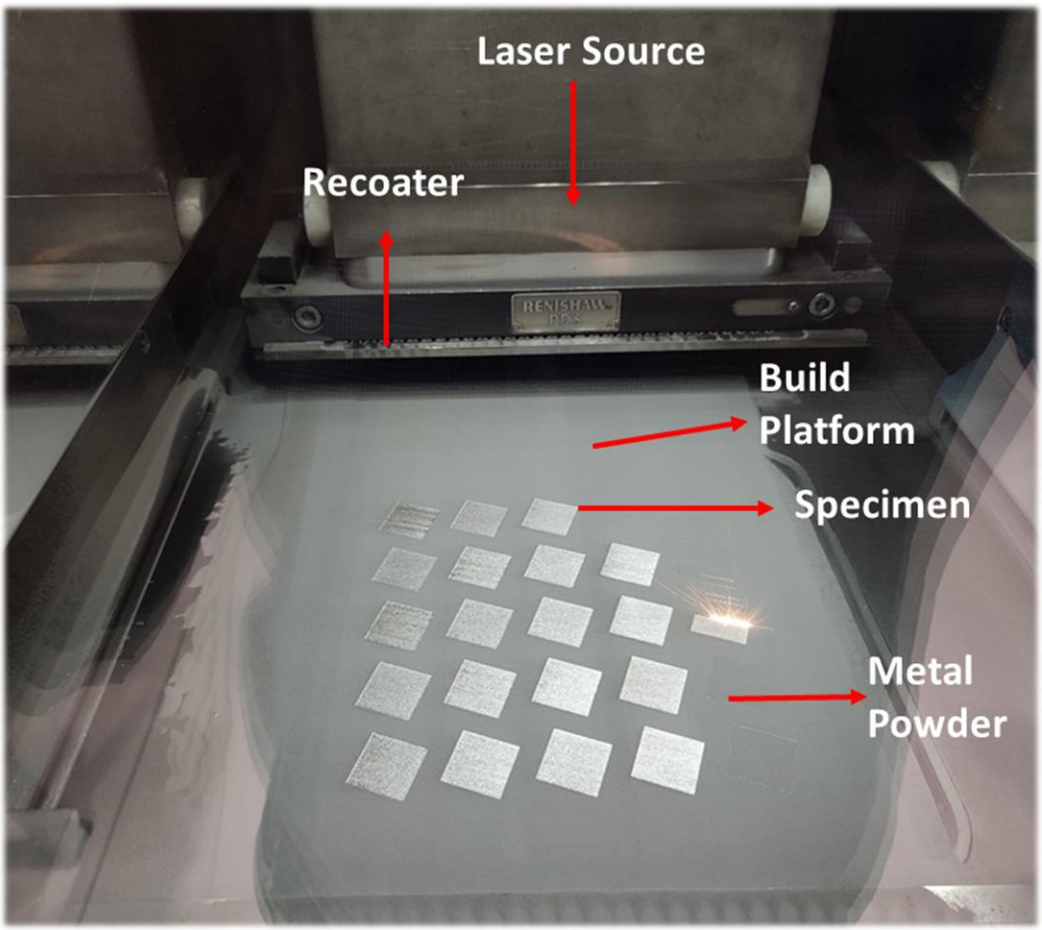

Figure 3-5 Renishaw AM400 laser powder bed fusion additive manufacturing equipment interior view

Renishaw AM400 laser powder bed fusion equipment has four types of scanning strategy capabilities which are namely Meander, Stripe, Chessboard and Total Fill The details about the scanning strategies are given in Section 2.1.1.1. Among these scanning strategies, Meander, Stripe and Chessbord scanning strategies are used for processing residual stress measurement specimens. The Total Fill scanning strategy is not used for residual stress measurement specimen production and analysis since this strategy creates a loose structure and is used for support structure production. The process parameters that are used for residual stress measurement specimens are given in Table 3-1 [24].

Table 3-1 Renishaw AM400 laser powder bed fusion equipment process parameters for scanning strategies

Specimen	Scanning Strategy	Power (watt)	Point Distance (µm)	Hatch Distance (µm)	Exposure Time (microsecond)	Layer Thickness (µm)
30-M	Meander	200	110	110	142	30
60-M	Meander	350	70	110	119	60
30-S	Stripe (width 7mm)	200	110	110	142	30
60-S	Stripe (width 7mm)	350	70	110	119	60
30-CB	Chessboard (field size 5mm^2)	200	110	110	142	30
60-CB	Chessboard (field size 5mm^2)	350	70	110	119	60

One of the other properties of Renishaw AM400 laser powder bed fusion equipment is having pulse mode building property. The details of the pulse mode laser properties are mentioned in Section 2.1.1.1. Chessboard specimen for 30µm layer thickness (30-CB) produced with 30µm Meander scanning strategy process parameters and Chessboard specimen for 60µm layer thickness (60-CB) produced with 60µm Meander scanning strategy process parameters as given in Table 3-1.

Materialise Magics software version 24.0 was used for 3D design file optimization and build preparation. Materialise Magics software for production setup for the design of experiment (DOE) specimen production is given in Figure 3-6.

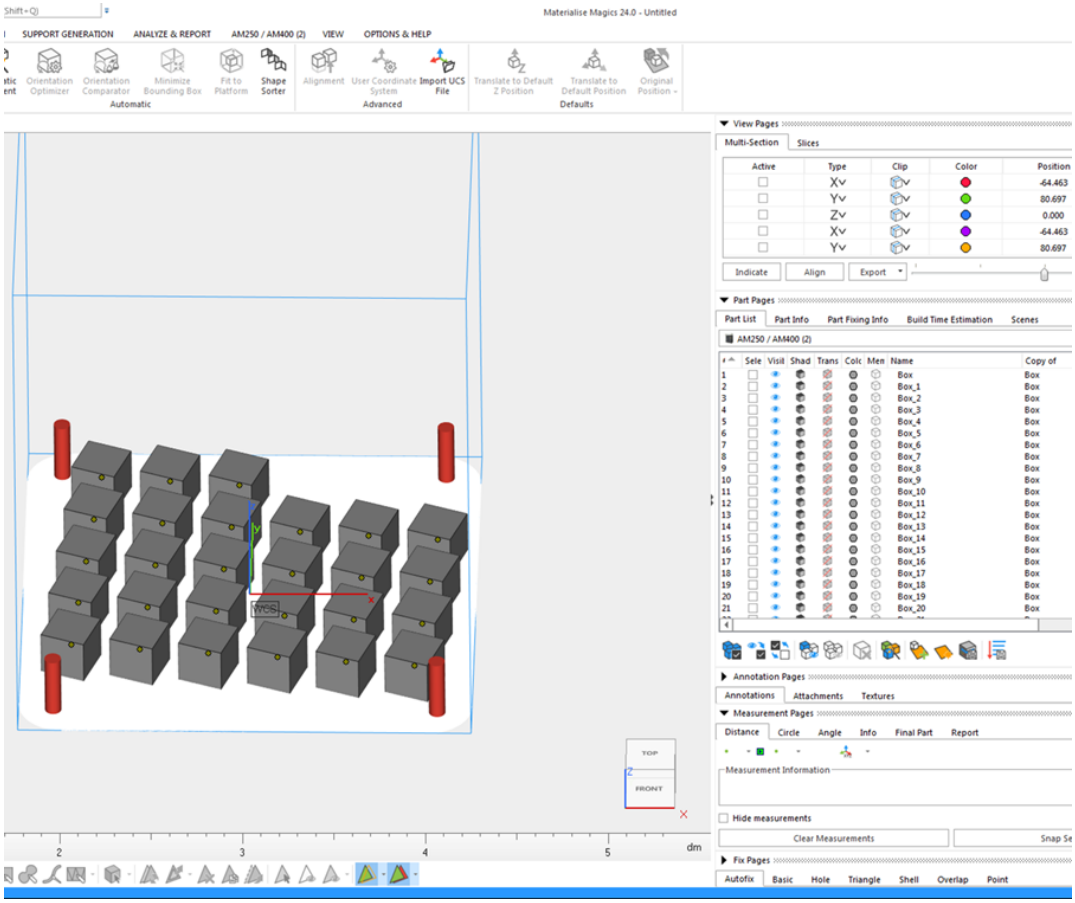

Figure 3-6 Materialise Magics software for production setup

The base plate of Renishaw AM400 was chosen as conventional carbon steel (AISI-1026, 98% Fe) and the base plate dimension was 250mm x 250mm with 20mm±2mm thickness.

3.2.2 X-Ray Diffraction Measurement Equipment

X-Ray Diffraction (XRD) residual stress measurements and retained austenite determination were utilized with Stresstech company product, Xstress_3000_G2R measurement device with XTronic software, version V1.14.0. The equipment is

compliant with European X-Ray residual stress testing standard EN 15305 which is given in Figure 3-7. Residual stresses were determined by the XRD method in accordance with ASTM E915 standard [68].

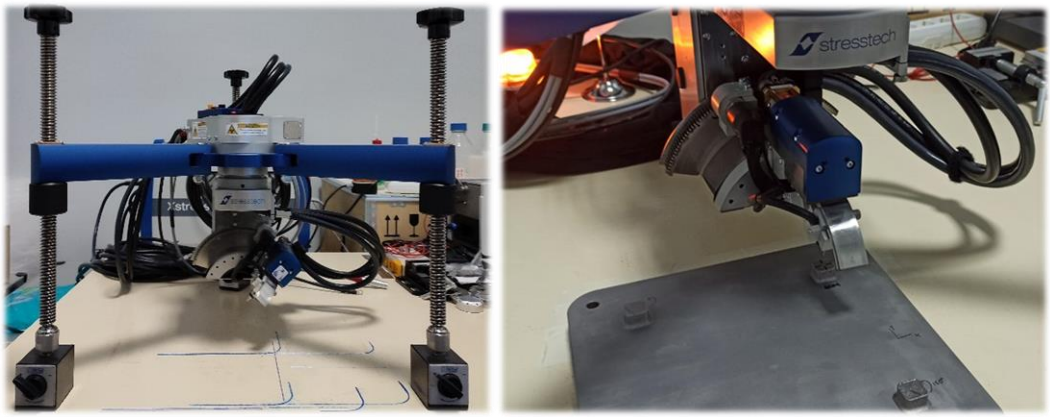

Figure 3-7 Stresstech, Xstress_3000_G2R Ray Diffraction (XRD) residual stress measurement equipment

Chromium (Cr) radiation with Kα wavelength 2,29 Å was used as the X-Ray source for measurements. X-Ray voltage current was set to 6,7mA, respectively. The collimator was 2mm in diameter and the distance between all samples and the collimator was 10mm. The detector distance was 50mm for all samples and the arc radius was 50mm. Exposure time was 10 seconds and the number of tilts was –8/+8, tilt angle -45°/+45° and tilt oscillation was 0°. Poisson's Ratio (v) and Modulus of Elasticity (E) values were 0,27 and 197 GPa selected respectively from Metallic Materials Properties Development and Standardization for 17-4 PH stainless steel specimens [69]. The device was calibrated by a stress-free iron reference sample. Stress values were calculated at 0°, 45° and 90° angles.

3.3 Electropolishing

Electropolishing was applied to residual stress specimens in order to get residual stress depth profile and investigate the process parameters' effect on additive manufacturing layers particularly for understanding the critical process parameters

such as laser power, scan speed, hatch distance, scanning strategy, layer thickness, exposure time, rotation effect etc.

The electropolish operation was performed with Struers Movipol-5 equipment and an A2 electrolyte (90 ml distilled water, 730 ml ethanol, 100 ml butoxyethanol, and 78 ml perchloric acid) for layer removal and depth profile measurements. A Mitutoyo micrometer gauge is used to measure the depth of the electropolished surface. The process setup is given in Figure 3-8.

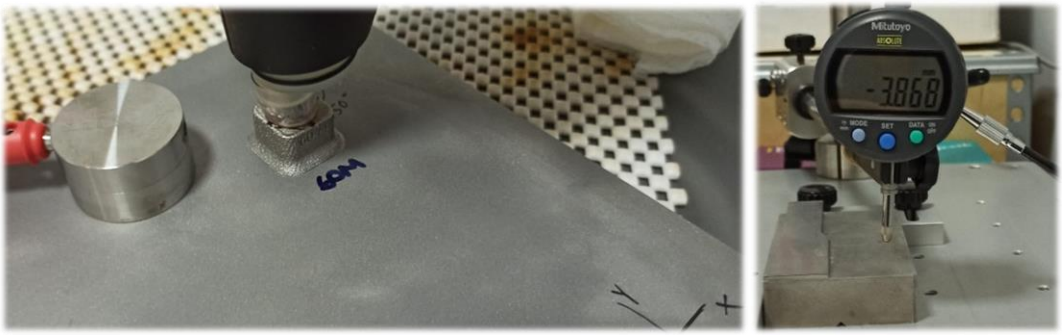

Figure 3-8 Electropolishing process setup

3.4 Sample Preparation

3.4.1 Control Specimens

H900 heat treated, bar formed in 1,5cm Ø, 17-4 PH stainless steel specimen compatible with ASTM A564 standard was used as a control specimen for residual stress measurement. Control specimens' results were shared and discussed in section 4.6. The residual stress control specimen was taken carefully from the bar specimen by EDM process in order to minimize additional residual stress exposition to the control specimen.

3.4.2 Residual Stress Measurement Specimen Production Plan

Residual stress measurement was performed on as-built 17-4 PH specimens, produced by LPBF process without any post processing including heat treatment, polishing, or any other surface treatment. Residual stress specimens were produced as given in Figure 3-9. Dimensions of the specimens were specified in Section 4.6.

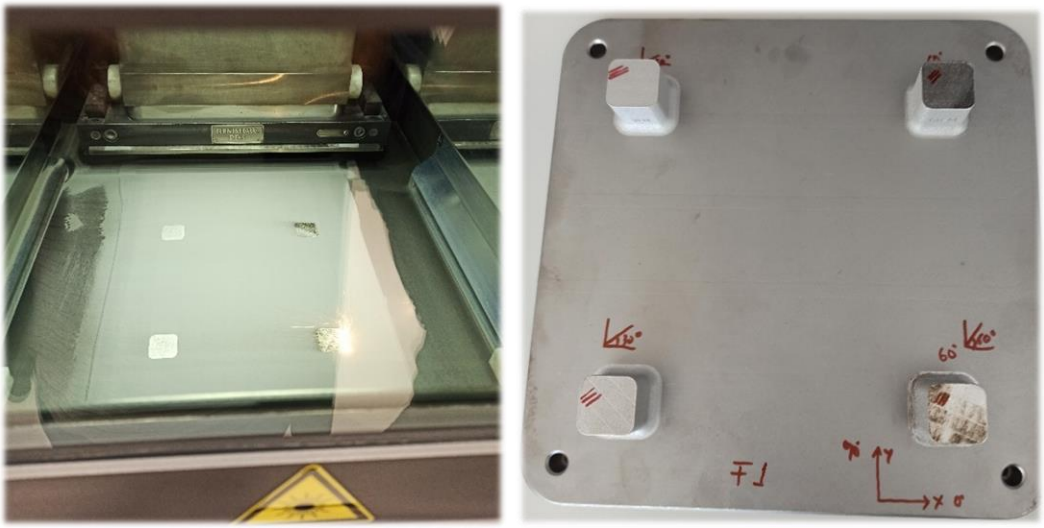

Figure 3-9 Specimen production by LPBF process.

Residual stress measurement specimens were used in order to examine the effect of scanning strategies, layer thickness, preheating of the baseplate, laser power, exposure time, volumetric energy density, hatch distance, point distance, separation from the base plate, height and area effect on surface and subsurface residual stresses by XRD residual measurement method.

3.4.3 Non-Destructive Testing

All specimens were non-destructively tested by Fluorescent Penetrant Inspection (FPI) method by ASTM E1417 [70] before mechanical or residual stress measurements. When there was a defect detected on specimens that can cause residual stress relief such as cracks or delamination, the defective specimens were

not evaluated for mechanical or residual stress measurements. An example of performed FPI tests can be seen for 60-S scanning strategies in Figure 3-10.

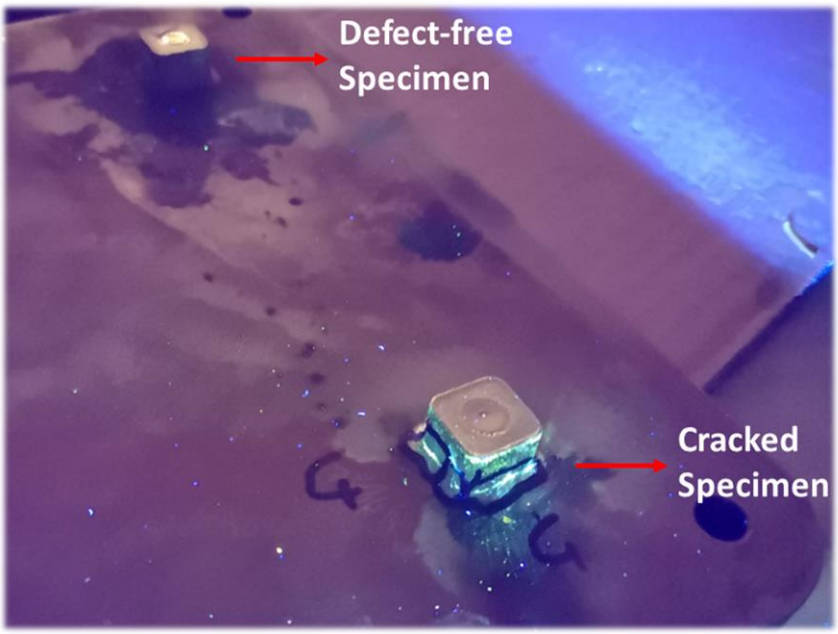

Figure 3-10 Fluorescent penetrant inspection test

3.5 Characterization

3.5.1 Chemical Composition Analysis

3.5.1.1 Optical Emission Spectrometer Analysis

Stationary metal analyzer, Optical Emission Spectrometer (OES) equipment (SPECTROMAXx, Germany) was used for chemical composition analysis on residual stress specimens. The obtained results were compared with the ASTM A564 standard chemical requirements and discussed in Section 4.1.3.

3.5.1.2 Scanning Electron Microscope, Energy Dispersive Spectroscopy (EDS) Analysis

Scanning Electron Microscope (SEM) (FEI Nova NanoSEM 430) was used for Energy Dispersive Spectroscopy (EDS) analysis. Chemical composition check by EDS analysis performed for produced specimens and used/unused powder materials. Local elements were enabled to be detected for specific areas of produced specimens and for used and unused powder materials.

3.5.2 Density Measurements

Density measurements were performed with Mettler-Toledo M304 type analytical balance equipment with a density kit. Pure water and three drops of foamdoctor F2887 (in order to minimize air bubbles) were used as the immersion liquid. The experiments were conducted at 20°C. All density measurements were utilized using Archimedes' Method in accordance with ASTM B-311 [71].

3.5.3 Metallographic Examination

3.5.3.1 Optical Microscope Images

Additive manufactured 17-4 PH stainless steel specimens were examined under Zeiss Axioscope-5 (Germany) optical microscope in order to examine the effect of process parameters on 17-4 PH stainless steel and to see melt pool boundaries and defect types. Residual stress specimens were cut into two pieces from the middle by Electro Discharge Machine (EDM) (Sodick/ALC 600G, United States of America) in order to perform metallographic examination from side view. Then the specimens are mounted, grinded, and polished respectively by an automated grinding & polishing equipment (Struers Tegramin, United States of America). The polished specimens were etched between 25-30 seconds by Fry's reagent which is prepared

in accordance with ASTM E 407 standard, etchant formula number 79 to clearly reveal the microstructure [72]. Cross-section of grain measurements was performed by ImageJ Analysis Software on metallography images. Metallography image analysis was performed to reveal the pulsed wave mode process parameters' effects on the specimen's cross-section of z-y plane for the LPBF process elongated grains.

3.5.3.2 Scanning Electron Microscope Images

Scanning Electron Microscope (SEM) (FEI Nova NanoSEM 430) was used for detailed 17-4 PH powder material images. Images for 17-4 PH powder material were obtained for powder sphericity and satellite formation control of used and unused powder material.

3.5.4 Mechanical Testing

3.5.4.1 Hardness Measurement

Hardness measurement was performed by DuraJet G5, Emco-Test (Kuchl, Germany) hardness test equipment. Tests were conducted on polished and flat surfaces of residual stress measurement samples from the top layer to the below direction with Vickers indenter by ASTM E 92 Standard [73]. Hardness measurement was performed with Vickers Hardness Number-HV 1 methods and converted into Rockwell C Hardness Number HRC by ASTM E 140 Standard [74]. 17-4 PH Stainless Steel specimen produced with 30µm layer thickness and meander scanning strategies was used for hardness measurement which has the highest densification and optimized tensile strength. The specimen was bakelite mounted and polished as in metallography operation. The zig-zag pattern was applied for hardness measurement as shown in Figure 3-11 to get more data from the specimen's top layer where tensile residual stresses affect can be observed. All the indentation distance was selected as more than two and a half times the length of the diagonal of the

impression to prevent additional plastic deformation. The diagonal length of each indentation was less than 0.1 mm.

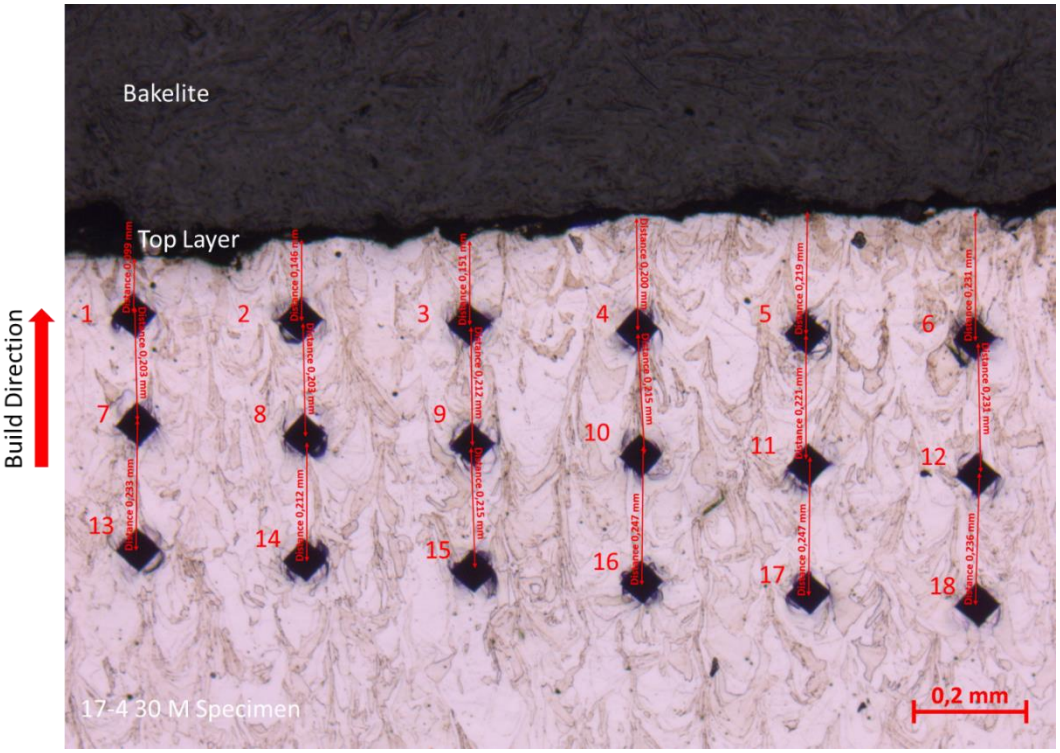

Figure 3-11 Hardness measurements close to top layer

3.5.4.2 Tensile Test

Tensile tests for 30µm layer thickness with meander scanning strategy were performed with Instron 5500R Universal Testing Machine (United States of America). For tensile tests, process parameters specified in Table 3-1 are used. The average tensile test results are given in section 4.2.1.2. Tensile tests were performed in accordance with ASTM E8m [75] sub-size tension test specimens at room temperature. The specimen dimensions are given in Figure 3-12.

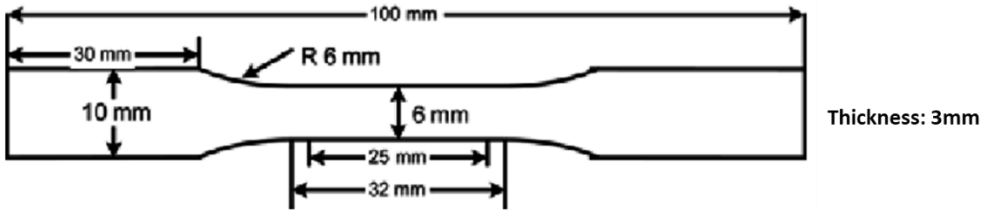

Figure 3-12 ASTM E8m sub-size tension test specimen dimensions [75]

Tensile test specimens were built in Z direction (build direction) and they were separated from the base plate by EDM. Generally, lower mechanical properties are obtained in Z direction for the LPBF process compared to X and Y direction due to having more exposure of layers' melting and solidification practice in a test specimen.

Tensile tests were performed with three repetitions as-built condition (heat treatment was not applied) and at room temperature for 30µm layer thickness, meander scanning strategy which has the highest densification rate and most commonly used parameter set.

3.5.5 Modulus of Elasticity & Poisson's Ratio Determination by Ultrasonic Flaw Detector

Olympus EPOCH 650 (Japan) ultrasonic flaw detector with contact transducer was used for Young's Modulus of Elasticity (E) and Poisson's Ratio (ν) determination of additive manufactured residual stress specimens by ultrasonic pulse-echo technique. This technique allows isotropic and homogeneous materials sound velocity measurement which can contribute to both Young's Modulus of Elasticity and Poisson's Ratio calculation. In longitudinal and shear modes, separate transducers were used for pulse-echo sound velocity measurements. Ultrasonic flaw detector and contact transducer instruments used for measurements are given in Figure 3-13.

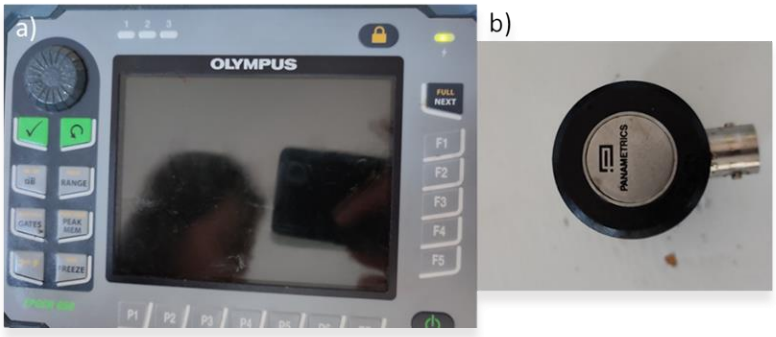

Figure 3-13 a) Olympus EPOCH 650 (Japan) ultrasonic flaw detector and b) contact transducer

The thickness of the residual stress measurement samples was measured and round-trip transit time was recorded with both shear and longitudinal wave transducers. Shear (transverse) and longitudinal velocity were calculated by *Equation 7* where the thickness of the 17-4 PH residual stress specimens was measured by caliper after they were separated from base plate material from the bottom by wire EDM process as shown in Figure 3-14.

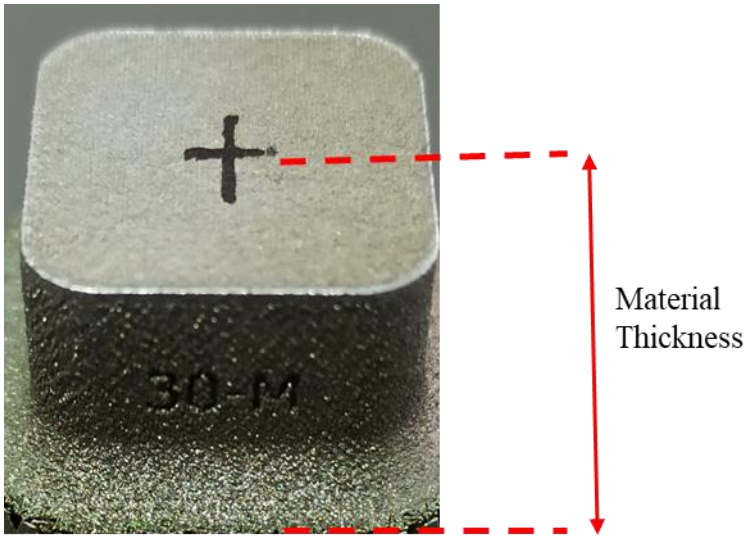

Figure 3-14 Material thickness measurement for 17-4 PH residual stress specimens

Transit time is divided by two since the ultrasonic sound trips to the bottom of the material and comes back [76].

$$Velocity = \frac{Thickness}{Round\ trip\ transit\ time\ /\ 2} \qquad \textit{Equation 7}$$

Then, with the values of shear and longitudinal velocity values Poisson's Ratio is calculated with given *Equation 8* [76].

$$Poisson's\ Ratio\ (v) = \frac{1 - 2\,(\frac{V_T}{V_L})^2}{2 - 2\,(\frac{V_T}{V_L})^2} \qquad \textit{Equation 8}$$

*V_T: *Shear* (transverse) velocity, V_L: Longitudinal Velocity

Young's Modulus of Elasticity was calculated by *Equation 9* and shear modulus by *Equation 10* [76].

$$Young's\ Modulus\ (E) = \frac{{V_L}^2 * \rho * (1 + v) * (1 - 2v)}{1 - v} \qquad \textit{Equation 9}$$

$$Shear\ Modulus = {V_T}^2 * \rho \qquad \textit{Equation 10}$$

3.6 Simulation

Residual stress simulation was performed with commercial Simufact Additive (Hexagon, Germany) software. This simulation software was developed for the Powder Bed Fusion Additive Manufacturing process for metal part productions. It also provides part production optimization at some level. Simufact Additive simulation can be performed when calibration data is obtained, as discussed in section 2.1.1.1. Calibration data is used for simulation software to analyze the additive manufacturing specimens. 17-4 PH stainless steel cantilever specimens were built by Renishaw AM400, pulsed mode laser powder bed fusion additive manufacturing equipment with 30µm layer thickness, meander scanning strategy process parameters as shown in Figure 2-6. The distortion level was measured for each cantilever from the points stated in Figure 3-15 by a Coordinate Measuring Machine (CMM) (Hexagon Global Advantage, Swiss).

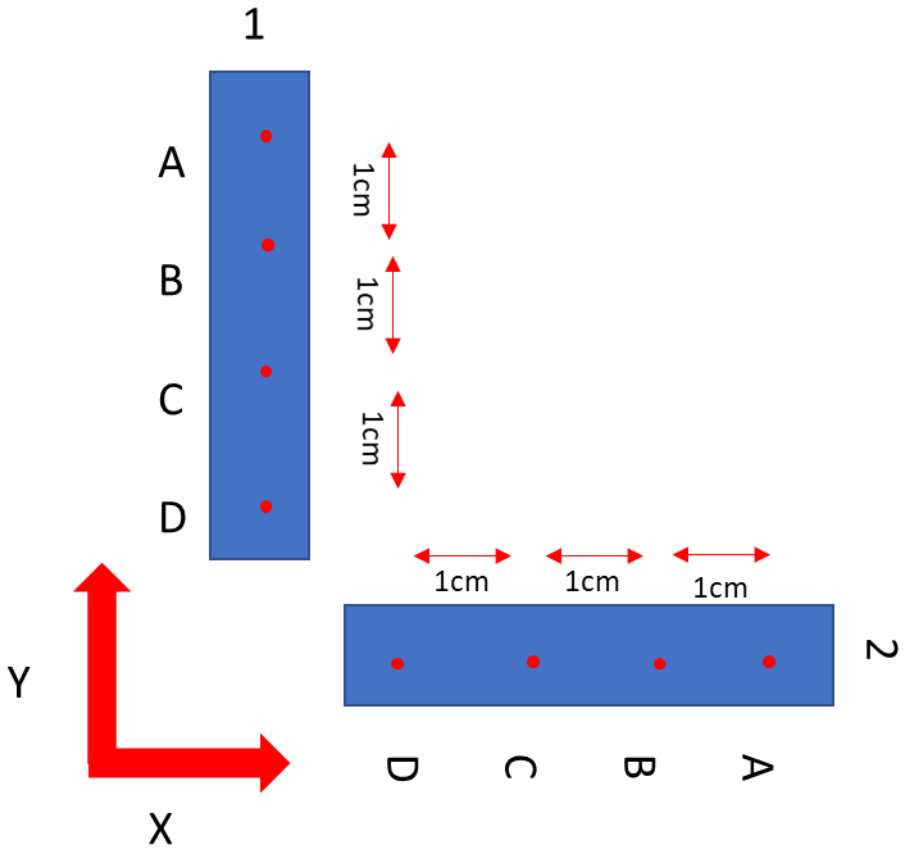

Figure 3-15 Orientation of the calibration cantilevers and representation of distortion measurement points

Cantilever calibration data for Simufact Additive Simulation software is given in Table 3-2. Distortions are measured by coordinate measuring machines. Obtaining calibration data takes some time, and Simufact Additive simulation software cannot be used without calibration data.

Table 3-2 Cantilever calibration data for simulation software

Measurement Points	Part 1		Part 2	
	Measurement in Z Direction	Relative Distortion (Ref D)	Measurement in Z Direction	Relative Distortion (Ref D)
A	10.4	1.7	10.3	1.6
B	9.8	1.1	9.7	1.0
C	9.3	0.6	9.3	0.6
D	8.7	0	8.7	0

CHAPTER 4

RESULTS AND DISCUSSION

4.1 Characterization

4.1.1 Metallographic Examination

Microstructure of the 17-4 PH specimens produced with different scanning strategies was examined by a) 5X, b) 10X, c) 20X and d) 100X magnification are given for namely; 30µm layer thickness with meander scanning strategy (30-M), 30µm layer thickness with stripe scanning strategy (30-S), 60µm layer thickness with meander scanning strategy (60-M), 60µm layer thickness with stripe scanning strategy (60-S) and for preheat at 170°C conditions. The scanning strategies are indicated in Table 3-1 and scanning strategies are explained in detail on section 2.1.1.1. All metallographic images were taken from the z-y plane (in the build direction).

Retained austenite formation does not occur for 17-4 PH stainless steel production by Laser Powder Bed Fusion (LPBF) process. Retained γ (austenite) could not be detected by XRD method and the structure has almost fully ferritic microstructure in the as-built condition. Retained austenite does not form due to the high heating and cooling rates (10^5-10^6 K/s) of the LPBF process as it was discussed in detail by Alnajjar et al [77]. 17-4 PH stainless steel solidifies immediately to stable δ (delta) ferrite phase and further metallurgical change does not occur during all the thermal cycles. δ ferrite to γ (austenite) phase transformation does not occur due to lack of time which is called austenite by-passing [77]. Therefore, γ (austenite) phase to martensite transformation also cannot occur and the structure has almost fully ferritic microstructure.

Grain boundaries are accepted as defects in the crystal structure. Finer grains can prevent or retard dislocation motion and improve the strength of the material. The LPBF process has unique grain characteristics. The grain characteristics of 30-M, 30-S, 60-M and 60-S analyzed in horizontal and vertical directions due to the nature of melting and solidification of each layer. The metallography images provided like raindrops' bottom effect images on the z-y plane cross-section by having elongated grains along the build direction as shown in Figure 2-8. Although cross-sectioning through the scanning line might not be possible, the images of each grain resemble a cross-section of each pulse mode effect of each laser shot. 3-D image analysis might be preferred for a detailed examination of the LPBF process [78]. Grains are more elongated in built direction for 60µm layer thickness process parameters compared to 30µm layer thickness as expected. Chessboard scanning strategy microstructures are not added deliberately by knowing the process parameters with meander scanning strategies applied.

4.1.1.1 30µm Layer Thickness with Meander Scanning Strategy (30-M)

Metallographic examination of 30µm layer thickness with meander scanning strategy (30-M) is given in Figure 4-1. Build direction is through the top of the figure. Anisotropic microstructure having elongated along the build direction and pulsed wave effect can be observed in the micrographs.

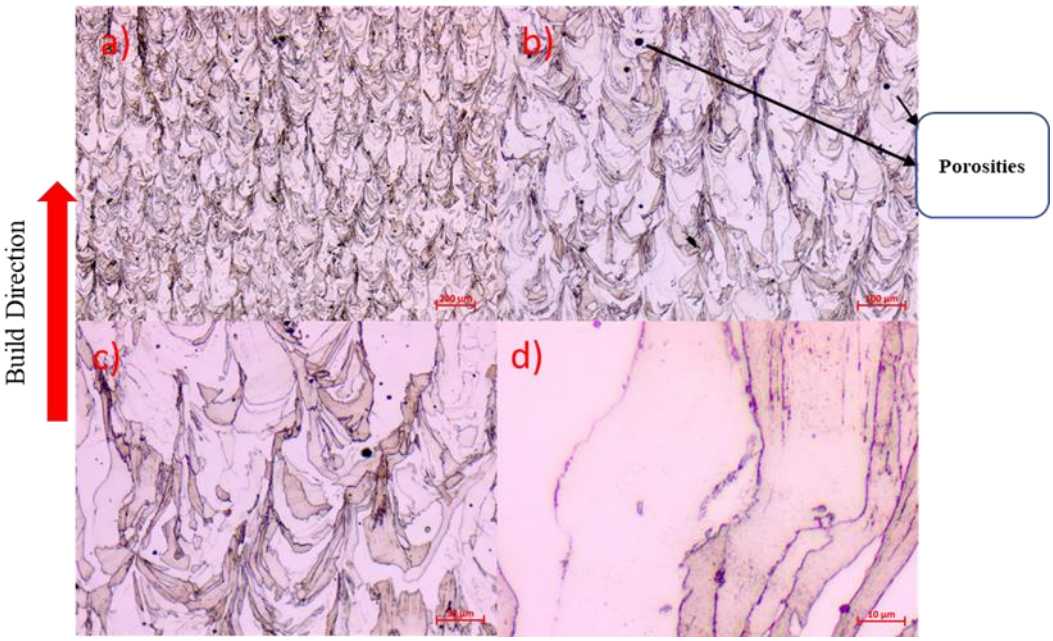

Figure 4-1 30µm layer thickness with meander scanning strategy (30-M) micrographs

The horizontal measurements of the image for the 30-M specimen were analyzed particularly for point distance and volumetric energy density (VED) effects. The cross-section of the specimen on z-y plane indicated about four grain cross-section in ~480µm where point distance is 110µm and VED is 78 J/mm3. The vertical measurements of the image for the 30-M specimen were analyzed for layer thickness, VED, laser power, and exposure time. In the horizontal line, twelve raindrops' bottom effect was observed in ~350µm where layer thickness is 30µm. The gas and keyhole porosities that formed in the 30-M specimen can be seen in Figure 4-1.

4.1.1.2 30µm Layer Thickness with Stripe Scanning Strategy (30-S)

Metallographic examination of 30µm layer thickness with stripe scanning strategy (30-S) is given in Figure 4-2.

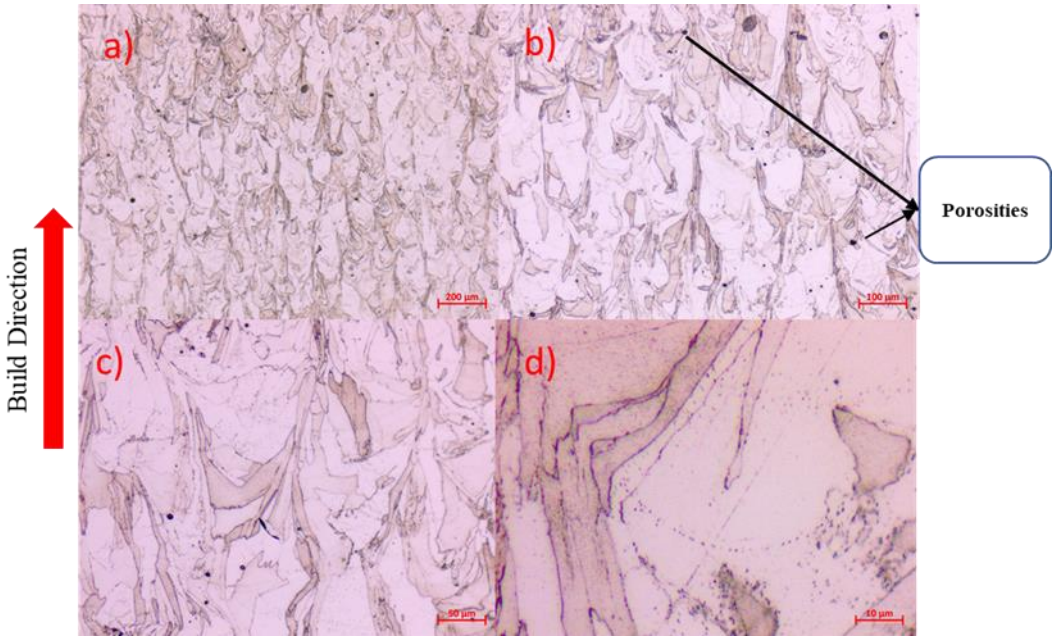

Figure 4-2 30µm layer thickness with stripe scanning strategy (30-S) micrographs

The horizontal measurements of the image for the 30-S specimen were analyzed particularly for point distance and volumetric energy density (VED) effects. The cross-section of the specimen on z-y plane indicated about three grain cross-section in ~340µm where point distance is 110µm and VED is 78 J/mm3. The vertical measurements of the image for the 30-S specimen were analyzed for layer thickness, VED, laser power, and exposure time. In the horizontal line, seven raindrops' bottom effect was observed in ~200µm where layer thickness is 30µm. The gas and keyhole porosities that formed in the 30-S specimen can be seen in Figure 4-2.

4.1.1.3 60µm Layer Thickness with Meander Scanning Strategy (60-M)

Metallographic examination of 60µm layer thickness with meander scanning strategy (60-M) is given in Figure 4-3.

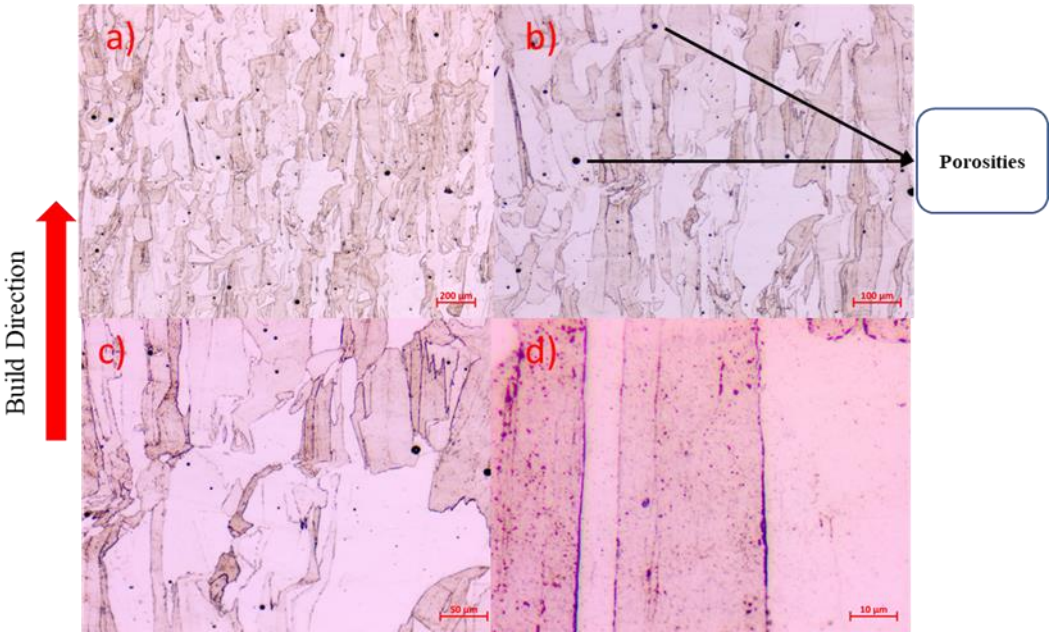

Figure 4-3 60µm layer thickness with meander scanning strategy (60-M) micrographs

The horizontal measurements of the image for the 60-M specimen were analyzed particularly for point distance and volumetric energy density (VED) effects. The cross-section of the specimen on z-y plane indicated about six grain cross-section in ~440µm where point distance is 70µm and VED is 90J/mm3. The vertical measurements of the image for the 60-M specimen were analyzed for layer thickness, VED, laser power, and exposure time. In the horizontal line, five raindrops' bottom effect was observed in ~290µm where layer thickness is 60µm. The gas and keyhole porosities that formed in the 60-M specimen can be seen in Figure 4-3.

4.1.1.4 60µm Layer Thickness with Stripe Scanning Strategy (60-S)

Metallographic examination of 60µm layer thickness with stripe scanning strategy (60-S) is given in Figure 4-4.

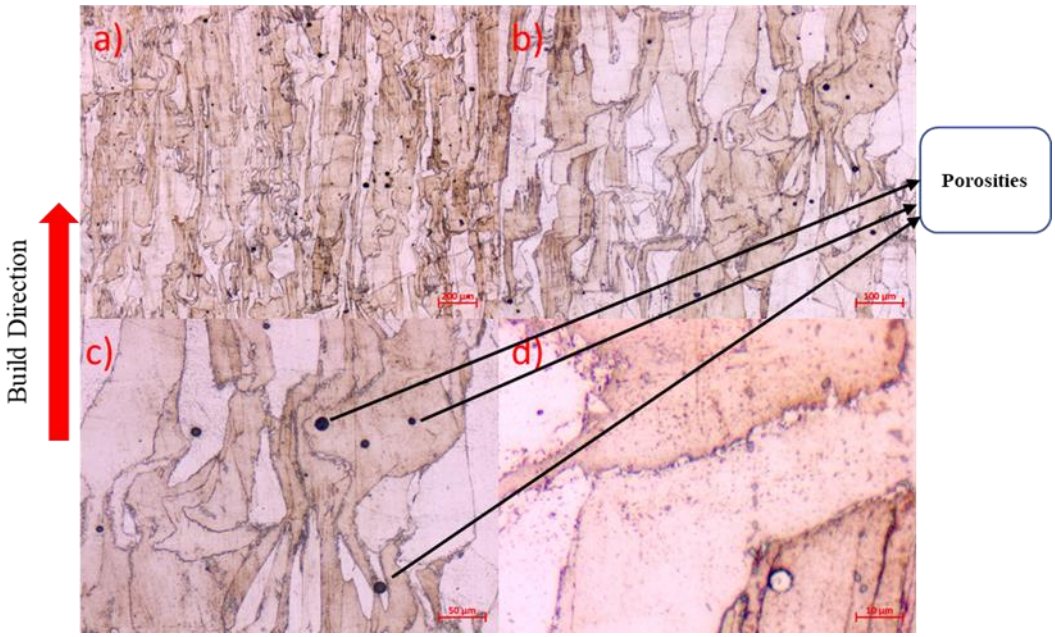

Figure 4-4 60µm layer thickness with stripe scanning strategy (60-S) micrographs

The horizontal measurements of the image for the 60-S specimen were analyzed particularly for the point distance and volumetric energy density (VED) effects. The cross-section of the specimen on z-y plane indicated about four grain cross-section in ~290µm where point distance is 70µm and VED is 90J/mm3. The vertical measurements of the image for the 60-S specimen were analyzed for layer thickness, VED, laser power, and exposure time. In the horizontal line, two raindrops' bottom effect was observed in ~120µm where layer thickness is 60µm. The gas and keyhole porosities that formed in the 60-S specimen can be seen in Figure 4-4.

4.1.1.5 30µm Layer Thickness with Meander Scanning Strategy (30-M) – Preheat at 170°C

Metallographic examination of 30µm layer thickness with meander scanning strategy (30-M) and preheating applied to the base plate at 170°C is given in Figure 4-5.

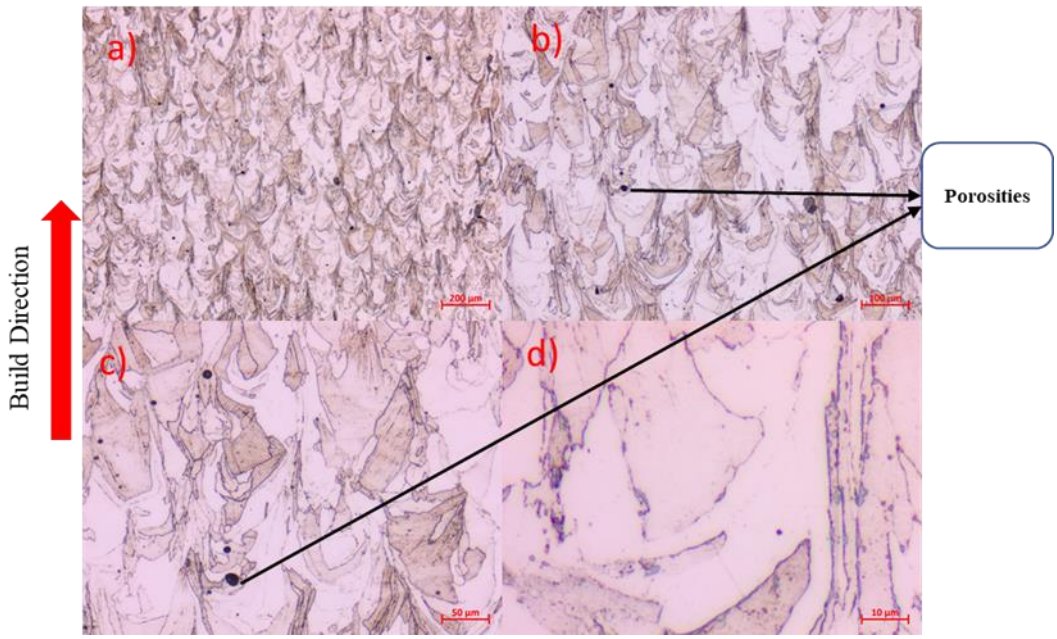

Figure 4-5 30µm layer thickness with meander scanning strategy (30-M) and preheating applied at 170°C micrographs

The horizontal measurements of the image for the 30-M Preheated specimen at 170°C were analyzed particularly for point distance and volumetric energy density (VED) effects. The cross-section of the specimen on z-y plane indicated about four grain cross-section in ~490µm where point distance is 110µm and VED is 78 J/mm3. The vertical measurements of the image for the 30-M Preheated specimen were analyzed for layer thickness, VED, laser power, and exposure time. In the horizontal line, six raindrops' bottom effect was observed in ~170µm where layer thickness is 30µm. The gas and keyhole

porosities that formed in the 30-M Preheat specimen can be seen in Figure 4-5.

4.1.1.6 30µm Layer Thickness with Stripe Scanning Strategy (30-S) – Preheat at 170°C

Metallographic examination of 30µm layer thickness with stripe scanning strategy (30-S) and preheating applied at 170°C is given in Figure 4-6. The horizontal measurements of the image for the 30-S Preheated specimen at 170°C were analyzed particularly for point distance and volumetric energy density (VED) effects. The cross-section of the specimen on z-y plane indicated about two grain cross-section in ~240µm where point distance is 110µm and VED is 78 J/mm3. The vertical measurements of the image for the 30-S Preheated specimen were analyzed particularly for the layer thickness, VED, laser power, and exposure time. In the horizontal line, four raindrops' bottom effect was observed in ~120µm where layer thickness is 30µm. The gas and keyhole porosities that formed in the 30-S Preheat specimen can be seen in Figure 4-6.

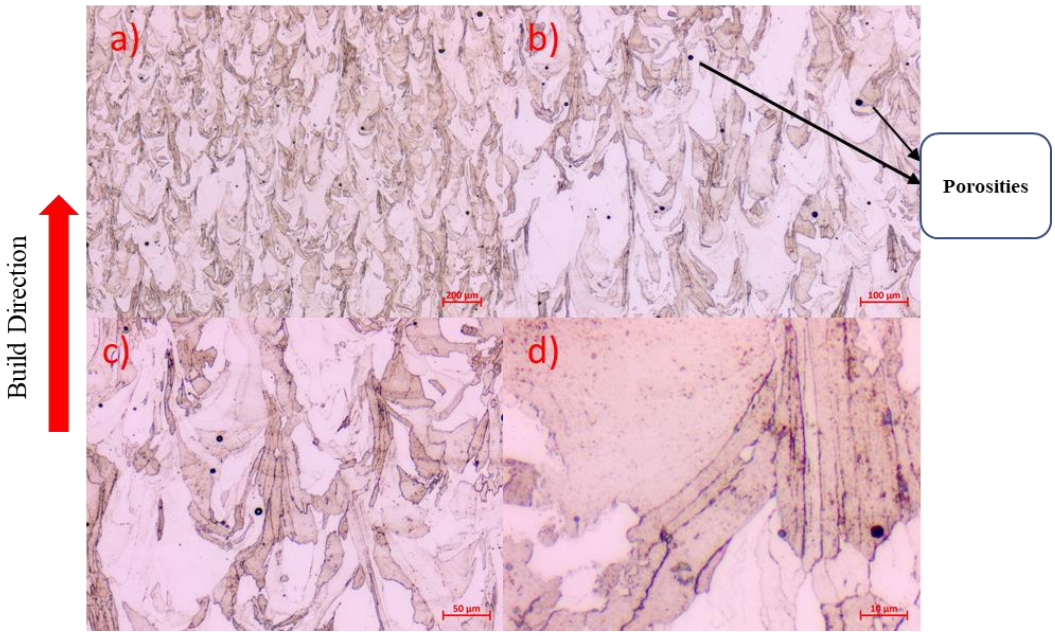

Figure 4-6 30µm layer thickness, stripe scanning strategy (30-S) and preheating applied at 170°C micrographs

4.1.1.7 60µm Layer Thickness with Meander Scanning Strategy (60-M) – Preheat at 170°C

Metallographic examination of 60µm layer thickness with meander scanning strategy (60-M) and preheating applied at 170°C is given in Figure 4-7. The horizontal measurements of the image for the 60-M Preheated specimen at 170°C were analyzed particularly for point distance and volumetric energy density (VED) effects. The cross-section of the specimen on z-y plane indicated about five grain cross-section in ~370µm where point distance is 70µm and VED is 90J/mm3. The vertical measurements of the image for the 60-M Preheated specimen were analyzed particularly for the layer thickness, VED, laser power, and exposure time. In the horizontal line, five raindrops' bottom effect was observed in ~290µm where layer thickness is 60µm. The

gas and keyhole porosities that formed in the 60-M Preheated specimen can be seen in Figure 4-7.

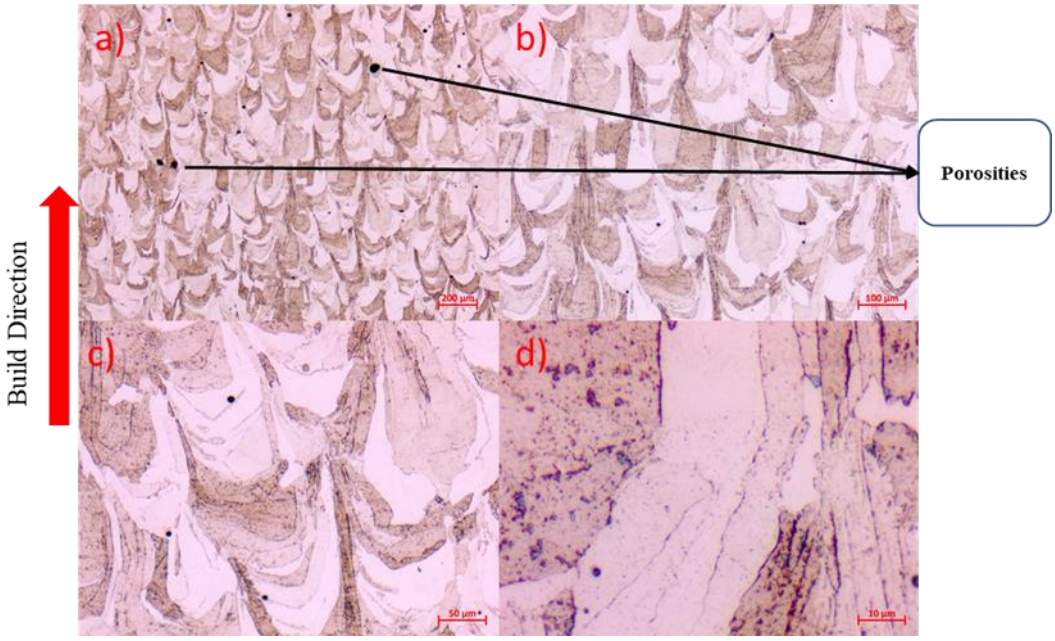

Figure 4-7 60µm layer thickness with meander scanning strategy (60-M) and preheating applied at 170°C micrographs

4.1.1.8 60µm Layer Thickness with Stripe Scanning Strategy (60-S) – Preheat at 170°C

Metallographic examination of 60µm layer thickness with stripe scanning strategy (60-S) and preheating applied at 170°C is given in Figure 4-8. The horizontal measurements of the image of the 60-S Preheated at 170°C specimen were analyzed particularly for the point distance and volumetric energy density (VED) effects. The cross-section of the specimen on z-y plane indicated about five grain cross-section in ~400 µm where point distance is 70µm and VED is 90J/mm3. The vertical measurements of the image for the 60-S Preheated specimen were analyzed for layer thickness, VED, laser power, and exposure time. In the horizontal line, six raindrops'

bottom effect was observed in ~340µm where layer thickness is 60µm. The gas and keyhole porosities that formed in the 60-S Preheated specimen can be seen in Figure 4-8

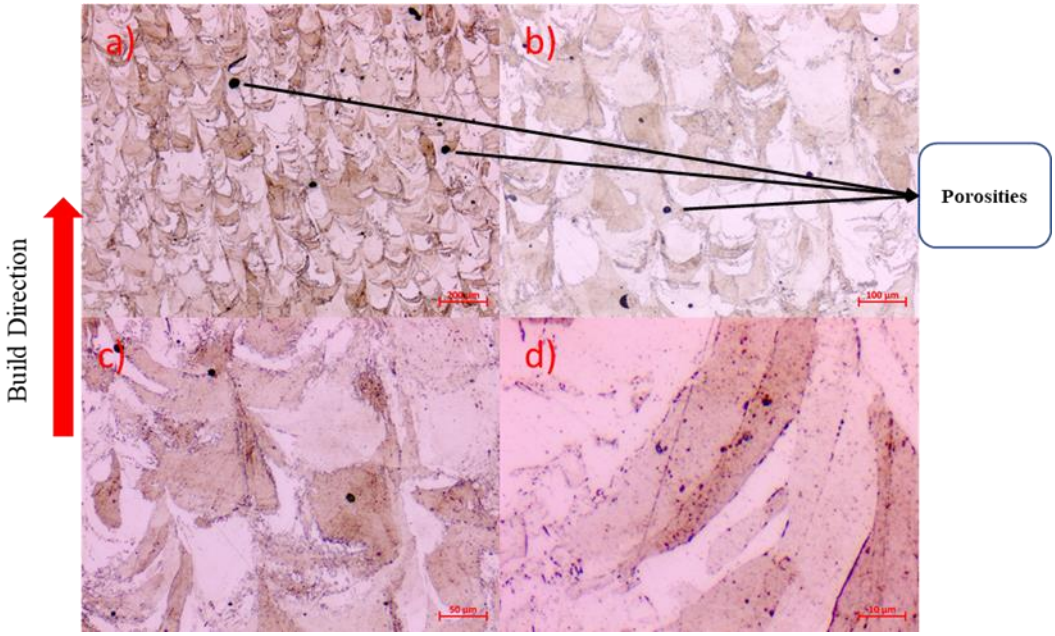

Figure 4-8 60µm layer thickness with stripe scanning strategy (60-S) and preheating applied at 170°C micrographs

Preheating by 170°C micrograph images of 30-M, 30-S, 60-M, and 60-S were examined and compared with standard 30-M, 30-S, 60-M, and 60-S specimens. There were not many specific changes in the microstructure images due to the base plate preheating effect. Preheating also does not play a change in martensite formation since the phase does not form austenite phase by the LPBF process due to high phase transformation rates as explained by Alnajjar et al. [77].

The 60-M process parameter' VED value is 15% higher than the 30-M process parameter's VED value. The 60-M's 15% more VED value with 75% higher laser power with 36% shorter point distance was used to melt 100% thicker layer thickness compared to 30-M specimens.

Retained austenite could not be detected by XRD method. On the other hand, layer thickness effects on metallographic images can be distinguished easily. The 60µm layer thickness specimen's shape of the grains is sharper and more elongated to the down side of the material. Furthermore, 30µm layer thickness with meander scanning strategy (30-M) has the lowest porosity rates on images as given in Figure 4-1. Density measurement results also validate this finding where the 30-M scanning strategy has the highest densification ratio with over 99.5% relative density and where density details are given in section 4.3. 30µm layer thickness with meander scanning strategy also has the most desirable metallographic images by having expected and ideal grain structure for 17-4 PH stainless steel produced by the LPBF process.

4.1.2 Scanning Electron Microscope (SEM)- Energy Dispersive Spectroscopy (EDS) Analysis

Energy Dispersive Spectroscopy (EDS) analysis was performed by Scanning Electron Microscope (SEM) to check the color variance observed on optical microscope images as shown in Figure 4-9. There were no significant phase changes by EDS. The color differences can be interpreted as, due to the nature of the Laser Powder Based Fusion proses.

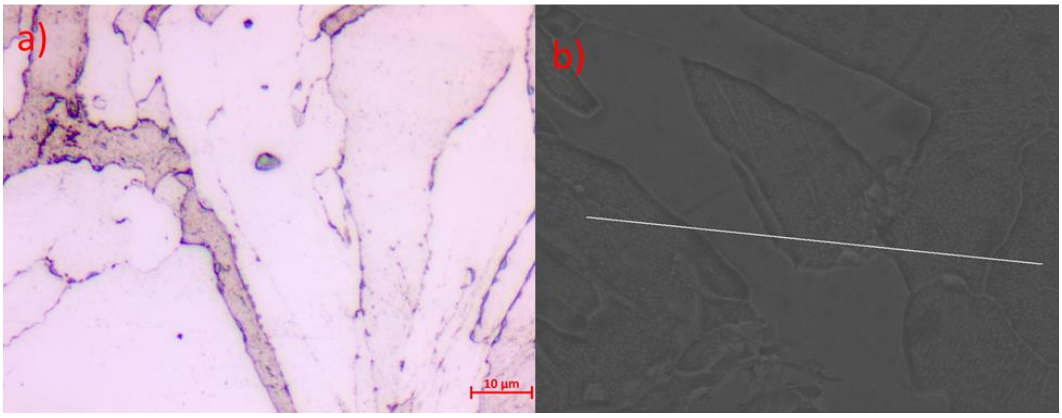

Figure 4-9 Energy Dispersive Spectroscopy (EDS) line analysis

Segregation-suspected dark areas other than porosities were also examined by EDS analysis. The EDS result for the segregation suspected dark areas is given in Figure 4-10 and the EDS analysis of the result of parent material is given in Figure 4-11. The chemical composition of the segregation suspected dark areas were slightly different than for Ni, Cu, and Cr elements of Table 2-2 ASTM A564 chemical composition requirements. Alnajjar et al.'s study support this result that precipitation of carbides or sulfides does not exist in the LPBF process of 17-4 PH stainless steel, and SEM mapping shows homogenous distribution of Ni, Cu, Fe, and Cr elements [77].

The chemical composition of the used powder material given in Figure 3-2 and parent material EDS results shared in Figure 4-11 were compatible with Table 2.2 ASTM A564 chemical composition requirements.

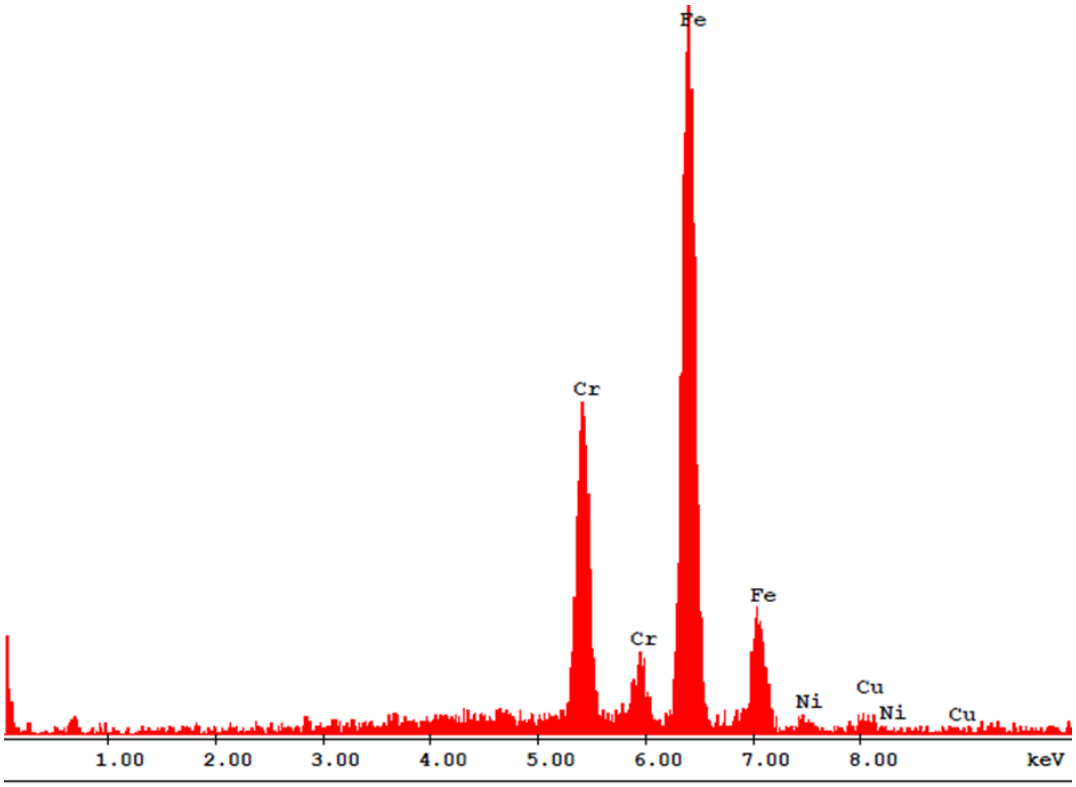

Element	Wt. %	At. %
Ni	1.93	1.82
Cr	20.44	21.73
Cu	3.25	2.83
Fe	74.38	73.63

Figure 4-10 Segregation suspected dark areas EDS analysis result

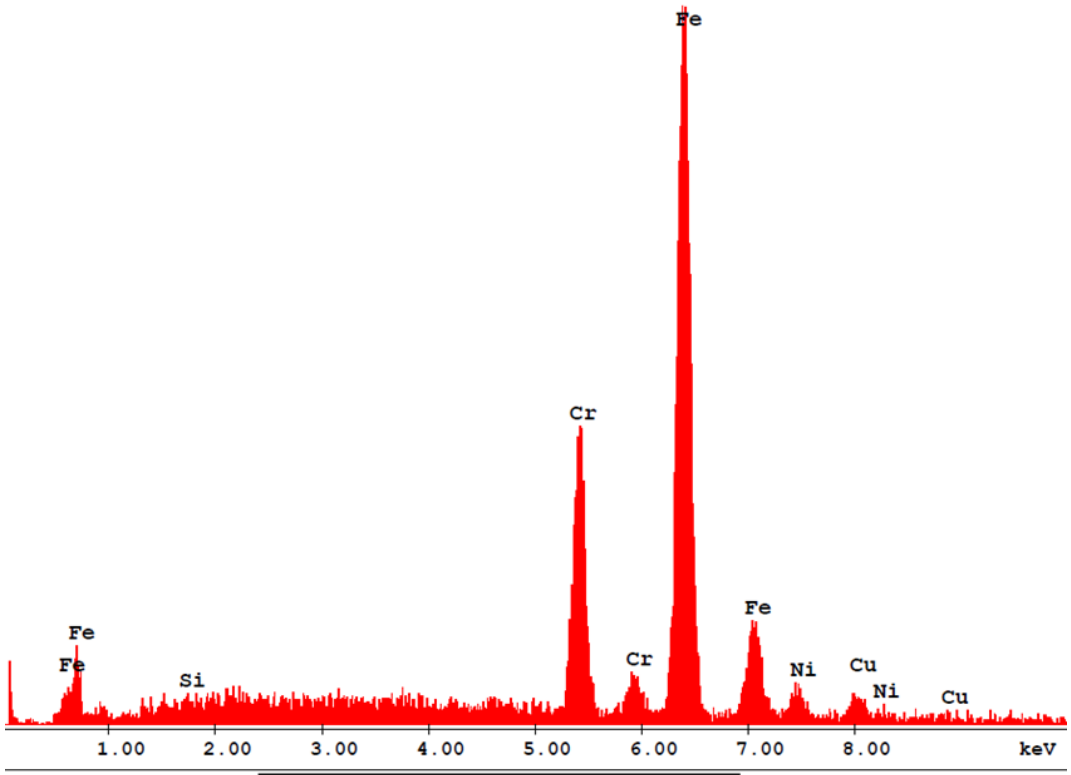

Element	Wt. %	At. %
Ni	4.81	4.53
Cr	17.19	18.21
Cu	4.98	4.24
Fe	72.14	71.19
Si	0.93	1.82

Figure 4-11 EDS analysis result of parent material

4.1.3 Optical Emission Spectroscopy Analysis

Optical Emission Spectroscopy (OES) results are compared with the ASTM A564 standard [42]. All Samples of residual stress specimens conform to the chemical composition percentages by weight. Four measurements are taken from each sample by optical emission spectroscopy, and all measurements are within the limits of

ASTM A564. The average values of four measurement results are given in Table 4-1 for only one representative sample.

Table 4-1 Optical emission spectroscopy, chemical composition analysis comparison table (composition percentages by weight) [42].

ASTM A564			Optical Emission Measurement
Element	**Min**	**Max**	**Average**
Carbon	-	0.07	0.01
Manganese	-	1	0.20
Silicon	-	1	0.60
Phosphorus	-	0.04	<0.0005
Sulfur	-	0.03	<0.0005
Chromium	15	17.5	16.60
Nickel	3	5	4.45
Columbium +Tantalum	0.15	0.45	0.25
Copper	3	5	3.85
Iron	Balance		Balance

4.2 Mechanical Testing

4.2.1.1 Hardness Measurement

17-4 PH stainless steel specimen produced with 30µm layer thickness and meander scanning strategies hardness measurement results were given in Table 4-2. The obtained hardness values were between 28,5 and 31 HRC which fits with the hardness values of conventionally produced 17-4 PH bar-formed specimens in H1150 and H1100 conditions as given in Table 2-1. The mechanical properties stated in Table 2-1 were in solution heat treated and precipitation hardened condition and

the hardness values of additively manufactured 17-4 PH stainless steel specimen produced with 30µm layer thickness and meander scanning strategies were in as-built conditions. Therefore, having hardness properties even in as-built condition can be accepted at a reasonable level for additively manufactured specimens.

Table 4-2 17-4 PH stainless steel specimen top layer hardness measurement results

Hardness Indentation No (*Figure 3-11)	**Vickers Hardness Number (HV-1)**	**Rockwell C Hardness Number 150 kgf (HRC)**
1	291	29
2	301	31
3	302	31
4	296	30
5	299	30
6	301	31
7	293	29
8	297	30
9	289	29
10	299	30
11	289	29
12	301	31
13	297	30
14	296	30
15	301	31
16	293	29
17	294	29
18	293	29

The trend between residual stress measurements and hardness values are tried to be correlated and analyzed by trying to obtain more data from the top layer as stated in Section 3.5.4.1. However, there was no substantial change in hardness values as shown in Figure 4-12. The hardness indentation number and illustration are shared in Figure 3-11.

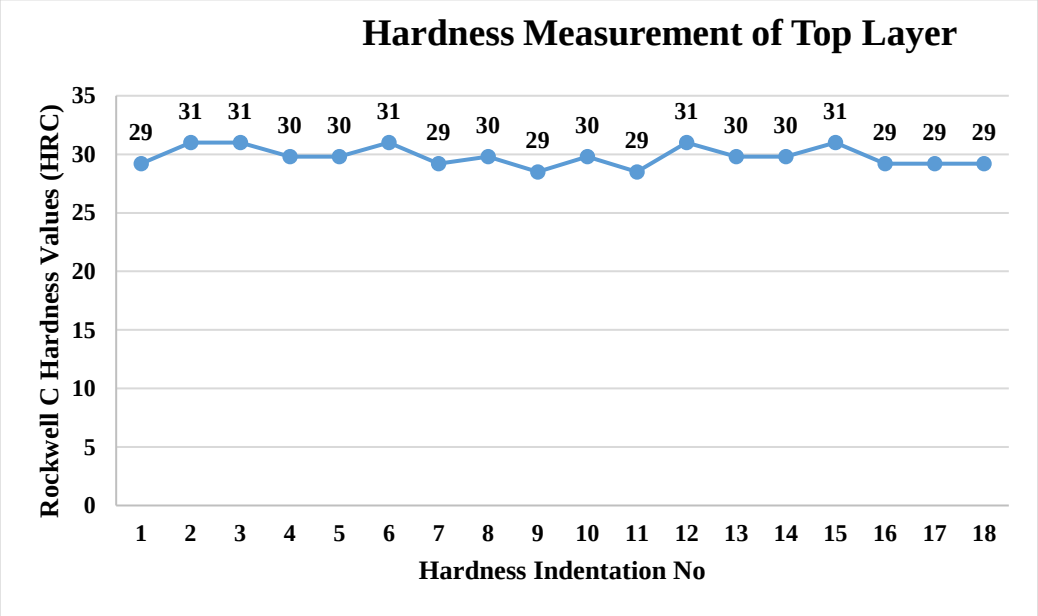

Figure 4-12 Hardness value changes on top layer of 17-4 PH stainless steel specimen

4.2.1.2 Tensile Test Results

The aim of the tensile testing was investigation and comparison of mechanical properties. The mechanical property comparisons were performed with the densest specimen, 30-M LPBF-17-4 PH stainless steel, 30µm thickness layer and meander scanning strategy as specified in section 4.3.

Comparison of the 30µm thickness layer and meander scanning strategy process parameters mechanical data with residual stress optimized process parameters was

performed. 30-M LPBF-17-4 PH stainless steel, 30µm thickness layer and meander scanning strategy, process parameters are specified in Table 3.1. Residual stress optimization Design of Experiment (DOE) details and residual stress optimized process parameters are shared in sections 4.6.1.10 & 4.6.1.11.

The tensile test graphs of conventionally produced 30µm thickness layer with meander scanning strategy process parameters (30-M Conventional) and residual stress optimized process parameters (DOE-I Optimized & DOE-II Optimized) are shown in Figure 4-13 & Figure 4-14 and the tensile test results are given in Table 4-3.

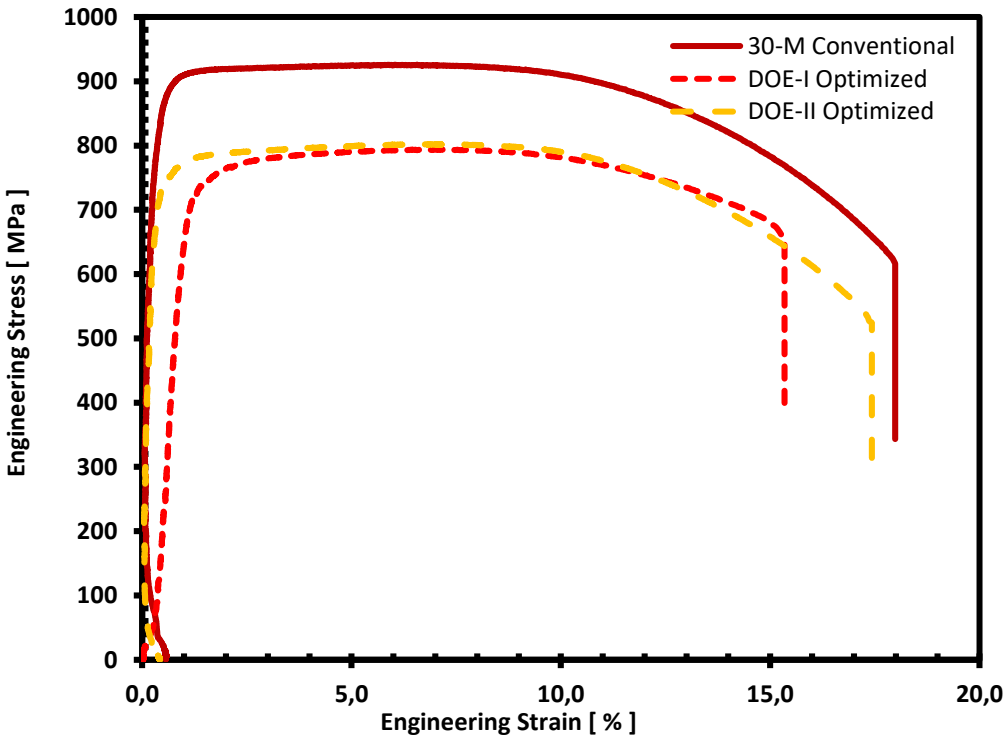

Figure 4-13 Tensile test graphs of conventionally produced 30µm thickness layer with meander scanning strategy process parameters (30-M Conventional) and residual stress optimized process parameters

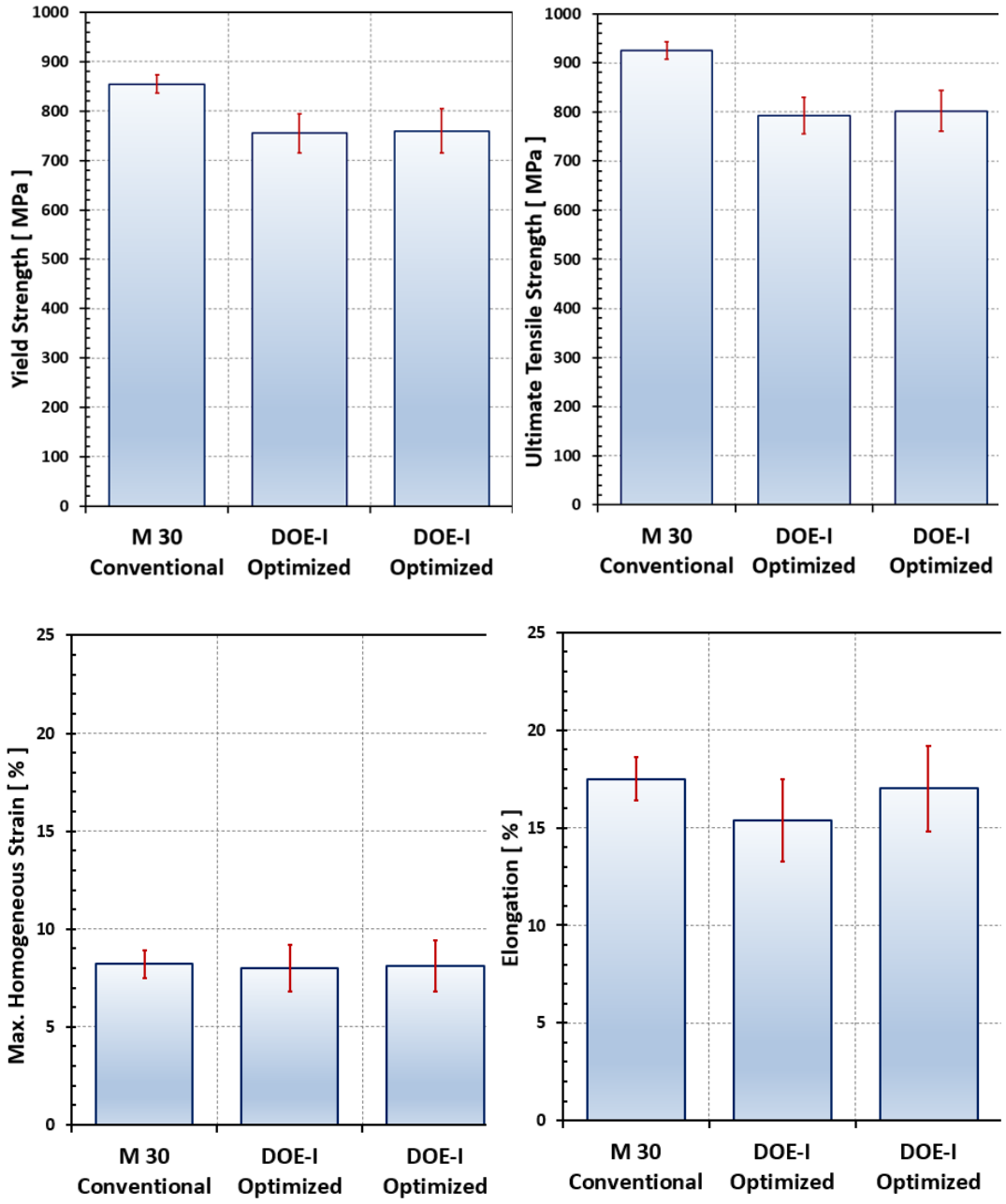

Figure 4-14 Tensile test bar graphs of conventionally produced 30µm thickness layer with meander scanning strategy process parameters (30-M Conventional) and residual stress optimized process parameters

Table 4-3 The tensile test results of conventionally produced 30μm thickness layer with meander scanning strategy process parameters (30-M Conventional) and residual stress optimized process parameters

Material	%0.2 Yield Strength	Ultimate Tensile Strength	Homogenous Strain % (Maximum)	% Elongation (Maximum)
M-30 Conventional	855	925	8,2	17,5
DOE-I Optimized	755	793	7,9	15,4
DOE-I Optimized	760	802	8,1	17,0

The average yield strength, tensile strength, maximum homogenous strain % and maximum elongation % values obtained for 17-4 PH, 30-M specimens were 855 MPa, 925 MPa, 8.2 % and 17,5 % respectively. The obtained values are within the range of ASTM A564 H1100 & H1150 heat-treated condition of conventionally produced 17-4 PH bar specimens as given in Table 2-1. Mechanical properties and residual stress results are evaluated in detail in sections 4.6.1.10 & 4.6.1.11.

4.3 Density Measurement Results and Discussion

17-4 PH stainless steel density values are expected to be 7.8 g/cm^3 at Room Temperature (RT) conditions in accordance with ASM Metals Handbook Volume 1 material data [36]. The control specimen mentioned in section 3.4.1, H900 heat treated, bar formed in 1.5cm Ø, 17-4 PH stainless steel specimen compatible with ASTM A564 standard average density value was measured as 7.73 g/cm^3 at 23 °C.

Additive manufacturing specimens' average density values are given in Table 4-4. The additive manufacturing specimens for 30-M, 30-S, 60-M and 60-S scanning strategies density values are slightly lower than the material reference data of ASM Metals Handbook Volume 1 as expected since some porosities were observed, as

stated in section 4.1.1. The 30-M scanning strategy provided the highest densification than other strategies with a 99.55% relative densification value.

Table 4-4 Average density measurement results of AM specimens

16mm x 16mm x 10 mm Specimens		
Scanning Strategy	**Density (g/cm^3)**	**Relative Density**
30-M	7.695	99.55%
30-S	7.654	99.02%
60-M	7.676	99.30%
60-S	7.644	98.89%

LPBF Process parameters play a key role in the densification of a material. Generally, low volumetric energy density (VED) could not melt the powder layer completely and causes the insufficient connection between the layers and porosity formation. On the other hand, higher VED completely melts the powder layer but causes high thermal stresses which leads to high-temperature gradients and surface stresses. Higher stresses usually deteriorate the structure by trying to get a more stable state. Moreover, high VED could evaporate some elements and cause the formation of entrapped cavities inside the melt pool [27]. Therefore, very high and low VED results with higher porosity and less densification. Using optimum process parameters are required for almost fully dense structure where 30µm Meander Scanning Strategy (30-M) has almost full densification.

4.4 Modulus of Elasticity & Poisson's Ratio Determination by Ultrasonic Flaw Detector

Modulus of Elasticity (E) and Poisson's Ratio (v) of additive manufacturing specimens were calculated by *Equation 7*, *Equation 8* and *Equation 9*. The calculated Modulus of Elasticity and Poisson's Ratio values are given in Table 4-5.

Table 4-5 Modulus of Elasticity (E) and Poisson's Ratio (v) of Additive Manufacturing Specimens

16mm x 16mm x 10 mm Specimens			
Scanning Strategy	**Density(g/cm^3)**	**E (GPa)**	v
30-M	7.695	190	0.30
30-S	7.654	192	0.29
60-M	7.676	181	0.27

The calculated values of modulus of elasticity (E) and poisson's ratio (v) for 30-M and 30-S scanning strategies are given in Table 4-5. The values for 30-M and 30-S are close to Metallic Materials Properties Development and Standardization (MMPDS), 17- PH steel forging material data which is stated in Section 3.2.2. Poisson's ratio (v) and modulus of elasticity (E) values were 0,27 and 197 GPa respectively in accordance with MMPDS material data. The basic difference between forged and additive manufacturing material data in terms of modulus of elasticity and poisson's ratio is due to the production nature difference of additive manufacturing which is explained in section 2.1.1.1. There were also some uncertainties due to measurement by caliper and flaw detector. Caliper and flaw detector were controlled by hand although the measurement needed to be performed very sensitively. Modulus of elasticity calculated values were 96% and 97% of MMPDS 17-4 PH material data for 30-M and 30-S scanning strategies respectively.

Additive manufactured specimens have more porous structure than forged materials which can also be seen by metallography examination in section 4.1.1. The density values of all scanning strategies given in Table 4-4 are lower than the forged or rolled materials as expected and the reasons are explained in detail in section 4.3. 60-S specimen modules of elasticity measurement could not be performed due to the high level of noise detected by ultrasonic measurement and there were cracks on the 60-S specimen, as shown in Figure 4-15.

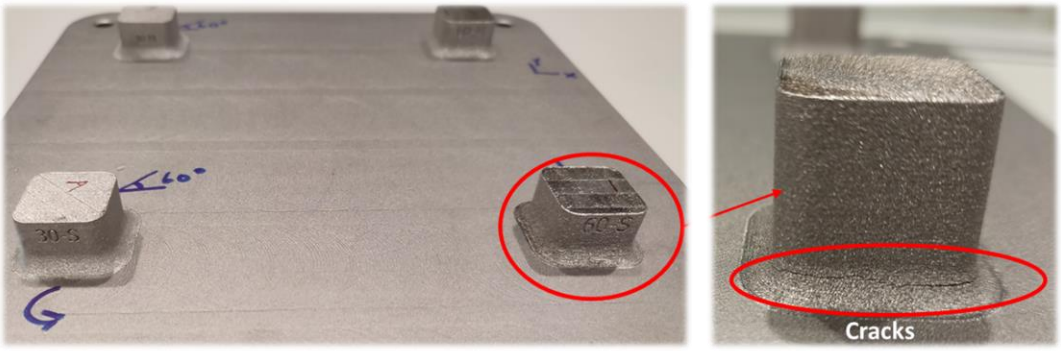

Figure 4-15 Cracks on 60-S scanning strategy specimen

4.5 Simulation Evaluations

Simulations were performed with Simufact Additive Simulation software. Cantilever calibration was performed with the optimum and most dense process parameters of 30µm layer thickness, meander scanning strategy. The calibration data and how it was obtained is given in Section 3.6. The effect & trend of area and height were investigated by Simufact Additive simulation. Simulation results could not be directly compared since the meshes were 500µm in thickness. However, simulation data provides a trend of residual stress changes from the top layer to the mid-center of a material. The results were compared with the experimental results, and the same trend was observed. Simulation specimen deployments are shown in Figure 4-16. Here, specimen numbers 1, 2 & 3 were analyzed for the effect of area expansion and 1, 4, 5 & 6 were analyzed for the impact of height changes. Simulation specimen dimensions are given in Table 4-6. Simulation results provided an idea about residual stresses accumulated on a material and how they change through the center of LPBF specimens.

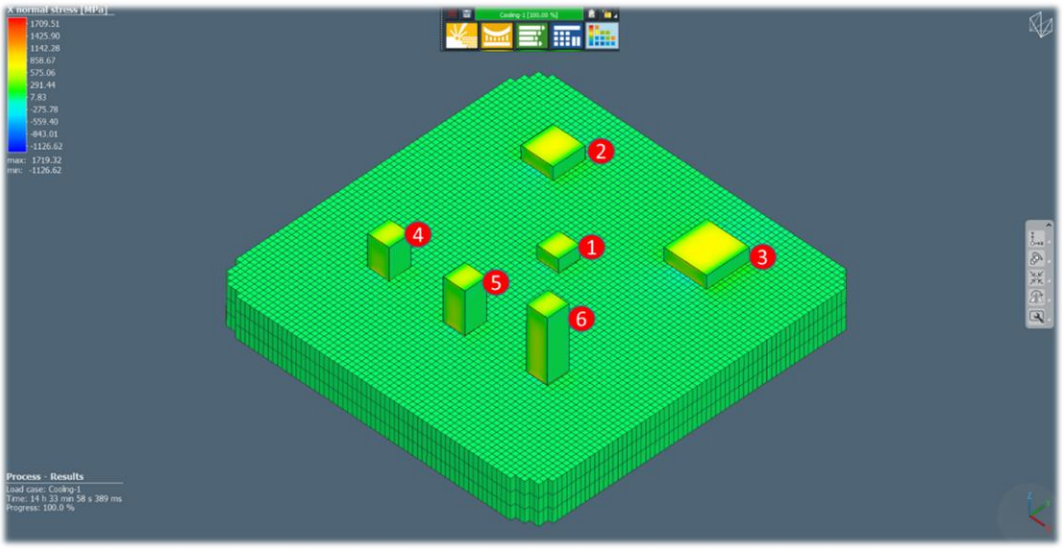

Figure 4-16 Simulation specimen deployment

Table 4-6 Simulation specimen dimensions

Effect of Area Expansion	
Specimen Number 1	16mmx16mmx10mm (X-Y-Z directions)
Specimen Number 2	24mmx24mmx10mm (X-Y-Z directions)
Specimen Number 3	32mmx32mmx10mm (X-Y-Z directions)
Effect of Height Expansion	
Specimen Number 1	16mmx16mmx10mm (X-Y-Z directions)
Specimen Number 4	16mmx16mmx24mm (X-Y-Z directions)
Specimen Number 5	16mmx16mmx32mm (X-Y-Z directions)
Specimen Number 6	16mmx16mmx48mm (X-Y-Z directions)

X normal stresses of Specimen Number 1, 2, 3, 4, 5 & 6 are given in Figure 4-17. In order to see the stress changes, X Normal stresses with 500MPa stress limitation are also given in Figure 4-18.

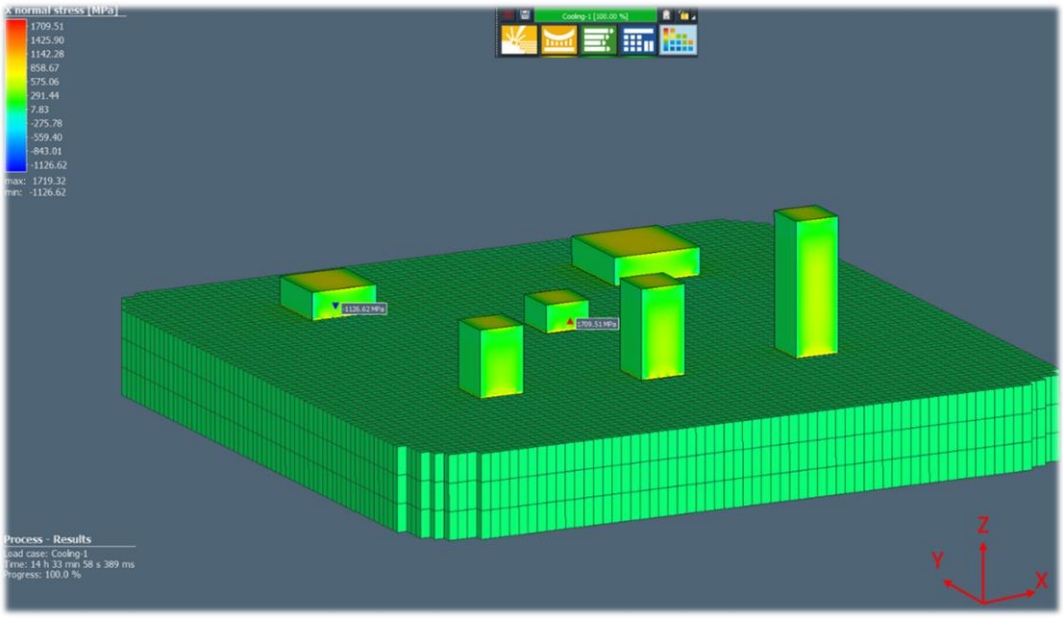

Figure 4-17 X Normal stresses analysis

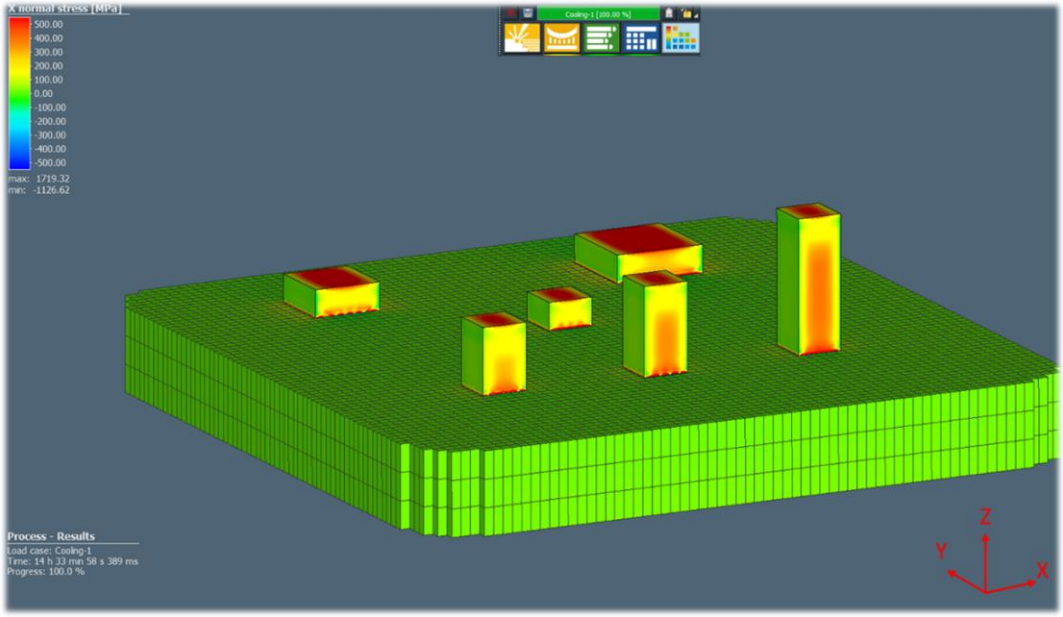

Figure 4-18 X Normal stresses with 500MPa stress limitation demonstration

Y normal stresses of Specimen Number 1, 2, 3, 4, 5 & 6 are given in Figure 4-19. In order to see the stress changes, Y Normal stresses with 500MPa stress limitation are also shown in Figure 4-20.

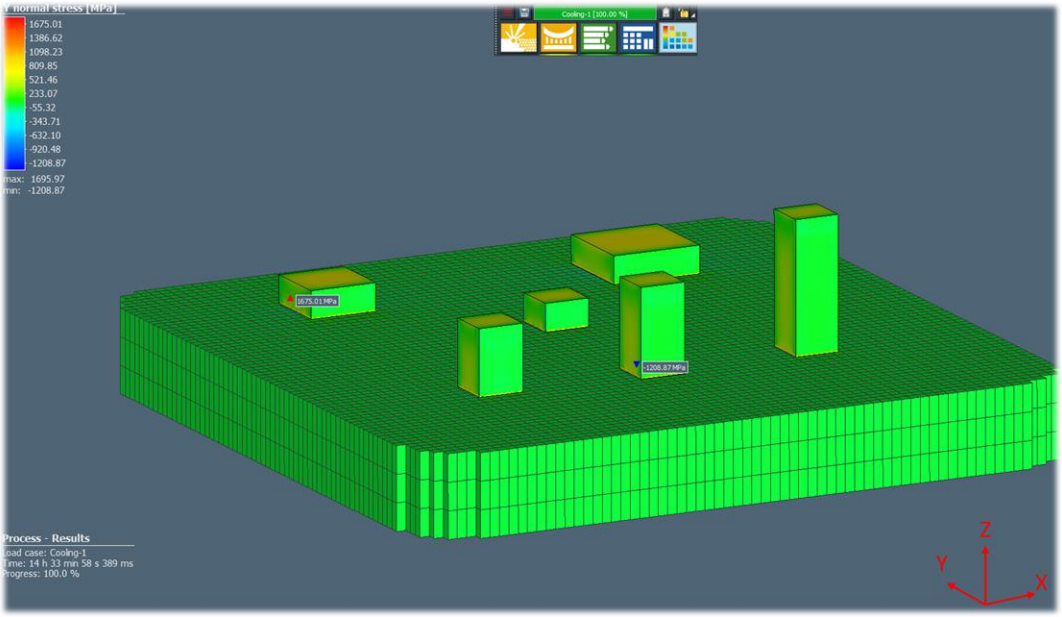

Figure 4-19 Y Normal stresses analysis

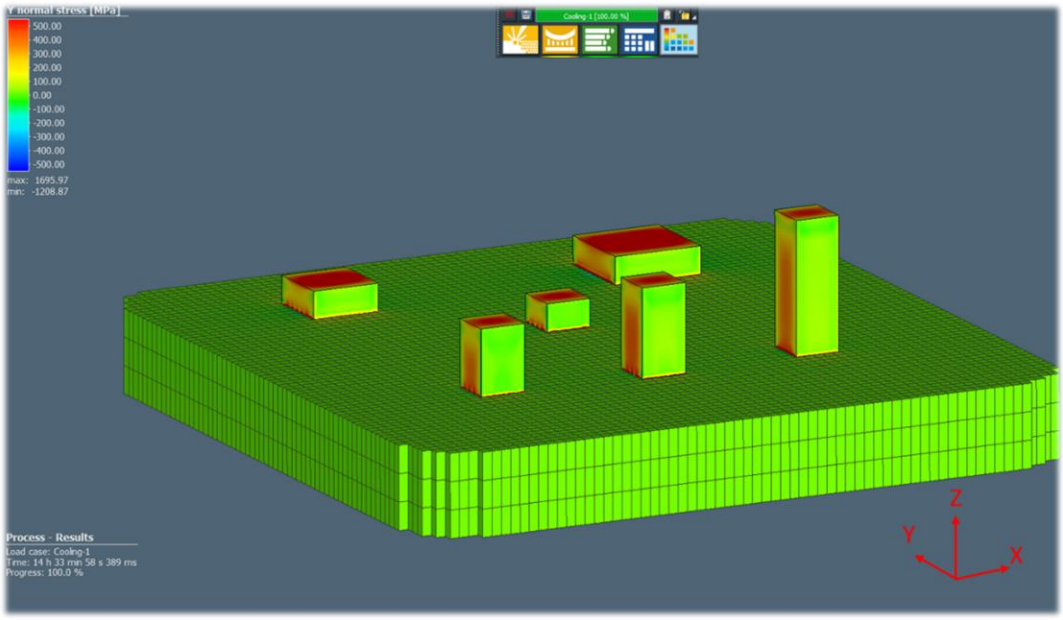

Figure 4-20 Y Normal stresses with 500MPa stress limitation demonstration

Z normal stresses of Specimen Number 1, 2, 3, 4, 5 & 6 are given in Figure 4-21. In order to see the stress changes, Y Normal stresses with 500MPa stress limitation are also given in Figure 4-22.

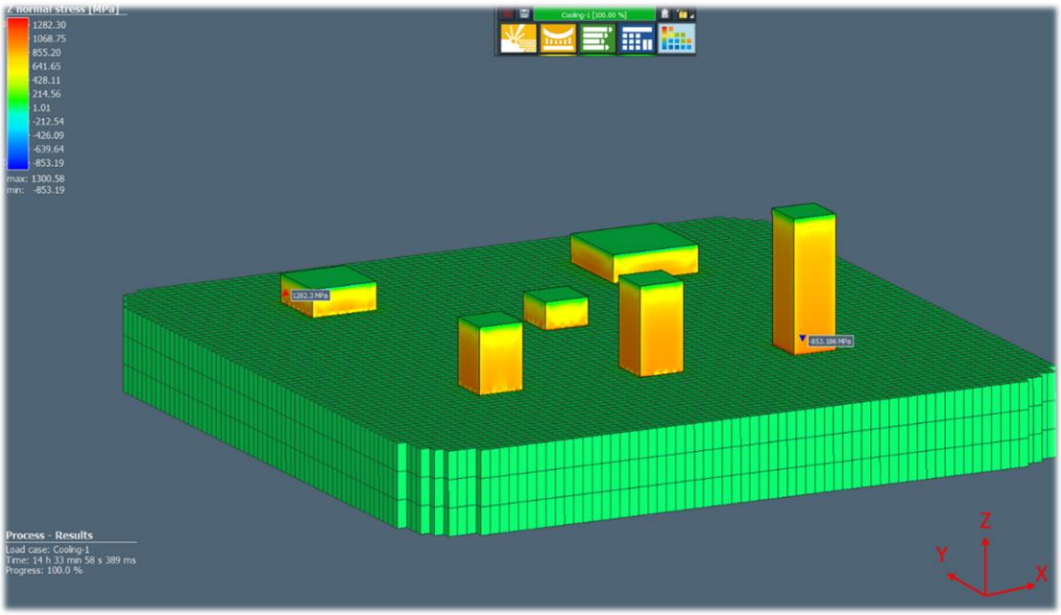

Figure 4-21 Z Normal stresses analysis

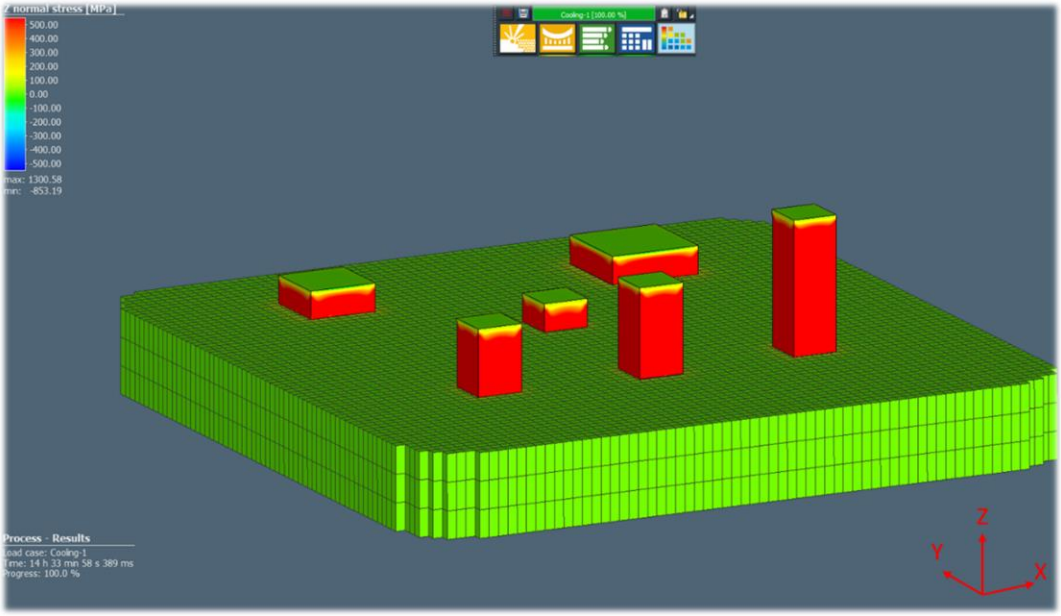

Figure 4-22 Z Normal stresses with 500MPa stress limitation demonstration

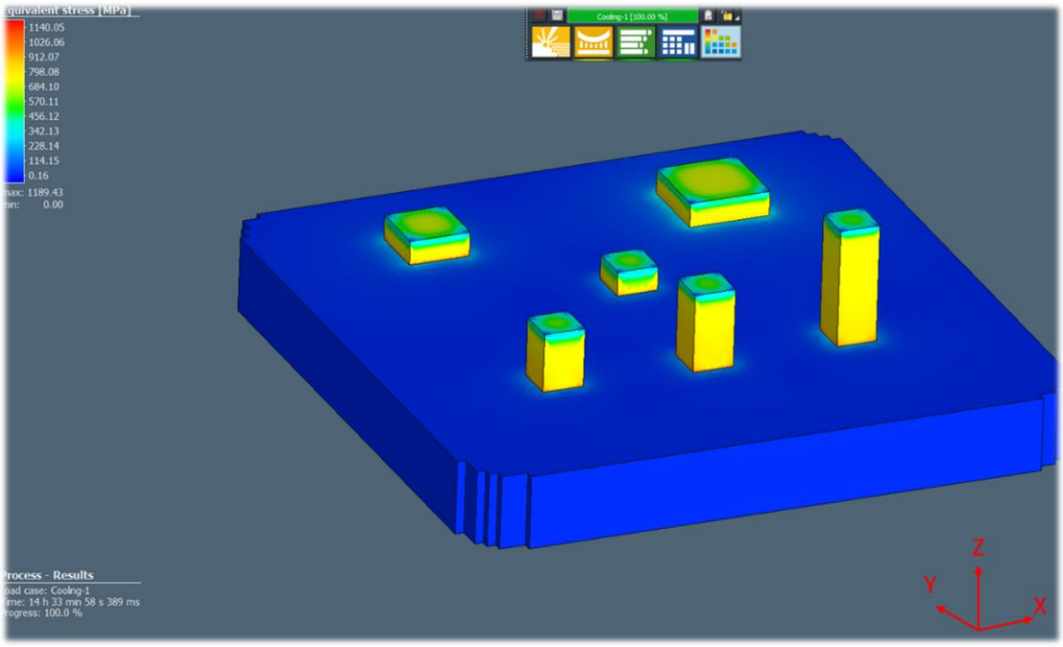

Figure 4-23 Equivalent stresses analysis

Equivalent stresses of the specimens given in Table 4-6 are shown by Figure 4-23.

Cross section was taken from the center of Specimen Number 1. Stress measurement analysis was performed by starting from the top layer through the mid-center of material from each node. The distance between each node was 500µm which was limited by the mesh size.

X normal stresses of Specimen Number 1 were tension stresses at the top layer. Tensile stress level was slightly decreased through the mid-center of the material and then compression stresses were formed as given in Figure 4-24. Tensile stresses were balanced with compression stresses close to the middle of the material. Y normal stresses were analyzed and similar results were obtained with X normal stresses as expected as shown in Figure 4-25. Z normal stresses were almost zero at the top layer as expected since it has the open layer surface in Z direction. Z normal compression stresses were gradually increasing through the mid-center of the specimen number 1 as given in Figure 4-26. Equivalent stresses were analyzed from the mid-cross

section of the material. The tensile stresses were decreasing through the mid-center of the Specimen Number 1 as given in Figure 4-27.

It is important to note that the simulations were performed in accordance with the continuous mode additive manufacturing system. Pulse mode simulation software is needed to enable point distance effect on residual stresses. Pulse mode analysis takes longer times compared to continuous analysis due to too much data consideration. However, it is necessary to consider pulse mode effects. This study might contribute to the development of pulse mode additive manufacturing simulations.

In general simulation and experimental results show similarities. The simulation was carried out with some assumptions, such as the elimination of the rotation of each layer. XRD provided residual stress measurements in each layer by 30μm thickness. On the other hand, the simulation provided 500μm layer measurement and relatively bigger meshes could be applied due to computer capability. Moreover, XRD provided higher resolution of residual stress measurement and more accurate data by including other production factors such as rotation effect compared to simulation analysis. Simulation software required calibration data obtained by cantilever specimens for each process parameter which takes some time. It can be concluded that the experimental XRD residual stress measurement method is a more accurate and sensitive way of providing detailed residual stress measurement. However, simulation software and computer technology are also developing very fast. The XRD results and residual stress measurement perspective of this thesis might contribute to the development of simulation software technology. Although the present simulation software cannot simulate all pulse mode system properties, the simulation software can be accepted as adequate for predicting the structural characteristics.

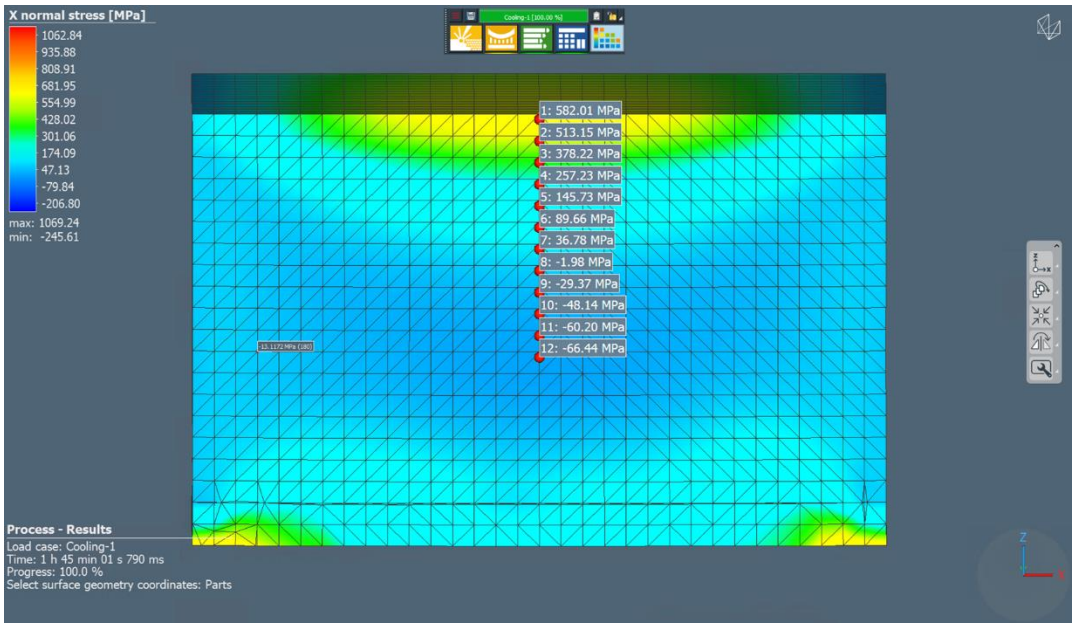

Figure 4-24 X Normal stresses from cross section of a specimen number 1 sample

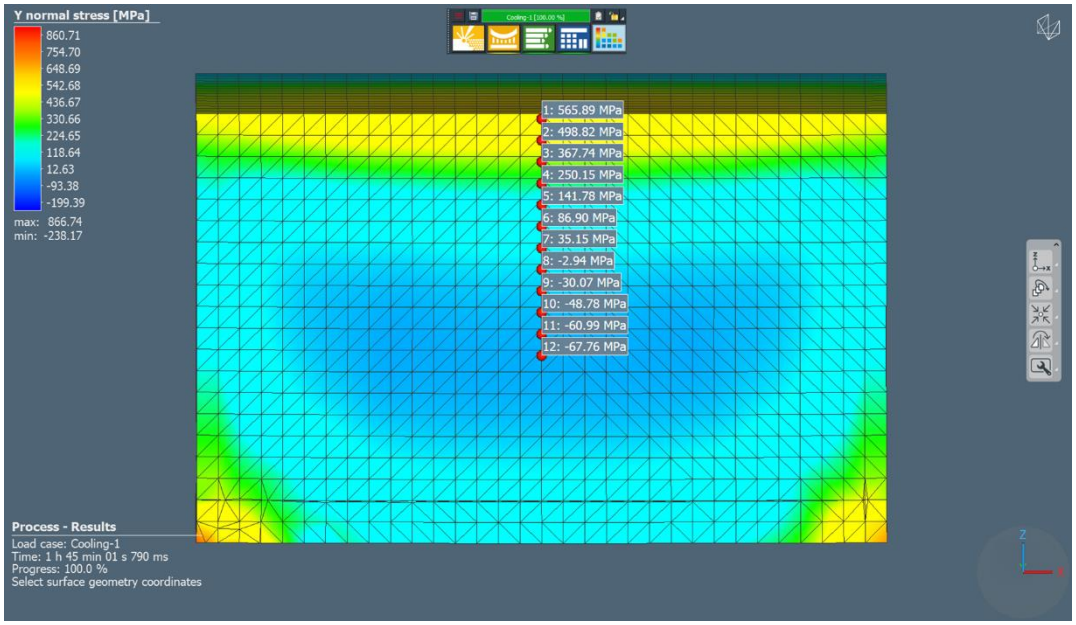

Figure 4-25 Y Normal stresses from cross section of a specimen number 1 sample

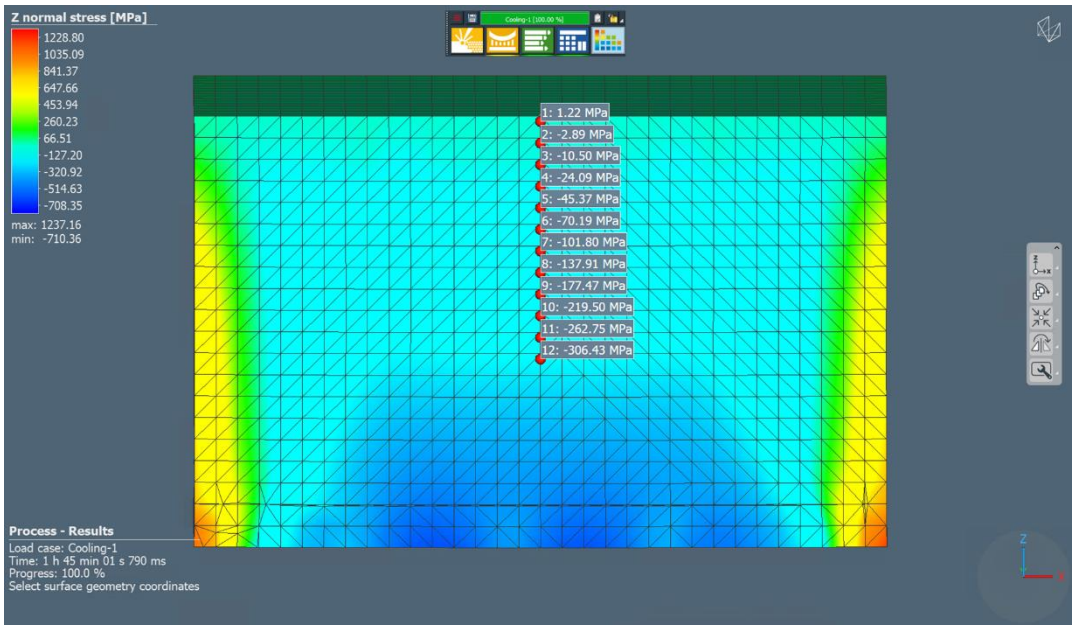

Figure 4-26 Z Normal stresses from cross section of a specimen number 1 sample

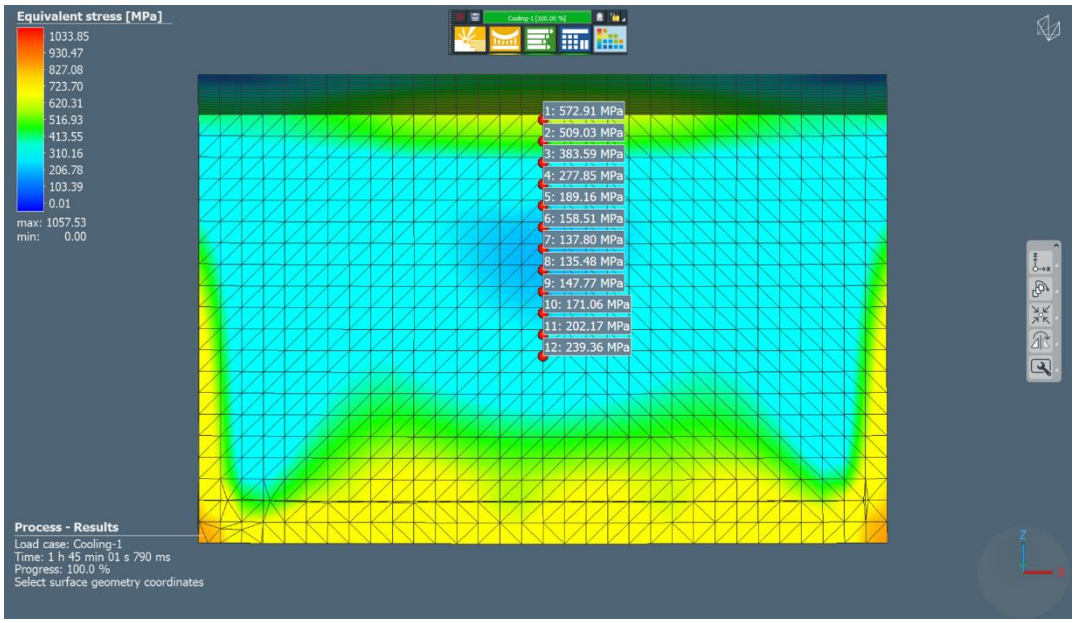

Figure 4-27 Equivalent stresses from cross section of a specimen number 1 sample

4.6 Experimental Residual Stress Measurements by XRD Method

Experimental residual stress measurements were performed to investigate the influence of the process parameters' effect on residual stress of 17-4 PH stainless steel parts manufactured by laser powder bed fusion additive manufacturing system. Within this study, Type I-macroscopic residual stresses were analyzed by XRD residual stress measurement method, where details are given in section 2.3.1. Residual stress values were compared with σ max residual stress results. The investigation and analysis details are given below;

4.6.1 Layer Thickness, Scanning Strategy, Area, Height and Rotation Effect on Residual Stresses

In order to analyze layer thickness, scanning strategy, and rotation effect on residual stresses by the LPBF process, the following specimens were produced;

a. 30µm layer thickness with meander scanning strategy (30-M) and 30° rotation as numbered "specimen#1" in Figure 4-28,
b. 30µm layer thickness with stripe scanning strategy (30-S) and 30° rotation as numbered "specimen#2" in Figure 4-28,
c. 60µm layer thickness with meander scanning strategy and 30° rotation as numbered (60-M) "specimen#3" in Figure 4-28,
d. 60µm layer thickness with stripe scanning strategy (60-S) and 30° rotation as numbered "specimen#4" in Figure 4-28,

as given in Figure 4-28. The angles stated on the specimens were the top layers' final scanning angles. The scanning angles were rotated 30° in Counter Clockwise (CCW) direction for specimens#1, 2, 3 and 4. In order to compare scanning strategies' effect on residual stresses, 30-M and 30-S scanning strategies are compared within each

other. Moreover, layer thickness difference effects on residual stresses were compared by 30-M and 60-M scanning strategies.

The specimens were fluorescent penetrant inspected in accordance by ASTM E-1417 [79]. Cracks were observed by fluorescent penetrant inspection on the 60-S specimen as shown in Figure 3-10 and Figure 4-28. Therefore, the 60-S specimen as marked "specimen#4" in Figure 4-28 had not been taken into consideration for evaluation. Specimen#1, 2, 3 and 4 were built in 16mm x 16mm x 10mm dimensions for the residual stress measurements.

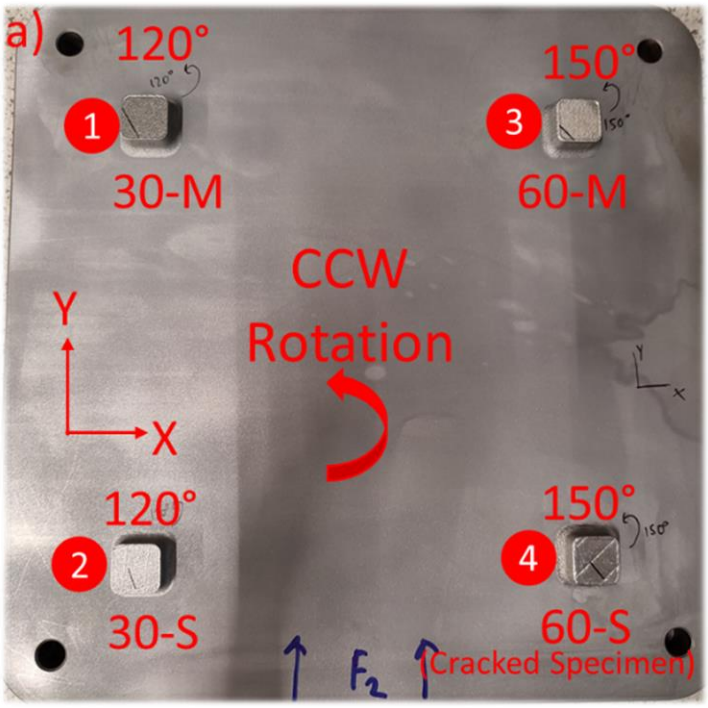

Figure 4-28 30-M (specimen#1), 30-S (specimen#2), 60-M (specimen#3) and 60-S (specimen#4) specimens a) top view

In order to analyze the area, chessboard scanning strategy, area and rotation effect on residual stresses by the LPBF process, the following specimens were produced;

e. 30µm layer thickness with chessboard scanning strategy (30-CB) and 30° rotation as numbered “specimen#5” in Figure 4-29,
f. 30µm layer thickness with chessboard scanning strategy (30-CB) and 67° rotation as numbered “specimen#6” in Figure 4-29,
g. 60µm layer thickness with chessboard scanning strategy (60-CB) and 67° rotation as numbered “specimen#7” in Figure 4-29,
h. 60µm layer thickness with chessboard scanning strategy (60-CB) and 30° rotation as numbered “specimen#8” in Figure 4-29,
i. 30µm layer thickness with meander scanning strategy and 67° rotation as numbered “specimen#9” (30-M 16mmx16mmx10mm) in Figure 4-29,
j. 30µm layer thickness with meander scanning strategy and 67° rotation as numbered “specimen#10” (30-M 24mmx24mmx10mm) in Figure 4-29,
k. 30µm layer thickness with meander scanning strategy and 67° rotation as numbered “specimen#11” (30-M 32mmx32mmx10mm) in Figure 4-29,
l. 30µm layer thickness with meander scanning strategy and 30° rotation as numbered “specimen#12” (30-M R30) in Figure 4-29,
m. 30µm layer thickness with stripe scanning strategy and 30° rotation as numbered “specimen#13” (30-S R30) in Figure 4-29

The specimens were fluorescent penetrant inspected by ASTM E-1417 [78]. Crack was detected by fluorescent penetrant inspection on 60-CB specimens, namely “specimen#7” and “specimen#8”. Therefore, these specimens had not been taken into consideration for evaluation.

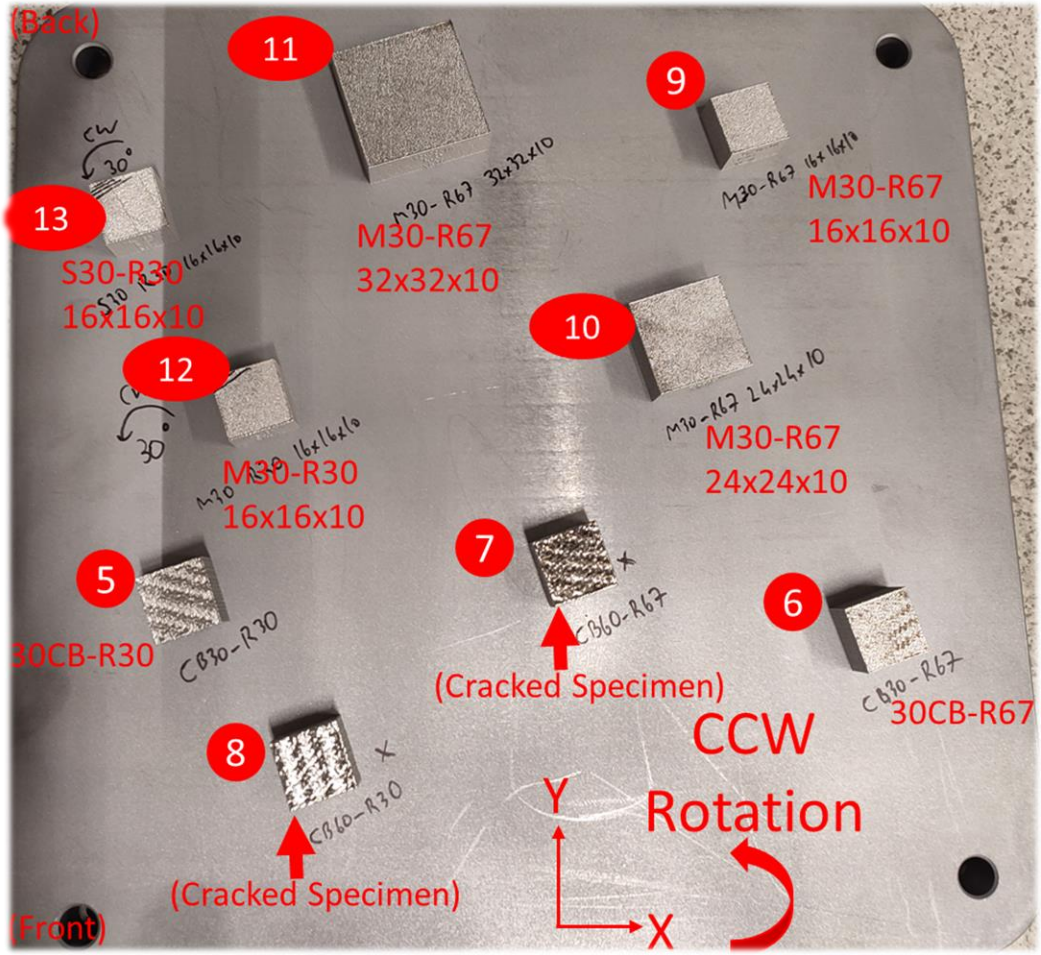

Figure 4-29 30-CB Rotation 30° (specimen#5), 30-CB Rotation 67° (specimen#6), 60-CB Rotation 67° (specimen#7), 60-CB Rotation 30° (specimen#8), 30-M 16mmx16mmx10mm Rotation 67° (specimen#9), 30-M 24mmx24mmx10mm Rotation 67° (specimen#10), 30-M 32mmx32mmx10mm Rotation 67° (specimen#11), 30-M 16mmx16mmx10mm Rotation 30° (specimen#12), 30-S 16mmx16mmx10mm Rotation 30° (specimen#13)

Summary of the residual stress measurement specimen properties for specimens #1 to #13 is given in Table 4-7

Table 4-7 Residual stress measurement specimen properties

No	Specimen	Specimen Notation	Layer Thickness	Scanning Strategy	Rotation	Specimen Dimension [mm] (X-Y-Z Directions)	Fluorescent Penetrant Inspection Result
a.	Specimen#1	30-M	30µm	Meander	30°	16x16x10	Passed
b.	Specimen#2	30-S	30µm	Stripe	30°	16x16x10	Passed
c.	Specimen#3	60-M	60µm	Meander	30°	16x16x10	Passed
d.	Specimen#4	60-S	60µm	Stripe	30°	16x16x10	Crack Detected
e.	Specimen#5	30-CB	30µm	Chessboard	30°	16x16x10	Passed
f.	Specimen#6	30-CB	30µm	Chessboard	67°	16x16x10	Passed
g.	Specimen#7	60-CB	60µm	Chessboard	30°	16x16x10	Crack Detected
h.	Specimen#8	60-CB	60µm	Chessboard	67°	16x16x10	Crack Detected
i.	Specimen#9	30-M	30µm	Meander	67°	16x16x10	Passed
j.	Specimen#10	30-M	30µm	Meander	67°	24x24x10	Passed
k.	Specimen#11	30-M	30µm	Meander	67°	32x32x10	Passed
l.	Specimen#12	30-M	30µm	Meander	30°	16x16x10	Passed
m.	Specimen#13	30-S	30µm	Stripe	30°	16x16x10	Passed

Residual stress results and discussions are given below;

4.6.1.1 30µm Layer Thickness with Meander Scanning Strategy (30-M) "Specimen#1"

30µm layer thickness with meander scanning strategy (30-M) 16mm x 16mm x 10mm specimen as marked "specimen#1" was built as given in Figure 4-28. Residual stress measurement was started from the top layer of the specimen through the bottom of the specimen. Residual stresses on each layer's center were tried to be measured. Therefore, firstly ~15µm first layer was removed, and then ~30µm layers were removed by electro-polish operation. The illustration of the residual stress measurement points is tried to be illustrated in Figure 4-30.

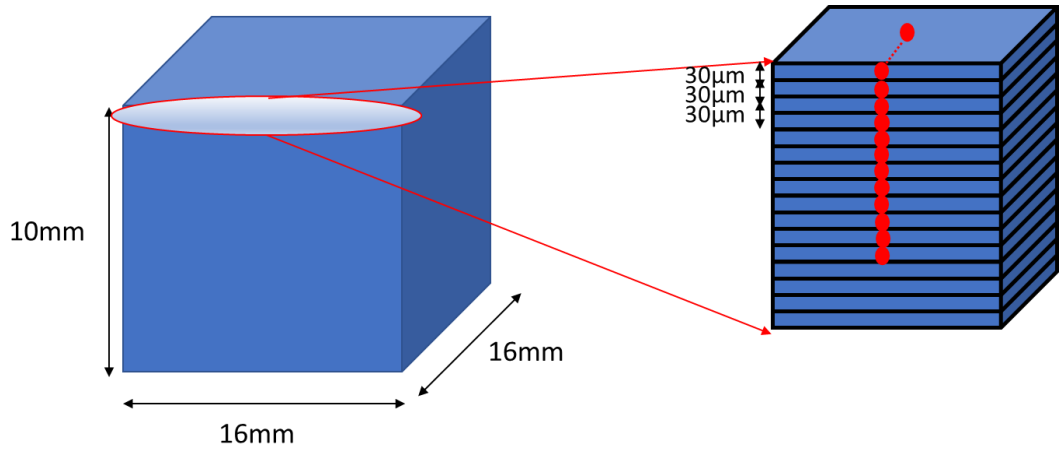

Figure 4-30 Residual stress measurement illustration of 30 M & 30 S specimen

30-M scanning strategy principal stresses measured and measurement depth were given in Table 4-8.

Table 4-8 30-M scanning strategy principal stresses by depth

No of XRD Measurement	Part Name	*Measurement Depth (mm)*	*Scanning Degree°*	*Principal Stresses*		
				σ max (MPa)	*σ min (MPa)*	*φ(σ max)(°)*
1	30-M	0	120	539	216	-75,0 ± 9,4
2	30-M	0,015	120	595	318	-76,3 ± 10,1
3	30-M	0,043	150	573	251	-51,6 ± 5,7
4	30-M	0,077	180	669	435	-70,1 ± 12,3
5	30-M	0,104	210	754	459	-88,0 ± 7,8
6	30-M	0,137	240	655	346	-77,4 ± 8,6
7	30-M	0,167	270	544	385	-69,9 ± 10,6
8	30-M	0,194	300	464	448	49,6 ± 51,2
9	30-M	0,223	330	474	388	73,4 ± 17,4
10	30-M	0,256	360	464	382	-52,8 ± 13,2
11	30-M	0,29	0	467	361	-47,8 ± 9,6
12	30-M	0,316	30	491	337	-46,0 ± 7,5
13	30-M	0,344	60	468	392	21,0 ± 20,0

Residual stress values were compared with σ max residual stress results. Residual stresses first slightly increase starting from the surface and then start decreasing. The surface stresses are relatively lower than the very close sub-surfaces due to open surface area, and residual stresses are then gradually decreased as given in Figure 4-31. Residual change trend was also observed by simulation results as given in Section 4.5. Moreover, by the advantage of very sensitive XRD residual stress measurement capability, surface stresses for each layer could be able to be evaluated.

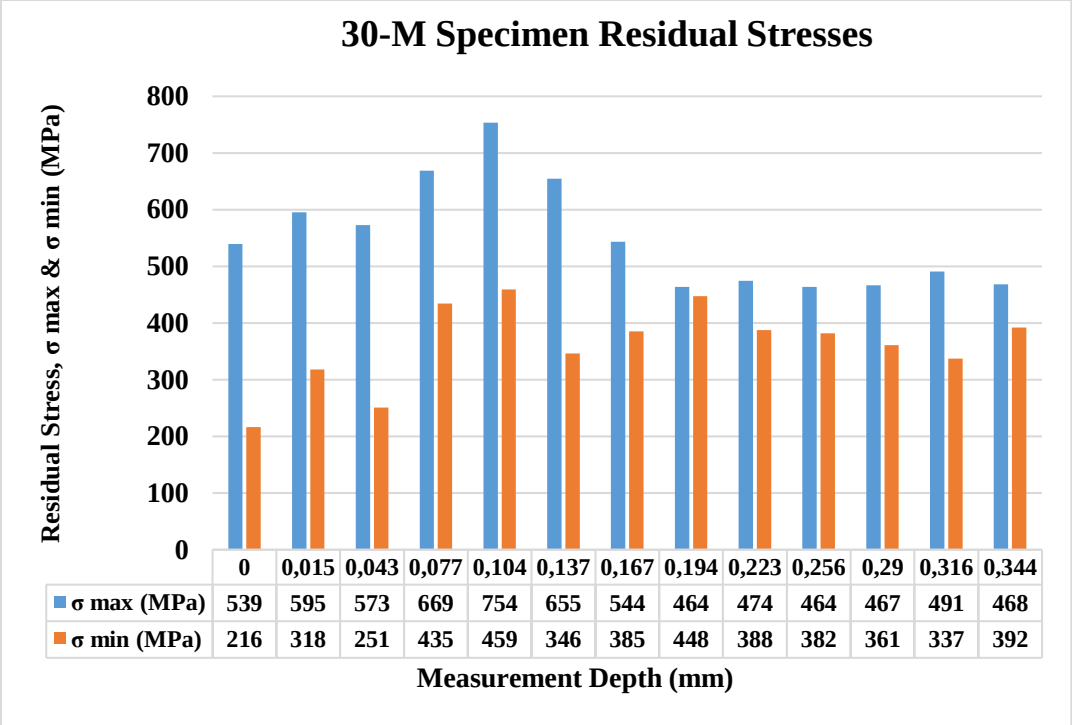

Figure 4-31 30-M specimen residual stresses

Rotation effect of the 30-M scanning strategy is given in Figure 4-32. The angle of the rotation was 30° in counter clockwise (CCW) direction and 30 M scanning was started at 120° as shown in Figure 4-28. Rotation of the scanning strategy might have a minor effect on residual stresses. The effect of it could not be particularly specified due to other dominant residual stress effects such as melting and solidification practices of each layer.

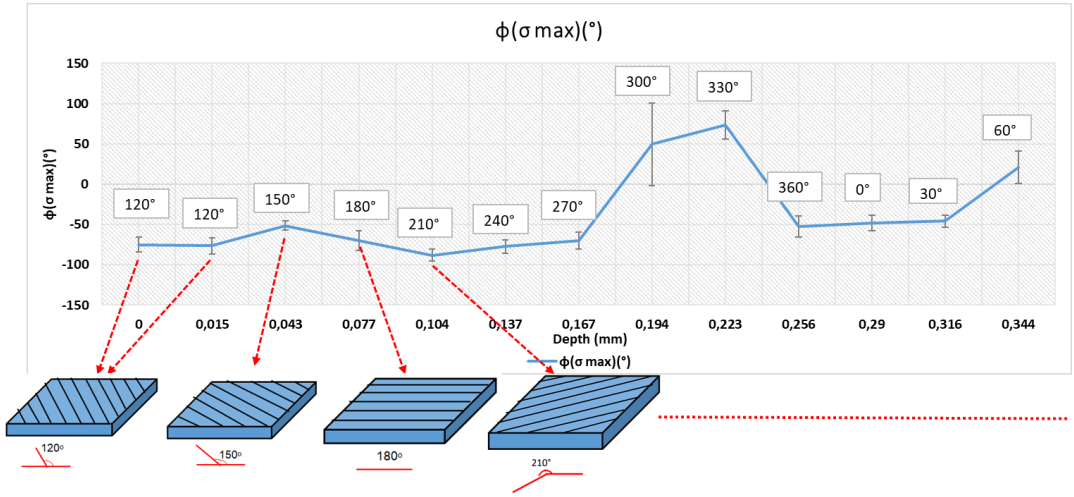

Figure 4-32 Rotation effect of 30-M scanning strategy

Residual stresses by depth for the 30-M scanning strategy graph is given in Figure 4-33.

Stripe scanning strategy has a shorter vectorial scanning length in defined areas as given in Figure 2-13 and Figure 2-14. As mentioned in detail in section 2.3.2.1, the melting and solidification practice of each layer causes the accumulation of residual stresses for the LPBF process. Although the exact process parameters were used for 30-M and 30-S scanning strategies, the 30-S scanning strategy provided relatively fewer surface residual stress values. Therefore, shorter vectorial scanning for the 30-S scanning strategy contributed to less cooling of the specimen and fewer residual stresses accumulated as a result on the 30-S specimen. Moreover, having relatively less density and more porosities also slightly contributed fewer residual stress accumulation by stress relaxation, as explained in Mugwagwa et al.'s study [22].

30-M and 60-M scanning strategies have almost the same surface residual stress values. 60-M process parameters are used for melting 60µm layer thickness, while 30-M process parameters are used for melting 30µm layer thickness. 60-M's %15 more volumetric energy density was used melting of thicker layers, and residual

stress change was not affected much due to this total volumetric energy density difference.

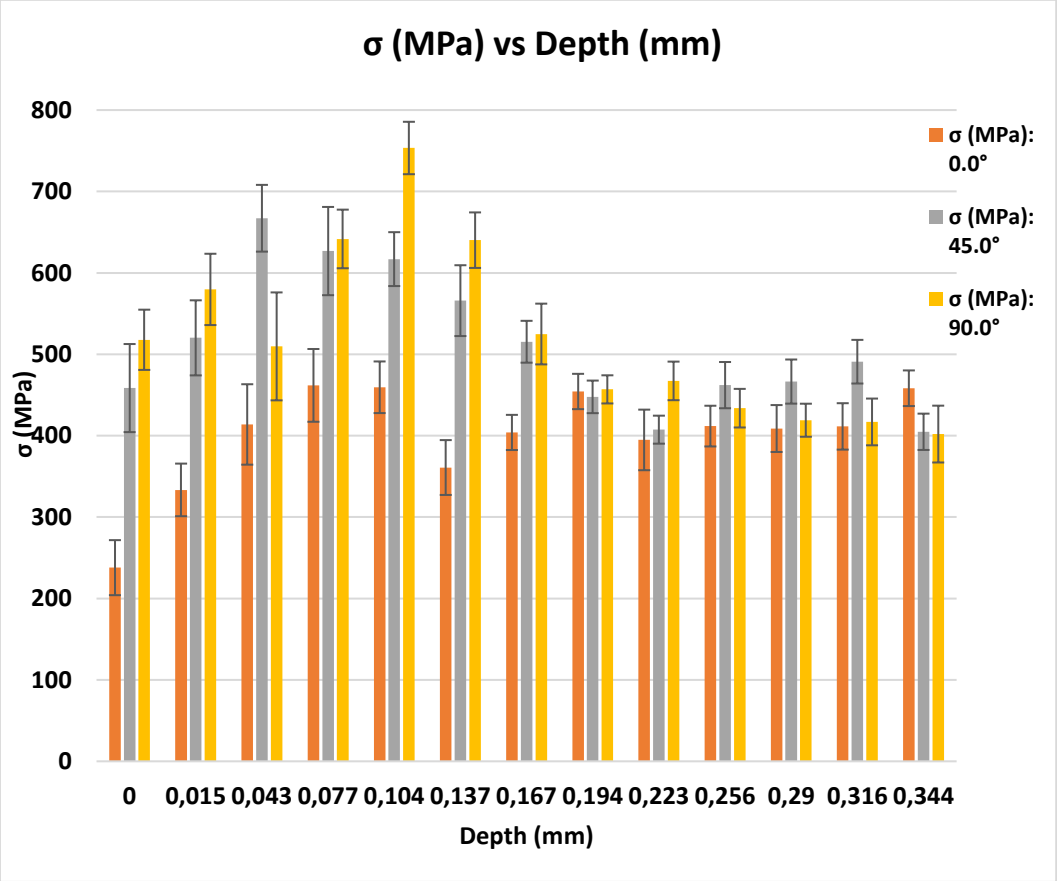

Figure 4-33 Residual stresses by depth for 30-M scanning strategy

4.6.1.2 30µm Layer Thickness with Stripe Scanning Strategy (30-S) "Specimen#2"

30µm layer thickness with stripe scanning strategy (30-S) 16mm x 16mm x 10mm specimen as marked "specimen#2" was built as given in Figure 4-28. Residual stress measurement was started from the top layer of the specimen through the bottom of the specimen. Residual stresses on each layer's center were tried to be measured.

Therefore, firstly ~15µm layer was removed, and then ~30µm layers were removed by electro-polish operation as the same procedure was applied for the meander scanning strategy. The illustration of the residual stress measurement points was tried to be illustrated in Figure 4-30.

30-S scanning strategy principal stresses measured and measurement depth were given in Table 4-9. and the graph is shown in Figure 4-34.

Table 4-9 30-S scanning strategy principal stresses by depth

No of XRD Measurement	Part Name	*Measurement Depth (mm)*	*Scanning Degree°*	*Principal Stresses*		
				σ max (MPa)	*σ min (MPa)*	*φ(σ max)(°)*
1	30-S	0	120	442	263	77,3 ± 16,2
2	30-S	0,016	120	486	335	-70,5 ± 19,2
3	30-S	0,046	150	607	248	-64,8 ± 8,7
4	30-S	0,074	180	588	307	-70,9 ± 12,2
5	30-S	0,105	210	556	358	-83,7 ± 19,1
6	30-S	0,133	240	532	285	-81,2 ± 10,3
7	30-S	0,166	270	537	377	-87,9 ± 17,3
8	30-S	0,194	300	483	302	-71,1 ± 11,6
9	30-S	0,225	330	456	401	29,5 ± 27,6
10	30-S	0,258	360	450	427	44,4 ± 53,5
11	30-S	0,284	0	503	360	57,3 ± 10,0
12	30-S	0,318	30	477	370	47,3 ± 14,3
13	30-S	0,345	60	427	378	-59,1 ± 33,1

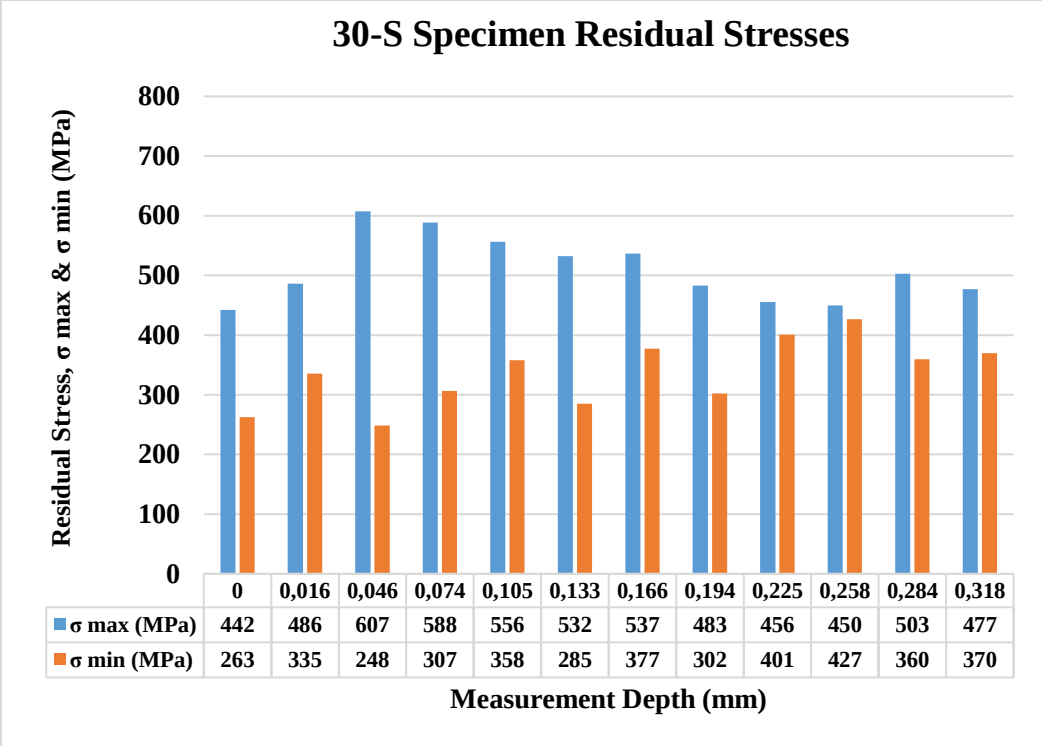

Figure 4-34 30-S specimen residual stress graph

Residual stresses by depth for the 30-S scanning strategy graph is given in Figure 4-35. Residual stress values were compared with σ max residual stress results.

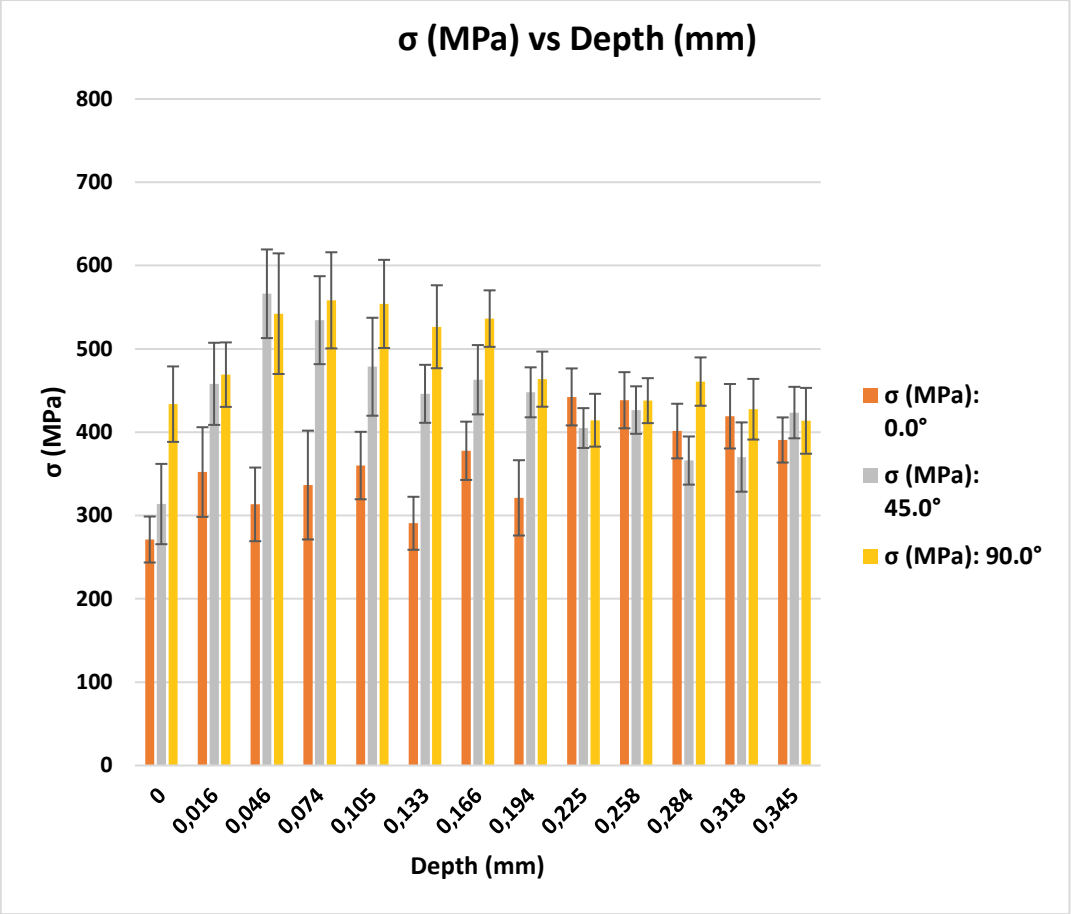

Figure 4-35 Residual stresses by depth for 30-S scanning strategy

4.6.1.3 60µm Layer Thickness with Meander Scanning Strategy (60-M) "Specimen#3"

60µm layer thickness with meander scanning strategy (60-M) 16mm x 16mm x 10mm specimen as marked "specimen#3" was built as given in Figure 4-28. Residual stress measurement was started from the top layer of the specimen through the bottom of the specimen. Residual stresses on each layer's center were tried to be measured. Therefore, firstly ~30µm one layer and then ~60µm layers were removed

by electro polish operation. The illustration of the residual stress measurement points is tried to be illustrated in Figure 4-36.

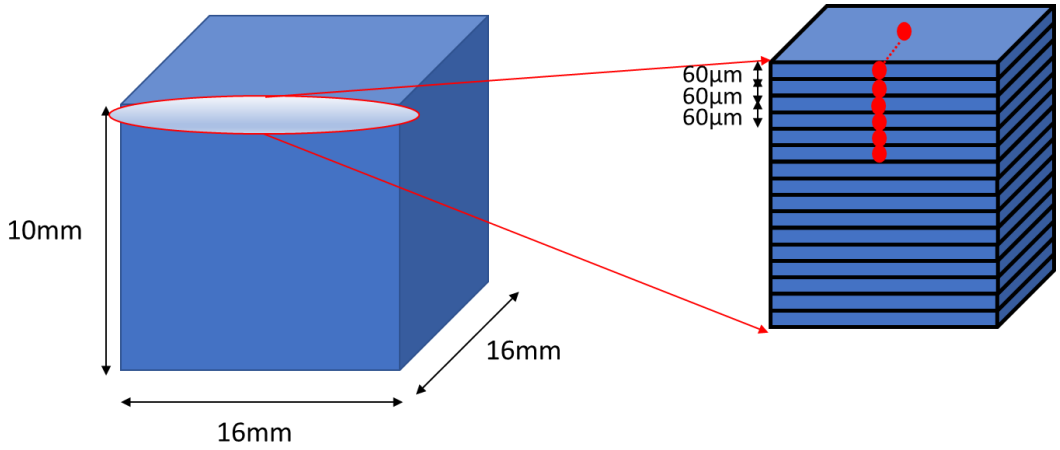

Figure 4-36 Residual stress measurement illustration of 60 M specimen

60-M scanning strategy principal stresses measured and measurement depth were given in Table 4-10 and the graph is given in Figure 4-37.

Table 4-10 60-M scanning strategy principal stresses by depth

No of XRD Measurement	Part Name	*Measurement Depth (mm)*	*Scanning Degree°*	*Principal Stresses*		
				σ max (MPa)	*σ min (MPa)*	*φ(σ max)(°)*
1	60-M	0,000	150	558	457	-12,8 ± 52,6
2	60-M	0,037	150	510	457	-6,5 ± 128,3
3	60-M	0,090	180	720	177	-31,1 ± 8,5
4	60-M	0,154	210	642	455	-80,0 ± 28,2
5	60-M	0,210	240	613	163	-39,4 ± 6,6
6	60-M	0,268	270	527	262	-46,6 ± 9,4
7	60-M	0,330	300	551	351	-47,1 ± 11,8

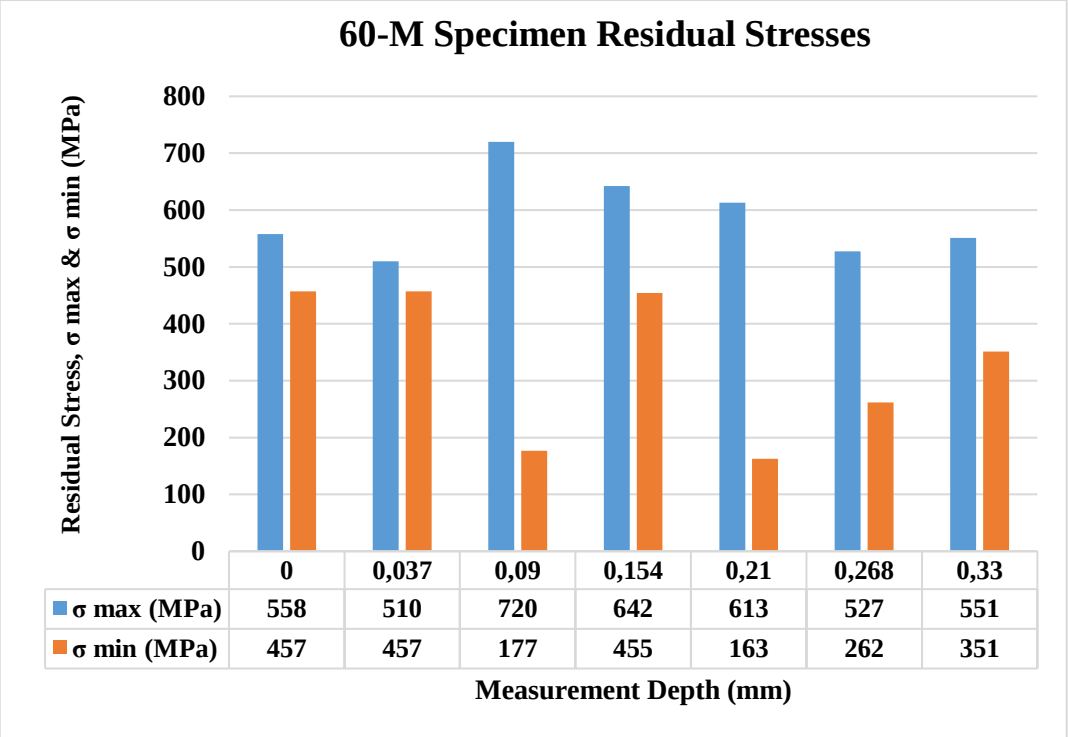

Figure 4-37 60-M specimen residual stress graph

Residual stresses by depth for the 60-M scanning strategy graph is given in Figure 4-38. Residual stress values were compared with σ max residual stress results.

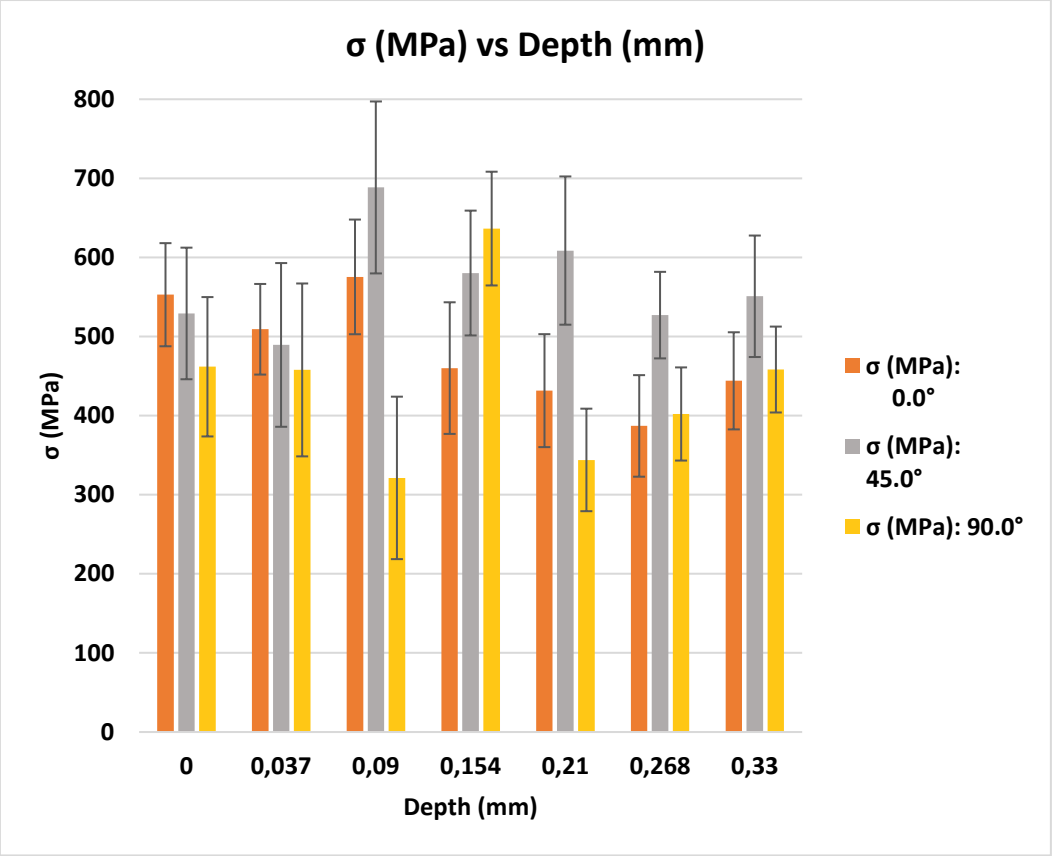

Figure 4-38 Residual stresses by depth for 60-M scanning strategy

30-S residual stress values are slightly lower than the 30-M and 60-M parameters. This might be due to higher porosity content which could lead to slight stress relief by having more open surfaces. Mugwagwa et al. also observed similar effects which support the studies as stated in section 2.3.2.1 [22].

4.6.1.4 30µm Layer Thickness with Chessboard Scanning Strategy (30-CB) "Specimen#5"

30µm layer thickness with chessboard scanning strategy (30-CB) 16mm x 16mm x 10mm specimen as marked "specimen#5" was built as given in Figure 4-29. A closed

view of chessboard scanning strategy (30-CB) is given in Figure 4-39. Small scanning islands can be clearly seen on the specimen.

Figure 4-39 Closed view of chessboard scanning strategy (30-CB)

30-CB scanning strategy principal stresses measured and measurement depth were given in Table 4-11, and the graph is shown in Figure 4-40.

Table 4-11 30-CB scanning strategy principal stresses by depth

No of XRD Measurement	Part Name	*Measurement Depth (mm)*	*Principal Stresses*		
			σ max (MPa)	*σ min (MPa)*	*φ(σ max)(°)*
1	30-CB	0	643	395	40 ± 6,1
2	30-CB	0,014	633	486	40,3 ± 13,6
3	30-CB	0,106	574	327	38,6 ± 7,7

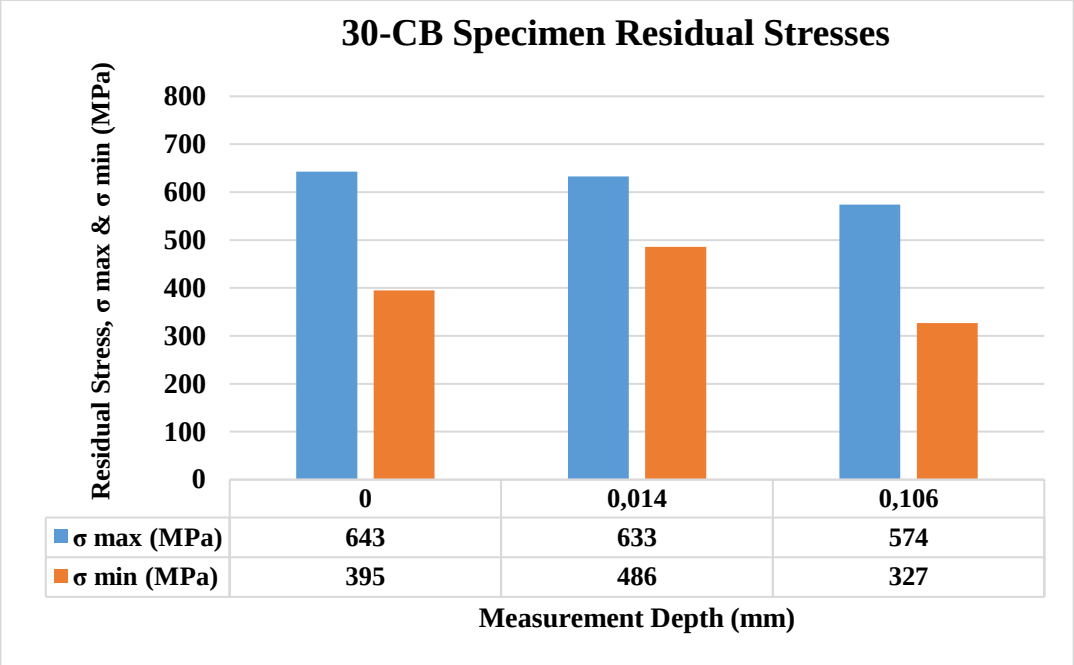

Figure 4-40 30-CB specimen residual stress graph

Residual stresses by depth for the 30-CB scanning strategy graph is given in Figure 4-41. Residual stress values were compared with σ max residual stress results. In order to understand the residual stress formation by 30-CB, residual stresses were measured for the selected depths as stated in Table 4-11. Generally, chessboard strategy is not much preferred in the industry due to leakage issues as mentioned in section 2.1.1.1.

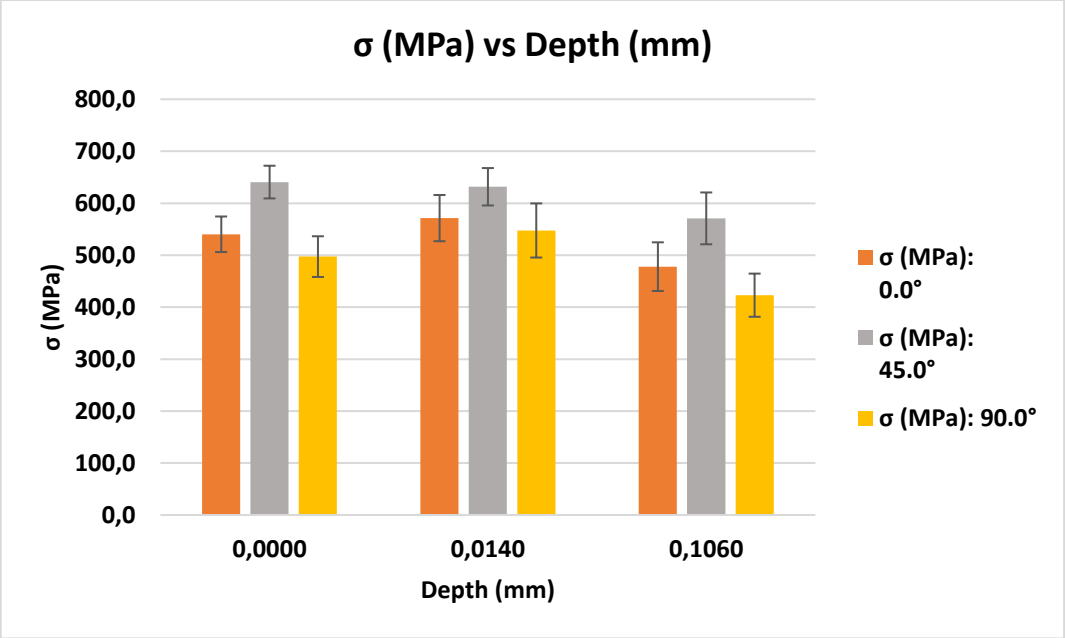

Figure 4-41 Residual stresses by depth for 30-CB scanning strategy

4.6.1.5 Effect of Area Examination

Effect of area examination was performed with comparison of specimen#9, specimen#10 and specimen#11, as given in Figure 4-29 and specimen properties are specified in Table 4-7.

The effect of area examination residual stress results is given in Table 4-12.

Table 4-12 Effect of area examination residual stress results

No of XRD Measurement	Part Name	Specimen Dimension [mm] (X-Y-Z Directions)	*Measurement Depth (mm)*	*Principal Stresses*		
				σ max (MPa)	*σ min (MPa)*	*φ (σ max)(°)*
1	Specimen#9	16x16x10	0,0000	540	276	4,8 ± 4,9
2	Specimen#9	16x16x10	0,0150	531	402	11,4 ± 9,3
3	Specimen#9	16x16x10	0,1350	574	381	4,2 ± 8
4	Specimen#10	24x24x10	0,0000	571	256	21,8 ± 5,4
5	Specimen#10	24x24x10	0,0170	639	340	24,7 ± 4,9
6	Specimen#10	24x24x10	0,1100	648	337	15,2 ± 4,6
7	Specimen#11	32x32x10	0,0000	581	221	22,3 ± 3,7
8	Specimen#11	32x32x10	0,0170	672	296	13,9 ± 5,5
9	Specimen#11	32x32x10	0,1060	695	403	14,5 ± 5

Surface stress comparison of residual stress area specimens is given in Figure 4-42. Similar XRD residual stress trend was observed for σ max residual stresses with simulation analysis.

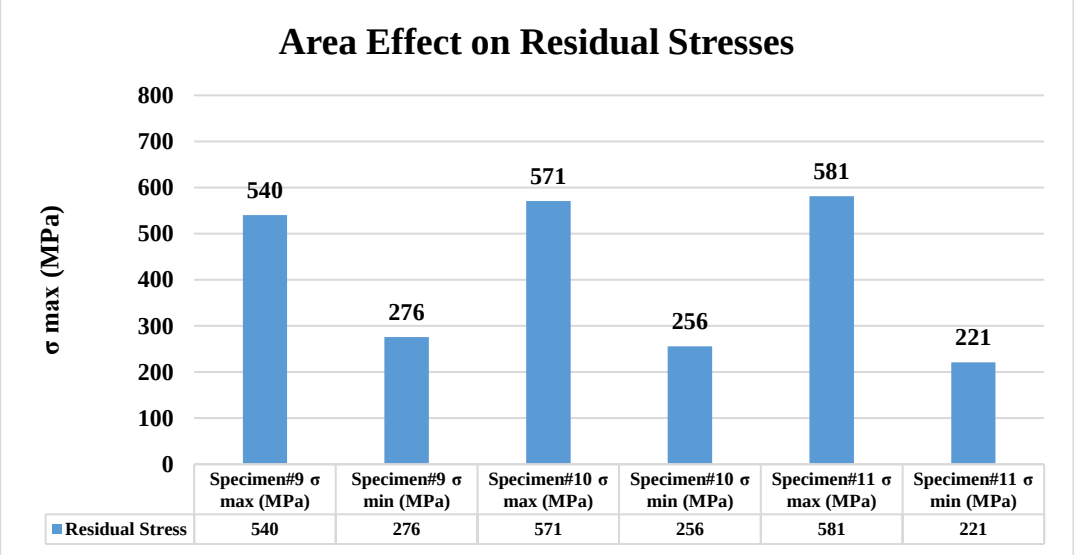

Figure 4-42 Surface stress comparison of residual stress area specimens

4.6.1.6 Effect of Height

In order to analyze the height effect on residual stresses by the LPBF process, the following specimens were additionally produced;

n. 30µm layer thickness with meander scanning strategy (30-M) and 67° rotation with 16mmx16mmx24mm dimensions as numbered “specimen#14” in Figure 4-43,
o. 30µm layer thickness with meander scanning strategy (30-M) and 67° rotation with 16mmx16mmx32mm dimensions as numbered “specimen#15” in Figure 4-43,

p. 30µm layer thickness with meander scanning strategy (30-M) and 67° rotation with 16mmx16mmx48mm dimensions as numbered “specimen#16” in Figure 4-43,
q. 30µm layer thickness with meander scanning strategy (30-M) and 67° rotation with 16mmx16mmx64mm dimensions as numbered “specimen#17” in Figure 4-43,

as given in Figure 4-43. The angles stated on the specimens were the top layers’ final scanning angles. The scanning angles were rotated 67° in Counter Clockwise (CCW) direction for specimens#14, 15, 16 and 17. Summary of the residual stress measurement specimen properties for specimens#9, #14, #15, #16 and #17 is given in Table 4-13.

Table 4-13 Height effect on residual stresses specimen properties

No	Specimen	Layer Thickness	Scanning Strategy	Rotation	Specimen Dimension [mm] (X-Y-Z Directions)	Fluorescent Penetrant Inspection Result
i.	Specimen#9	30µm	Meander	67°	16x16x10	Passed
n.	Specimen#14	30µm	Meander	67°	16x16x24	Passed
o.	Specimen#15	30µm	Meander	67°	16x16x32	Passed
p	Specimen#16	30µm	Meander	67°	16x16x48	Passed
q	Specimen#17	30µm	Meander	67°	16x16x64	Passed

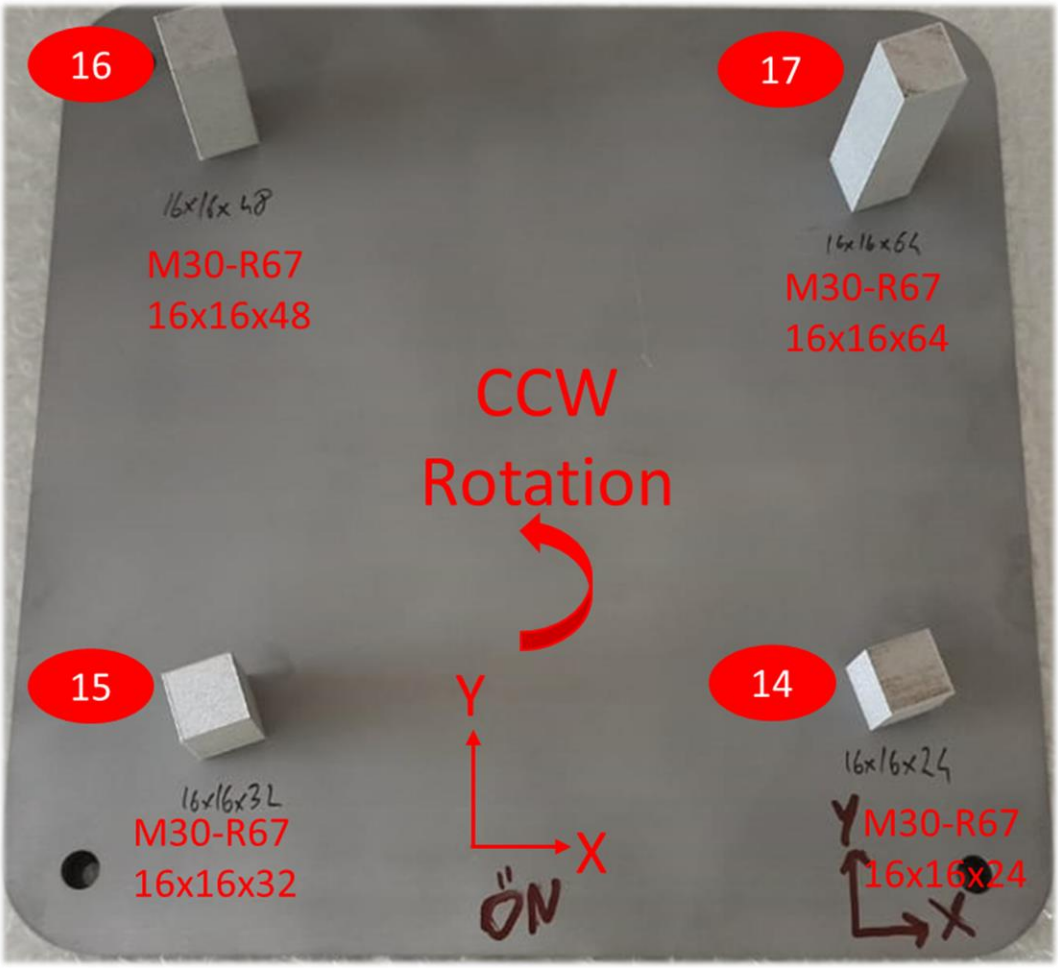

Figure 4-43 30-M 16mmx16mmx24mm Rotation 67° (specimen#14), 30-M 16mmx16mmx32mm Rotation 67° (specimen#15), 30-M 16mmx16mmx48mm Rotation 67° (specimen#16), 30-M 16mmx16mmx64mm Rotation 67° (specimen#17)

Effects of height on residual stresses results are given in Table 4-14.

Table 4-14 Effects of height on residual stresses

No of XRD Measurement	Part Name	Specimen Dimension [mm] (X-Y-Z Directions)	*Measurement Depth (mm)*	*Principal Stresses*		
				σ max (MPa)	*σ min (MPa)*	*φ (σ max) (°)*
1	Specimen#9	16x16x10	0,0000	540	276	4,8 ± 4,9
2	Specimen#9	16x16x10	0,0150	531	402	11,4 ± 9,3
3	Specimen#9	16x16x10	0,1350	574	381	4,2 ± 8
4	Specimen#14	16x16x24	0,0000	522	285	21 ± 4
5	Specimen#14	16x16x24	0,0160	504	348	20,9 ± 4,5
6	Specimen#14	16x16x24	0,1100	541	341	22,2 ± 4,4
7	Specimen#15	16x16x32	0,0000	509	284	-57 ± 3,9
8	Specimen#15	16x16x32	0,0160	490	335	-56,5 ± 6,7
9	Specimen#15	16x16x32	0,1050	523	330	-52,1 ± 3,6
10	Specimen#16	16x16x48	0,0000	468	297	56,3 ± 5,4
11	Specimen#16	16x16x48	0,0140	448	396	55,8 ± 9,4
12	Specimen#16	16x16x48	0,1070	482	318	68,5 ± 7,7
13	Specimen#17	16x16x64	0,0000	435	326	-19,2 ± 11,1
14	Specimen#17	16x16x64	0,0150	458	385	-7,4 ± 16,3
15	Specimen#17	16x16x64	0,1060	450	334	-8,2 ± 9,8

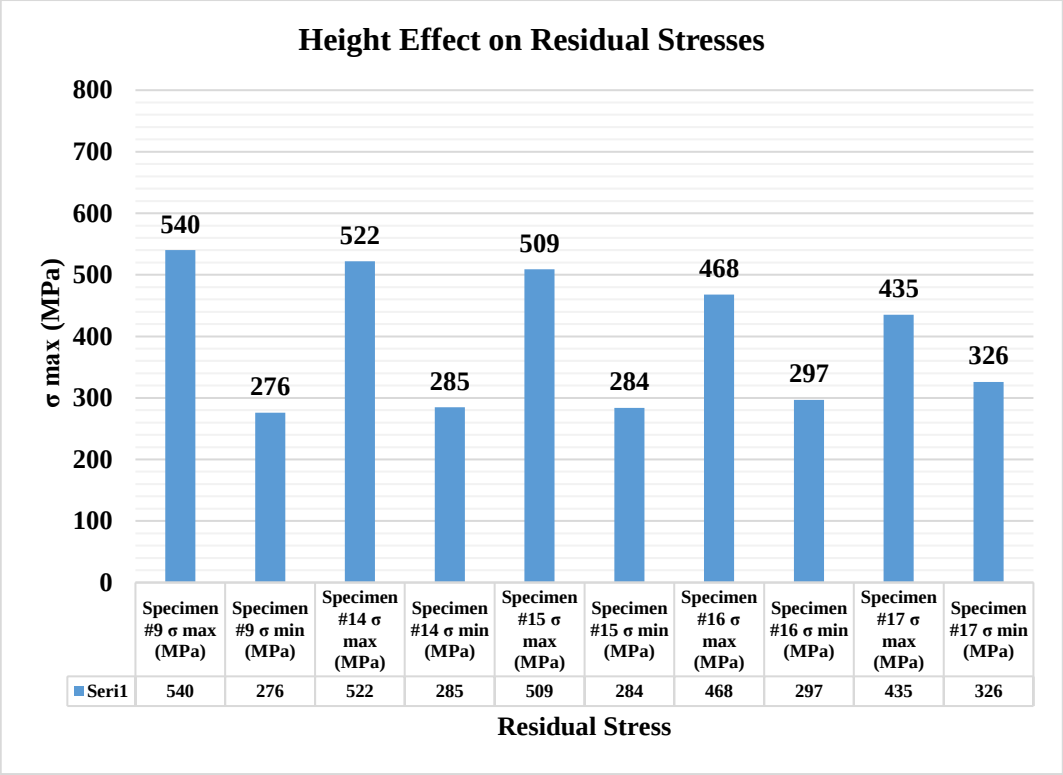

Figure 4-44 Surface stress comparison of residual stress for height specimens

Surface stress comparison of residual stress for height specimens is given in Figure 4-44. Residual stress values were decreased for σ max residual stresses as height increased. It is important to note that, for surface stresses, similar XRD residual stress trend was observed with the simulation analysis.

4.6.1.7 Support Structure

Residual stresses with support structure were also measured. Specimen with support structure is given in Figure 4-45. The support structure was produced with general support material structure process parameters, and the top layers were produced with 30-M scanning strategy process parameters, as given in Table 3-1.

Figure 4-45 Specimen with support structure

Residual stress values were compared with σ max residual stress results. Support used structure residual stress results are given in Table 4-15 and the graph is shown in Figure 4-46. The residual stresses slightly increase and gradually decrease as same as with the support-free structures when compared the results given in Table 4-8. Furthermore, Support used structure residual stress results are relatively lower than the support-free structures, particularly at the lower layers of the specimen. Having relatively more open surfaces might be a potential effect of residual stress relief and lower residual stresses on materials.

Table 4-15 Support structure residual stress results

No of XRD Measurement	Part Name	*Measurement Depth (mm)*	*Principal Stresses*		
			σ max (MPa)	*σ min (MPa)*	*φ(σ max)(°)*
1	Support	0,0000	519	270	88,7 ± 11,8
2	Support	0,0150	612	412	67,9 ± 11
3	Support	0,0490	656	419	68,7 ± 11,5
4	Support	0,0770	627	334	78,9 ± 9,3
5	Support	0,1050	644	390	89,2 ± 10,3
6	Support	0,1340	665	321	88,9 ± 5,4
7	Support	0,1640	707	323	80,8 ± 3,9
8	Support	0,1950	459	269	85,7 ± 7,6
9	Support	0,2250	271	83	-86,2 ± 8,6
10	Support	0,2560	200	69	-87,8 ± 14,6
11	Support	0,2830	154	98	63,9 ± 26,6
12	Support	0,3140	251	104	82,7 ± 12,7

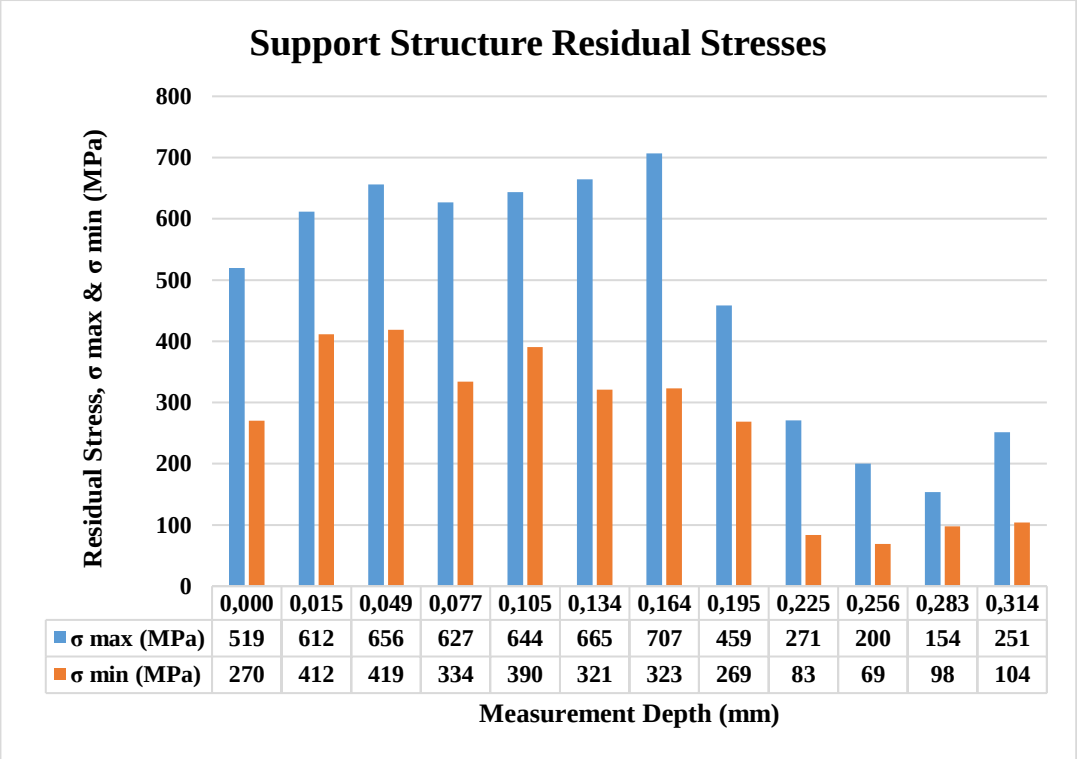

Figure 4-46 Support structure residual stress graph

4.6.1.8 Preheating Effect

Conventional 17-4 PH stainless steels can be in martensitic, austenitic, semi-austenitic, and stable δ (delta) ferritic microstructure at ambient temperatures as mentioned in section 2.2.5. Preheating of the baseplate at 170°C idea was analyzed for prevention or minimization of martensite formation in the LPBF to accumulate fewer residual stresses by keeping all processes above martensite start (M_s) temperature (~135°C). However, the as-built and 170°C pre-heat applied specimens' residual stress values were almost at the same level as given in Figure 4-49 and Figure 4-31. Alnajjar et al.'s study [77] indicates that, high heating and cooling rates (10^5-10^5 K/s) cause austenite by-passing, as explained in detail in section 4.1.1. Due to austenite by-passing effect, austenite formation is prevented during the heating

and cooling of each LPBF process layers. Therefore, martensite is not generated as in conventional 17-4 PH stainless steels. Thus, almost the same residual stress values were obtained by mainly having stable δ (delta) ferrite phase [77] for the as-built and 170°C pre-heat applied specimens. Preheating at 170°C might contribute to fewer delta temperature changes (~150°C) during each heating and cooling cycle. However, residual stress measurement results indicate that the delta temperature change (~150°C) is ignorable compared to other dominant residual stress effects.

Preheating of the baseplate was performed at 170°C for specimens given below;

r. 30µm layer thickness with meander scanning strategy (30-M) and 30° rotation as numbered “specimen#18” in Figure 4-47,
s. 30µm layer thickness with stripe scanning strategy (30-S) and 30° rotation as numbered “specimen#19” in Figure 4-47,
t. 60µm layer thickness with meander scanning strategy and 30° rotation as numbered (60-M) “specimen#20” in Figure 4-47,
u. 60µm layer thickness with stripe scanning strategy (60-S) and 30° rotation as numbered “specimen#21” in Figure 4-47.

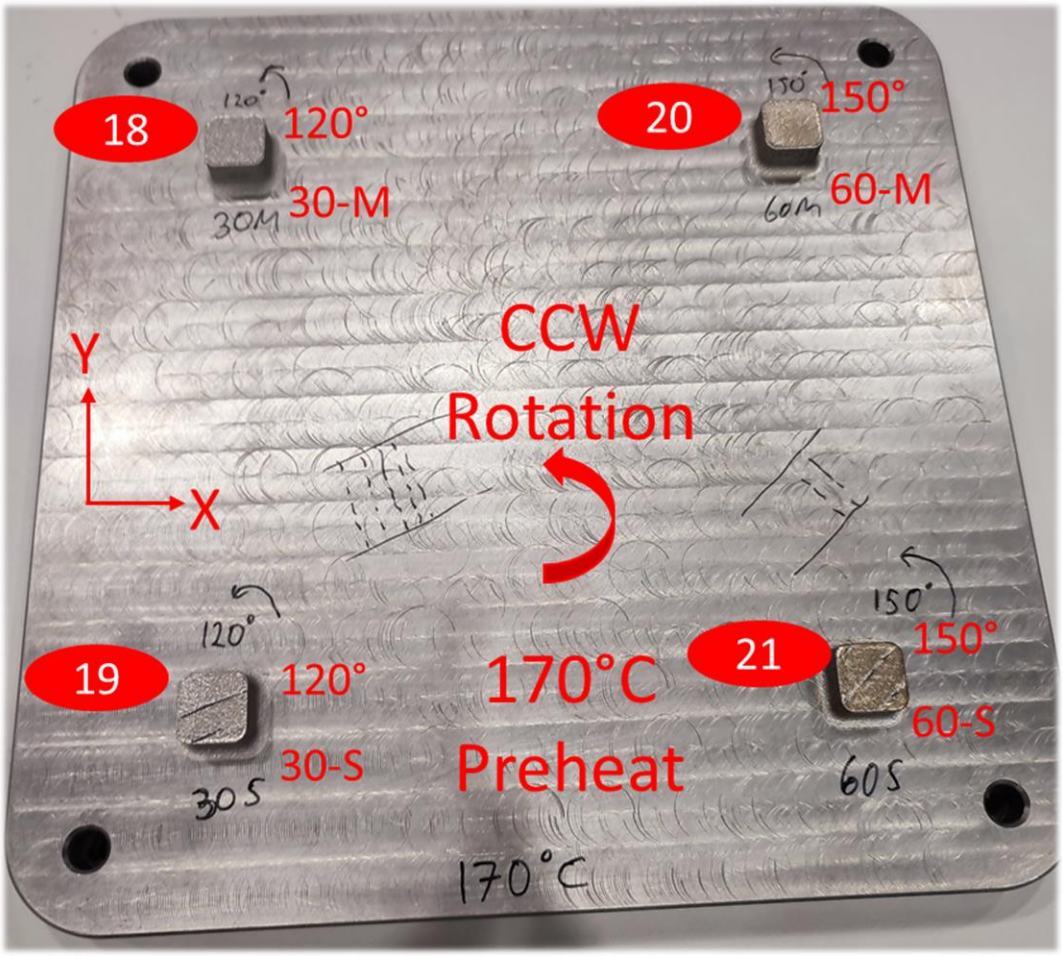

Figure 4-47 170°C preheat specimens

Residual stress values were compared with σ max residual stress results. 170°C Preheat residual stress measurement specimen properties are given in Table 4-16. Cracks and delamination were detected on 170°C Preheated 60µm layer thickness with stripe scanning strategy (60-S) specimen as shown in Figure 4-48. Therefore, the 60-S specimen had not been taken into consideration in terms of residual stress analysis.

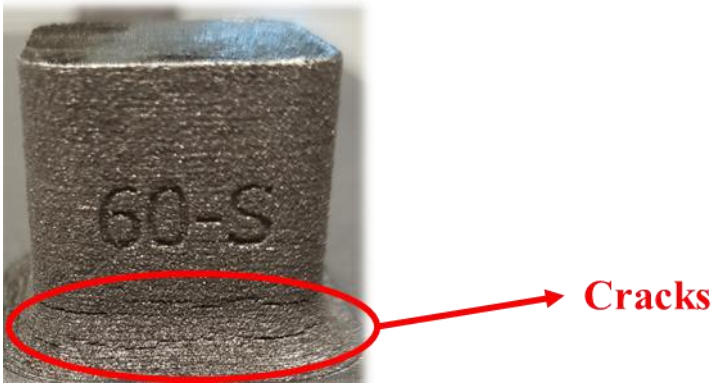

Figure 4-48 Cracks and delamination detected on preheated 60-S scanning strategy specimen

Table 4-16 170°C Preheat residual stress measurement specimen properties

No	Specimen	Specimen Notation	Layer Thickness	Scanning Strategy	Specimen Dimension [mm] (X-Y-Z Directions)	Fluorescent Penetrant Inspection Result
r.	Specimen#18	30-M-170°C	30µm	Meander	16x16x10	Passed
s.	Specimen#19	30-S-170°C	30µm	Stripe	16x16x10	Passed
t.	Specimen#20	60-M-170°C	60µm	Meander	16x16x10	Passed
u.	Specimen#21	60-S-170°C	60µm	Stripe	16x16x10	Crack Detected

4.6.1.8.1 170°C Preheated 30µm Layer Thickness with Meander Scanning Strategy (30-M) "Specimen#18"

Preheated, 30µm layer thickness with meander scanning strategy (30-M) structure residual stress results are given in Table 4-17 and the principal stresses graph is

shown in Figure 4-49. Preheated 30-M sample residual stresses also firstly slightly increase and then decrease. Preheated 30-M sample, σ min residual stress values were slightly lower than the 30-M sample.

Table 4-17 30-M preheat structure residual stress results

No of XRD Measurement	Part Name	*Measurement Depth (mm)*	*Principal Stresses*		
			σ max (MPa)	*σ min (MPa)*	*φ(σ max)(°)*
1	30-M Preheat	0,0000	546	193	73,9 ± 7,8
2	30-M Preheat	0,0160	612	265	67,3 ± 9,5
3	30-M Preheat	0,0510	666	490	70,2 ± 15,8
4	30-M Preheat	0,0800	635	328	57,8 ± 8,2
5	30-M Preheat	0,1030	646	275	61 ± 6,9
6	30-M Preheat	0,1330	640	244	71,5 ± 7
7	30-M Preheat	0,1680	634	240	69 ± 4,7
8	30-M Preheat	0,1960	527	269	59,1 ± 6,1
9	30-M Preheat	0,2250	472	289	56,8 ± 7,5
10	30-M Preheat	0,2540	403	375	-42,2 ± 38,3
11	30-M Preheat	0,2900	392	299	24,3 ± 15
12	30-M Preheat	0,3150	400	355	-8,9 ± 48,3

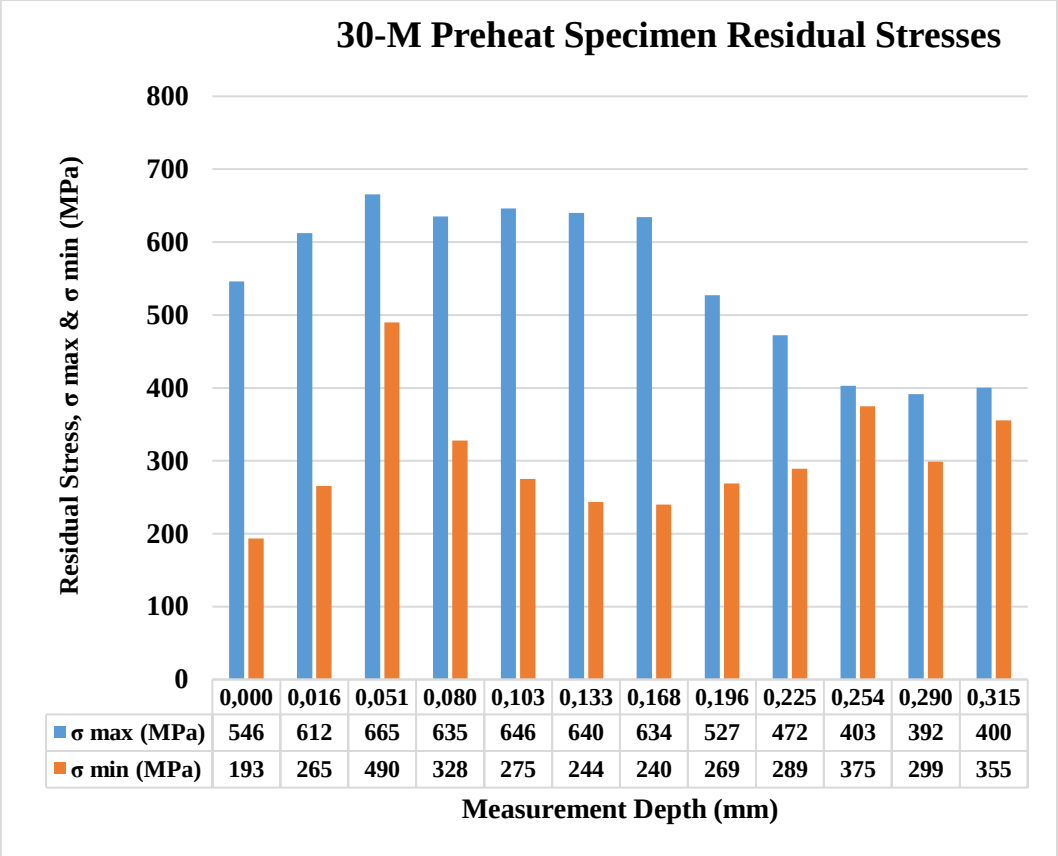

	0,000	0,016	0,051	0,080	0,103	0,133	0,168	0,196	0,225	0,254	0,290	0,315
σ max (MPa)	546	612	665	635	646	640	634	527	472	403	392	400
σ min (MPa)	193	265	490	328	275	244	240	269	289	375	299	355

Figure 4-49 30-M preheat structure residual stress graph

4.6.1.8.2 Preheated 30µm Layer Thickness with Stripe Scanning Strategy (30-S) "Specimen#19"

Residual stress values were compared with σ max residual stress results. Preheated, 30µm layer thickness with stripe scanning strategy (30-S) structure residual stress results are given in Table 4-18 and the principal stresses graph is shown in Figure 4-50.

Table 4-18 30-S preheat structure residual stress results

No of XRD Measurement	Part Name	*Measurement Depth (mm)*	*Principal Stresses*		
			σ max (MPa)	*σ min (MPa)*	*φ(σ max)(°)*
1	30-S Preheat	0,0000	725	293	-84,6 ± 8,4
2	30-S Preheat	0,0150	722	365	83,5 ± 12,6
3	30-S Preheat	0,0520	633	324	83,6 ± 20,2
4	30-S Preheat	0,0740	596	316	56,3 ± 12,5
5	30-S Preheat	0,1050	595	376	83,2 ± 14,8
6	30-S Preheat	0,1370	645	389	-86,3 ± 13,2
7	30-S Preheat	0,1630	549	333	-76,5 ± 14,2
8	30-S Preheat	0,1940	573	417	89,5 ± 21,8
9	30-S Preheat	0,2240	557	351	79,8 ± 14,3
10	30-S Preheat	0,2580	489	389	59,1 ± 17
11	30-S Preheat	0,2900	508	414	87,8 ± 35,9
12	30-S Preheat	0,3200	501	454	41,5 ± 37,4
13	30-S Preheat	0,3500	514	434	-1,9 ± 41,4

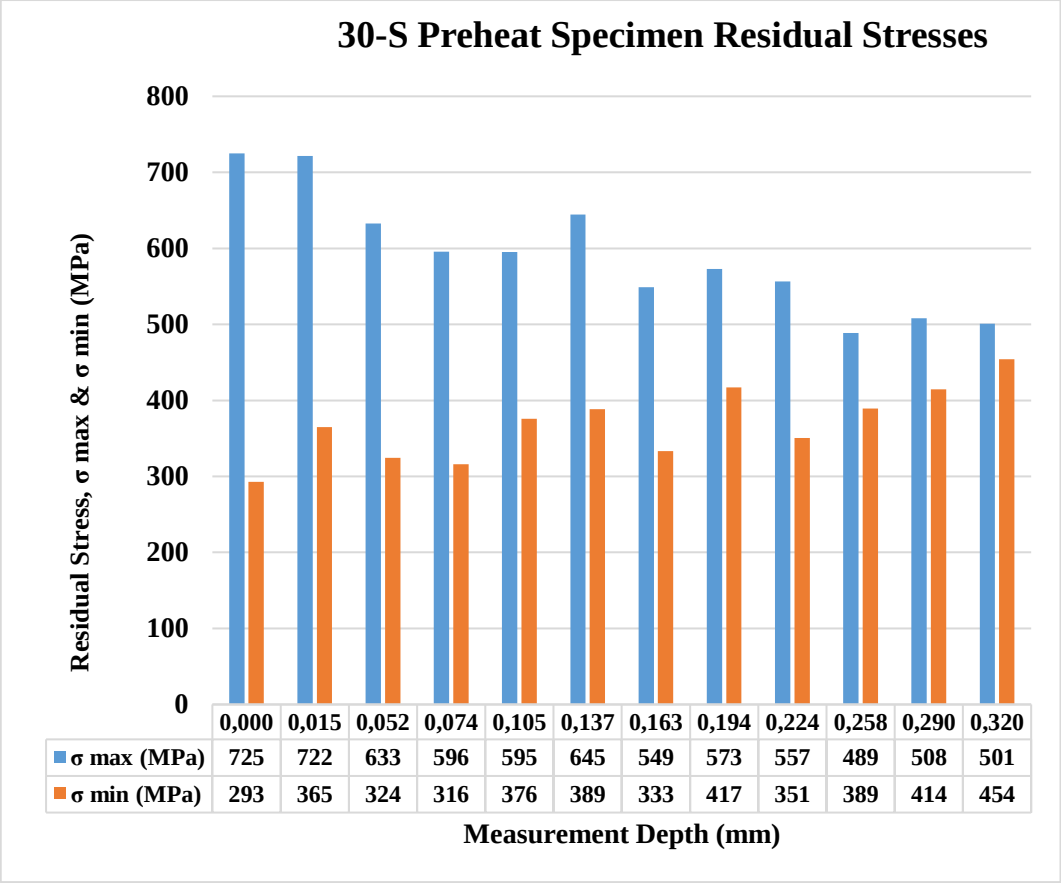

Figure 4-50 30-S preheat structure residual stress graph

4.6.1.8.3 Preheated 30µm Layer Thickness with Meander Scanning Strategy (60-M) "Specimen#20"

Residual stress values were compared with σ max residual stress results. Preheated, 60µm layer thickness with meander scanning strategy (60-M) structure residual stress results are given in Table 4-19 and the principal stresses graph is shown in Figure 4-51.

Table 4-19 60-M preheat structure residual stress results

No of XRD Measurement	Part Name	*Measurement Depth (mm)*	*Principal Stresses*		
			σ max (MPa)	*σ min (MPa)*	*φ(σ max)(°)*
1	60-M Preheat	0,0000	535	156	52,7 ± 8,1
2	60-M Preheat	0,0320	480	359	87,9 ± 57,9
3	60-M Preheat	0,0950	599	462	61,4 ± 38,5
4	60-M Preheat	0,1470	768	181	66,2 ± 8,5
5	60-M Preheat	0,2080	546	455	82,6 ± 73,9
6	60-M Preheat	0,2700	664	366	80,7 ± 16,5
7	60-M Preheat	0,3270	684	301	52,7 ± 4,9

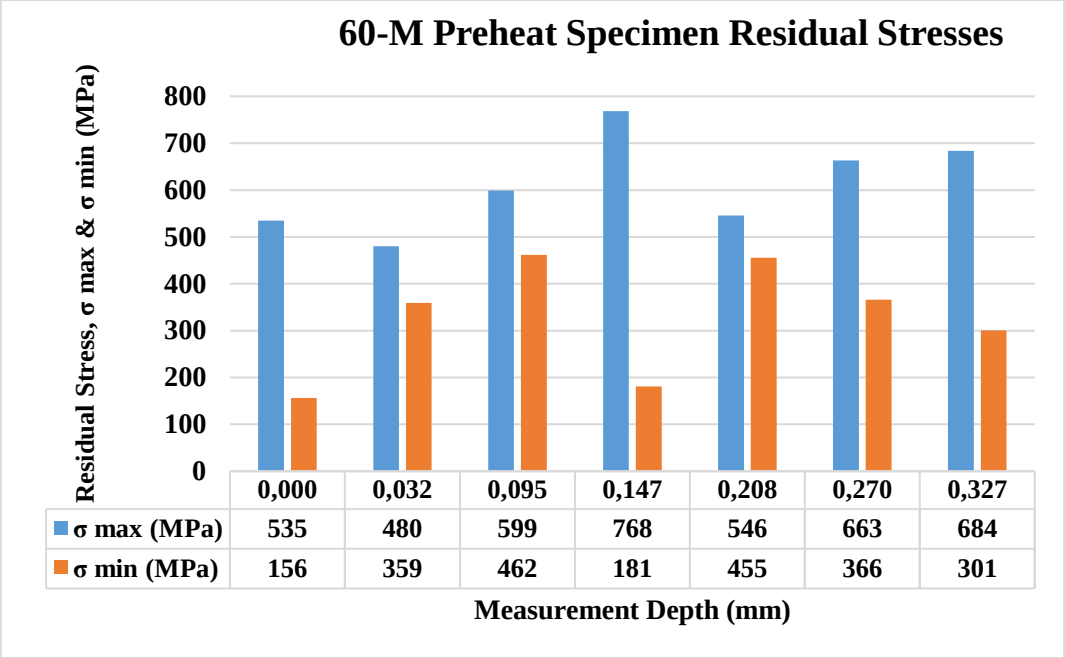

Figure 4-51 60-M preheat structure residual stress graph

4.6.1.9 EDM Separated 30-M Specimen Residual Stress Measurement

Almost all of the AM build parts are separated by the Electric Discharge Machining (EDM) process from baseplate material. In order to observe the effect of the EDM process on residual stress changes, a 30µm layer thickness with meander scanning strategy (30-M) structure was built by laser powder bed fusion process and separated from base plate material by EDM process. Residual stress values were compared with σ max residual stress results. Residual stress results of EDM separated the 30-M specimen are given in Table 4-20, and the principal stresses graph is shown in Figure 4-52. Stress relief can be observed when compared with the non-separated 30-M specimen residual stress results given in Table 4-8. However, usually high residual stresses can cause material deformation and irreversible material failures. Therefore, taking preventive actions before material failures are accepted as more crucial.

Table 4-20 EDM separated 30-M specimen residual stress results by depth

No of XRD Measurement	Part Name	*Measurement Depth (mm)*	*Principal Stresses*		
			σ max (MPa)	*σ min (MPa)*	*φ(σ max)(°)*
1	EDM Separated 30-M	0,000	492	129	-83,3 ± 7,7
2	EDM Separated 30-M	0,022	390	199	69,9 ± 16,4
3	EDM Separated 30-M	0,046	436	282	-76,6 ± 17,2
4	EDM Separated 30-M	0,073	479	230	-85,5 ± 9,4
5	EDM Separated 30-M	0,103	504	190	-88,4 ± 7,1
6	EDM Separated 30-M	0,135	554	183	-88,9 ± 5
7	EDM Separated 30-M	0,170	542	152	80,5 ± 2,7
8	EDM Separated 30-M	0,198	429	143	66,9 ± 3,1
9	EDM Separated 30-M	0,228	261	114	67,1 ± 10,9
10	EDM Separated 30-M	0,260	169	45	72 ± 11,6
11	EDM Separated 30-M	0,288	171	9	62,9 ± 7,3
12	EDM Separated 30-M	0,312	150	5	61,9 ± 9,9

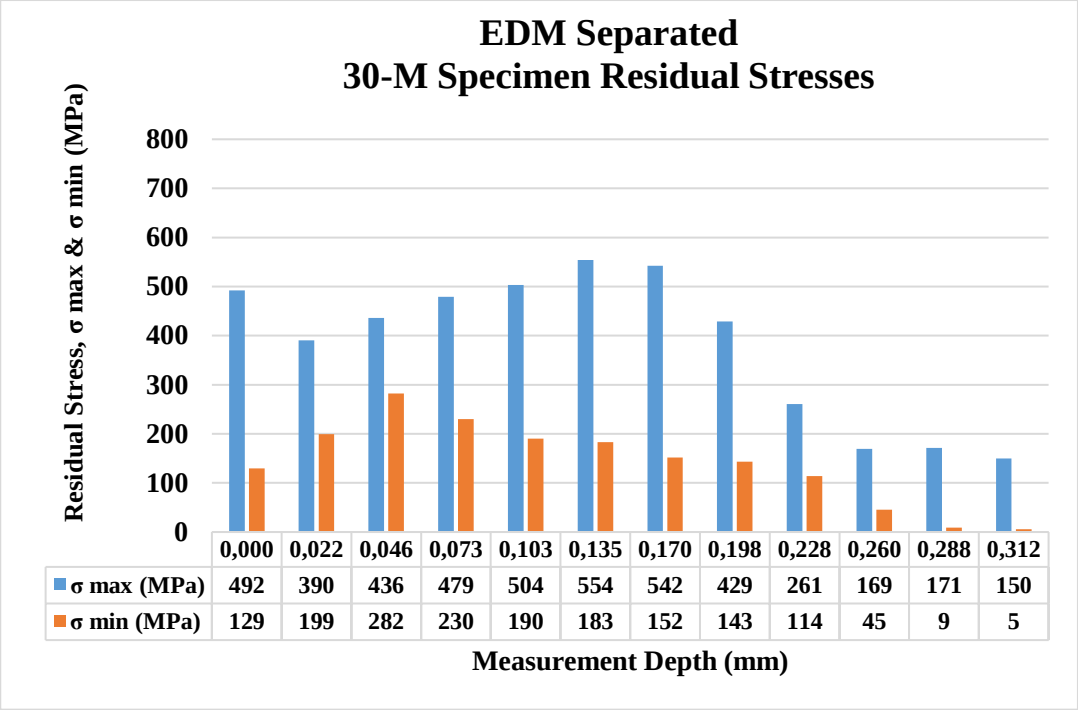

	0,000	0,022	0,046	0,073	0,103	0,135	0,170	0,198	0,228	0,260	0,288	0,312
σ max (MPa)	492	390	436	479	504	554	542	429	261	169	171	150
σ min (MPa)	129	199	282	230	190	183	152	143	114	45	9	5

Figure 4-52 EDM separated 30-M specimen residual stress graph

4.6.1.10 Design of Experiment-I; Power, Point Distance, Hatch Distance Effect for Pulsed Mode Additive Manufacturing

Among the process parameters; Laser Power, Point Distance, and Hatch Distance have a major effect on Laser Powder Bed Fusion (LPBF) process for proper material production. These process parameters are particularly critical in proper production for pulsed mode additive manufacturing systems as details of pulsed wave LPBF process parameter properties were given in section 2.1.1.1. Therefore, it was found worth to investigate Laser Power, Point Distance, and Hatch Distance effect for pulsed mode LPBF for 17-4 PH stainless steel parts. Laser Power, Point Distance, and Hatch Distance effect investigation was performed by Design of Experiment-I (DOE-I) setup where details are given below. The production was conducted with 30µm layer thickness and Meander scanning strategy. Specimen dimensions are

16mmx16mmx10mm (X-Y-Z directions). Volumetric Energy Density (VED) calculation variables used for this DOE as given in *Equation 3*. The constants of this DOE setup are shown in Table 4-21. Exposure time values were calculated by *Equation 3* for each run.

Power, Point Distance, and Hatch Distance effect investigation DOE samples are given in Figure 4-53. Statistical analysis was performed with Minitab Data Analysis Software, Version 18.

Table 4-21 Power, point distance, hatch distance effect constant parameters

Layer Thickness	**Scanning Strategy**	**Rotation**	**Specimen Dimension [mm] (X-Y-Z Directions)**	**VED (J/mm^3)**
30µm	Meander	67°	16x16x10	101

Power, point distance, hatch distance design factor information and summary are given in Table 4-22 and Table 4-24, respectively.

The DOE values were defined within the optimum parameter range to obtain a fully dense structure, as shown in Figure 2-10. Otherwise, cracks could be observed on specimens, and residual stress evaluations could not be conducted properly.

Table 4-22 Power, point distance, hatch distance design factor information

Design Factor Information		
Factor	**Levels**	**Values**
Power (W)	3	200, 275, 350
Point Distance (µm)	3	70, 90, 110
Hatch Distance (µm)	3	70, 90, 110

Table 4-23 Power, point distance, hatch distance design of experiment summary

Design Summary	
Factors	3
Base Runs	27
Base Blocks	1
Replicate	1
Total Runs	27
Total blocks	1

Figure 4-53 Power, point distance, hatch distance effect investigation DOE-I samples

Stepwise backward elimination was performed by Minitab software, and alpha to remove 0,15 was selected. Calculated R-squared and R-square adjusted values are 86,76% and 71,30%, respectively.

Residual stress values were measured from 105±5 µm depth, and σ max (MPa) values were taken into consideration. The measured residual stress values are given in Table 4-24.

Table 4-24 Power, point distance, hatch distance effect residual stress values

No	Laser Power (W)	Point Distance (µm)	Hatch Distance (µm)	Exposure Time(µs)	VED Given Hatch (J/mm3)	σ max (MPa) 105±5(µm)
1	275	70	110	85	101	462
2	350	70	70	42	101	384
3	200	90	110	150	101	554
4	350	70	90	55	101	333
5	350	110	70	67	101	363
6	200	110	70	117	101	548
7	350	90	70	55	101	436
8	275	90	110	109	101	519
9	350	90	110	86	101	342
10	275	110	70	85	101	379
11	275	70	70	54	101	399
12	200	110	90	150	101	608
13	350	90	90	70	101	245
14	200	70	90	95	101	457
15	200	90	90	123	101	513
16	275	110	90	109	101	528
17	200	90	70	95	101	624
18	275	110	110	133	101	433
19	200	70	70	74	101	648
20	350	70	110	67	101	327
21	275	70	90	69	101	487
22	350	110	110	105	101	365
23	275	90	70	69	101	531
24	275	90	90	89	101	553
25	350	110	90	86	101	333
26	200	70	110	117	101	514
27	200	110	110	183	101	660

The Pareto chart indicates that laser power has the main influence on residual stress accumulation as given in Figure 4-54. It can be concluded that laser power's influence on residual stress accumulation is due to being a high-energy input source. Normal probability data fits with the graph and the histogram have an ideal shape as given in Figure 4-55. In this DOE-I, by keeping the VED value constant, exposure time indirect effect was also analyzed. Power value with 200W accumulates higher stresses than 350W value as given in Figure 4-56 and Figure 4-57 since the VED value is kept constant. When power decreases, exposure time value increases in accordance with *Equation 3* to get constant 101 J/mm^3 value. Therefore, it can be said that exposure time has an indirect influence on residual stresses. On the other hand, point distance and hatch distance has a slight influence when compared with the effect of laser power as given in Figure 4-57.

DOE-I results within the defined ranges indicated that, the process parameters of No 13 given in Table 4-24 provided the minimum residual stress level by having 245MPa σ max residual stresses at 105±5(µm) depth. When the results were compared with the conventional 30-M process parameters given in Figure 4-31, as an advantage, the σ max residual stress level was decreased from 754MPa to 245MPa (~67% less). However, tensile strength of the material decreased from 925MPa to 793MPa (~14% less), yield strength of the material decreased from 855MPa to 755MPa (~12% less) and maximum homogenous strain value decreased from 8,2% to 7,9% (~4% less) as disadvantages. Moreover, DOE-I results within the defined ranges also indicate that, process parameters with high laser power and less exposure time provided lower residual stresses. Having fully dense parts with high laser source with less exposure time has also decreased production time of the parts which was desired by industry by having fewer residual stresses. Therefore, trade-off shall be considered between fewer surface residual stress values and mechanical strength in an engineering perspective. Obtaining fully dense parts with less residual stresses shall be considered within the range of the specified triangle as given in Figure 2-10.

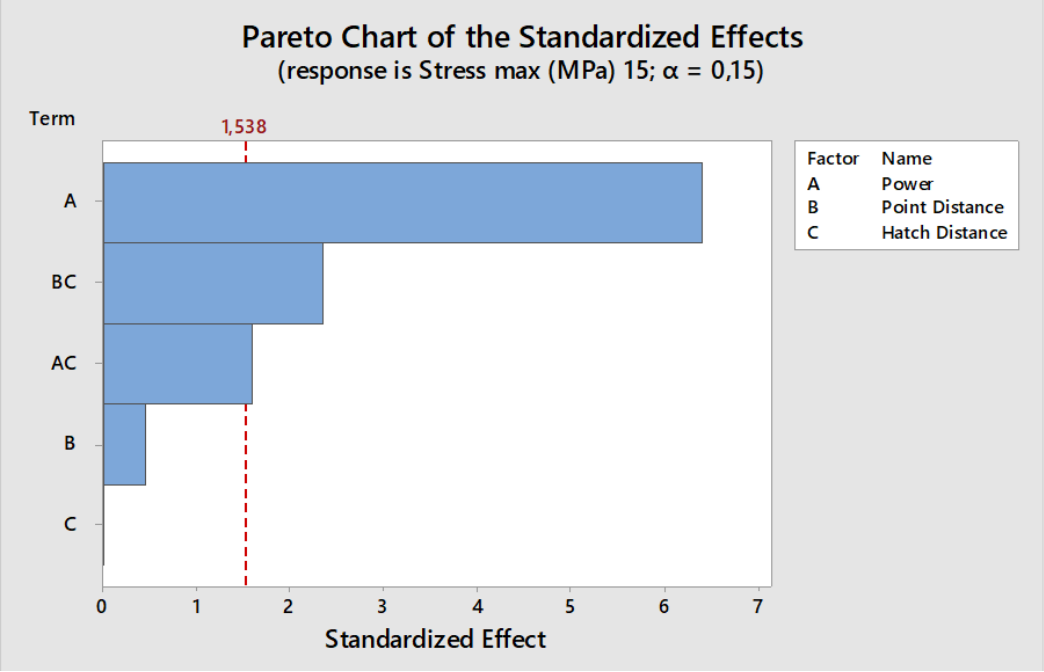

Figure 4-54 Pareto chart of power, point distance, hatch distance effect

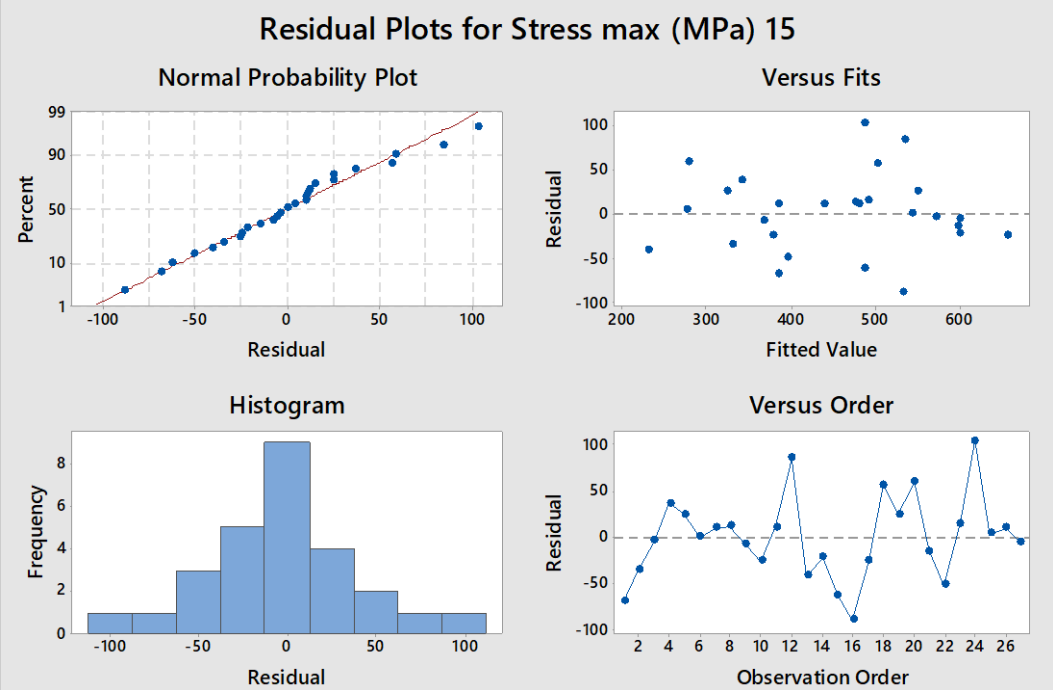

Figure 4-55 Residual plots of power, point distance, hatch distance effect

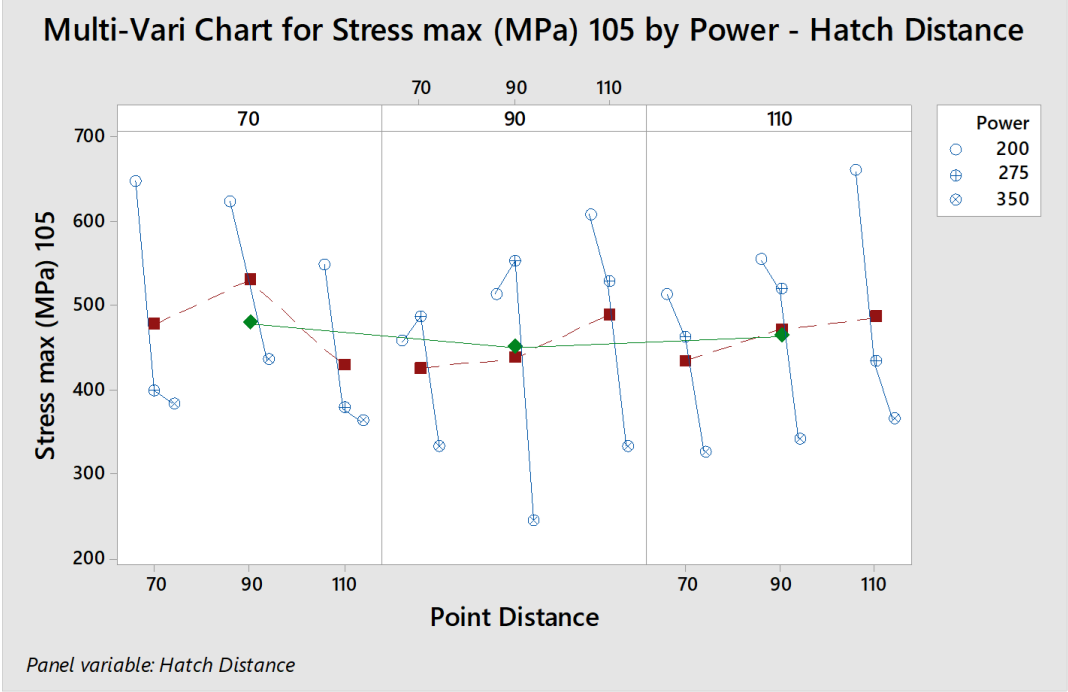

Figure 4-56 Multi-Vari chart of power, point distance, hatch distance effect

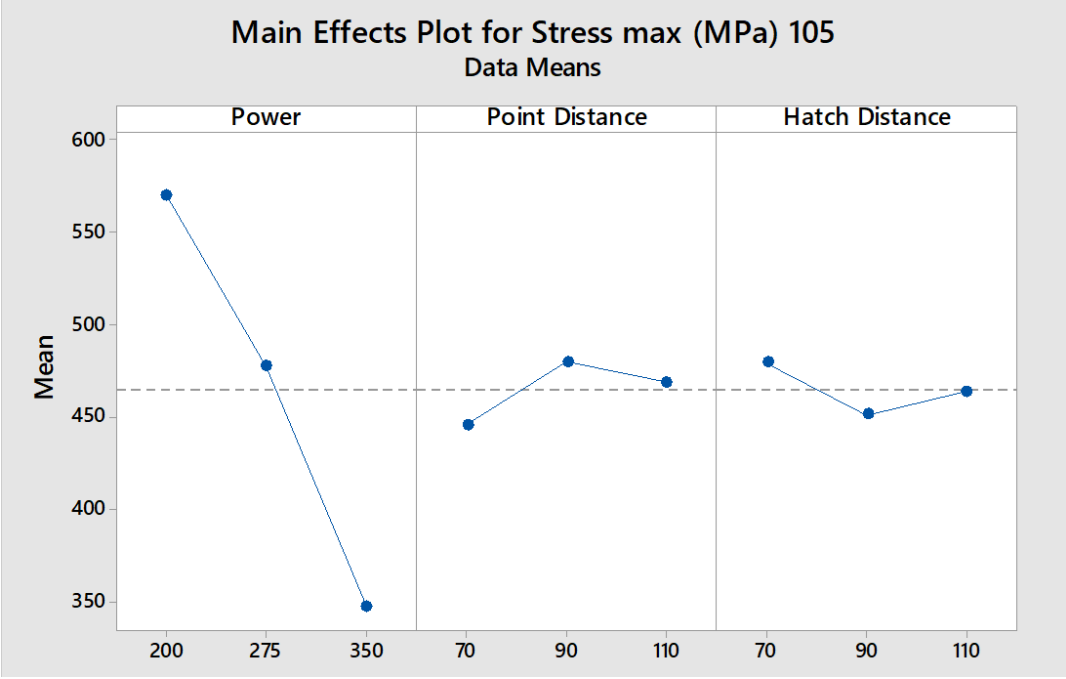

Figure 4-57 Main effects plot of power, point distance, hatch distance effect

4.6.1.11 Design of Experiment-II; Exposure Time, Volumetric Energy Density, Point Distance, Hatch Distance Effect for Pulsed Mode Additive Manufacturing

Major influence of Power on the Laser Powder Bed Fusion (LPBF) process was indicated in section 4.6.1.10. Analysis for Exposure Time, Volumetric Energy Density, Point Distance, and Hatch Distance effect for pulsed mode additive manufacturing was conducted within this section. Exposure Time, Volumetric Energy Density, Point Distance, and Hatch Distance effect investigation were performed by Design of Experiment-II (DOE-II) setup, where details are given below. The production was performed with 30µm layer thickness and Meander scanning strategy. Power calculation was conducted by *Equation 3*. The constants of this DOE setup are given in Table 4-25. Exposure Time, Volumetric Energy Density, Point Distance, and Hatch Distance effect investigation DOE samples are shown in Figure 4-58. Statistical analysis was performed with Minitab Data Analysis Software, Version 18.

Figure 4-58 Exposure time, volumetric energy density, point distance, hatch distance effect investigation DOE-II samples

Table 4-25 Exposure time, volumetric energy density, point distance, hatch distance design constant parameters

Layer Thickness	Scanning Strategy	Rotation	Specimen Dimension [mm] (X-Y-Z Directions)
30µm	Meander	67°	16x16x10

Exposure time, volumetric energy density, point distance, hatch distance design factor summary, and design information are given in Table 4-26 and Table 4-27, respectively.

Table 4-26 Exposure time, volumetric energy density, point distance, hatch distance design factor information

Design Factor Information		
Factor	**Levels**	**Values**
Exposure Time (µs)	2	86, 142
Volumetric Energy Density (J/mm^3)	2	78, 101
Point Distance (µm)	2	70, 110
Hatch Distance (µm)	2	70, 110

Table 4-27 Exposure time, volumetric energy density, point distance, hatch distance design of experiment summary

Design Summary	
Factors	4
Base Design	4; 16
Base Blocks	1
Replicate	1
Center Points	1
Total Runs	17

Residual stress values were measured from 105±5 µm depth and σ max (MPa) values were taken into consideration. The measured residual stress values are given in Table

4-28. No 9 process parameters were the center point attained by Minitab Data Analysis Software process parameters which are given in Table 4-28. No 9 laser power is within the limit of Renishaw AM400 laser power which is not usually desired.

Table 4-28 Exposure time, volumetric energy density, point distance, hatch distance effect residual stress values

No	Exposure Time(µs)	VED Given Hatch (J/mm3)	Point Distance (µm)	Hatch Distance (µm)	Power(W)	σ max (MPa) 105±5(µm)
1	142	101	110	70	164	586
2	86	78	70	70	133	605
3	142	78	70	110	127	630
4	142	78	110	70	127	657
5	142	78	110	110	199	650
6	86	78	70	110	210	678
7	86	101	70	110	271	400
8	114	89,5	90	90	191	648
9	86	101	110	110	400	605
10	142	101	70	70	105	486
11	142	78	70	70	81	622
12	142	101	110	110	258	574
13	86	101	70	70	173	557
14	86	78	110	110	329	562
15	142	101	70	110	164	684
16	86	101	110	70	271	443
17	86	78	110	70	210	612

Stepwise backward elimination was performed by Minitab software and alpha to remove 0,15 was selected. The center point was assigned for analysis. Calculated R-squared and R-square adjusted values are 98,54% and 94,16%, respectively.

In accordance with the results of this DOE-II, Volumetric Energy Density and Exposure Time have the primary influence on residual stress formation as given in Figure 4-59. Normal probability data fits with the graph in Figure 4-60. The main effect plot of exposure time, volumetric energy density, point distance, and hatch distance is shown in Figure 4-61. The main effect plot indicates that average values of exposure time, volumetric energy density, point distance, hatch distance accumulate higher residual stresses. The interaction plot shows that higher VED and low exposure time provide lower residual stresses as given in Figure 4-62. Hatch distance and point distance have a minor influence on residual stresses within the defined ranges. Exposure time, volumetric energy density, point distance, hatch distance effect DOE-II proves the cruciality of exposure time process parameter optimization for residual stress minimization in pulsed mode additive manufacturing system as similar results were observed with power, point distance, hatch distance effect DOE-I.

DOE-II results within the defined ranges indicated that, the process parameters of No 7 given in Table 4-28 provided the minimum residual stress level by having 400MPa σ max residual stresses at 105±5(µm) depth. When the results were compared with the conventional 30-M process parameters given in Figure 4-31, as an advantage, the σ max residual stress level was decreased from 754MPa to 400MPa (~47% less). However, tensile strength of the material decreased from 925MPa to 802MPa (~13% less), yield strength of the material decreased from 855MPa to 760MPa (~11% less) and maximum homogenous strain value decreased from 8,2% to 8,1% (~2% less) as disadvantages. The process parameters of No 9 given in Table 4-28 are not considered by having 400W laser power which is out of the range of the specified triangle which is shown in Figure 2-10. Among the exposure time of 86µs with VED value of 101J/mm^3 parameters, No 7 and No 16 provided the lowest surface residual stress level, proving the discussion given for DOE-I. As a result, the

VED parameter is crucial for overall penetration and residual stress on material with high power and less exposure time within the defined parameter range.

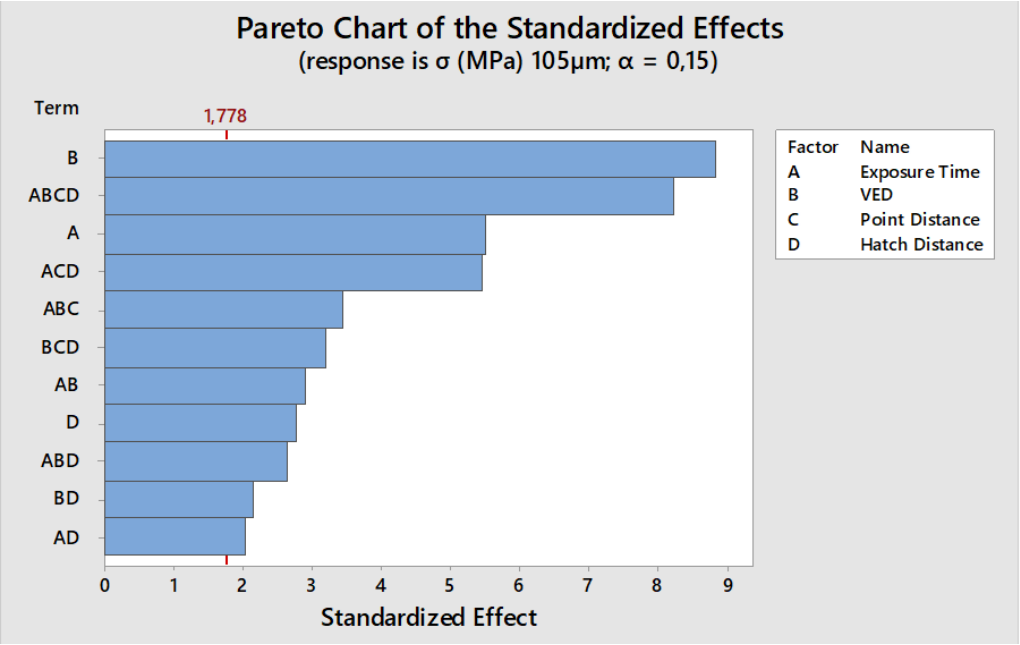

Figure 4-59 Pareto chart of exposure time, volumetric energy density, point distance, hatch distance effect

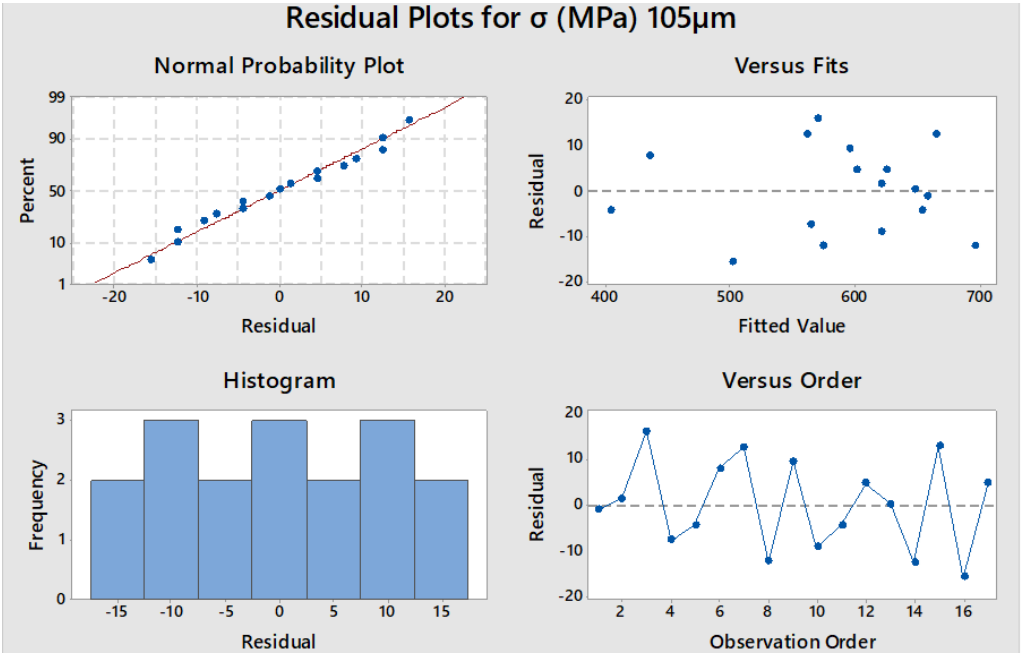

Figure 4-60 Residual plots of exposure time, volumetric energy density, point distance, hatch distance effect

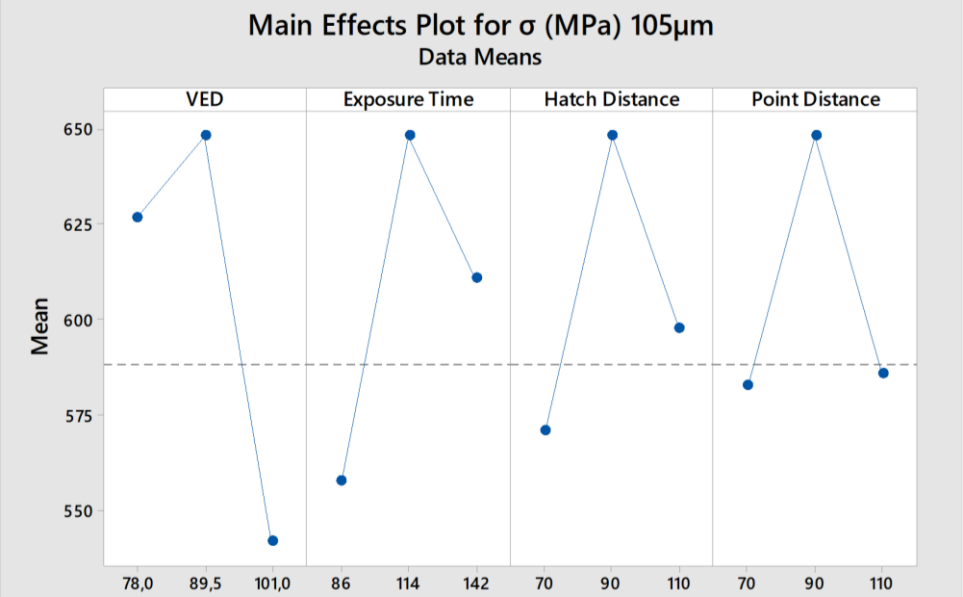

Figure 4-61 Main effect plot of exposure time, volumetric energy density, point distance, hatch distance

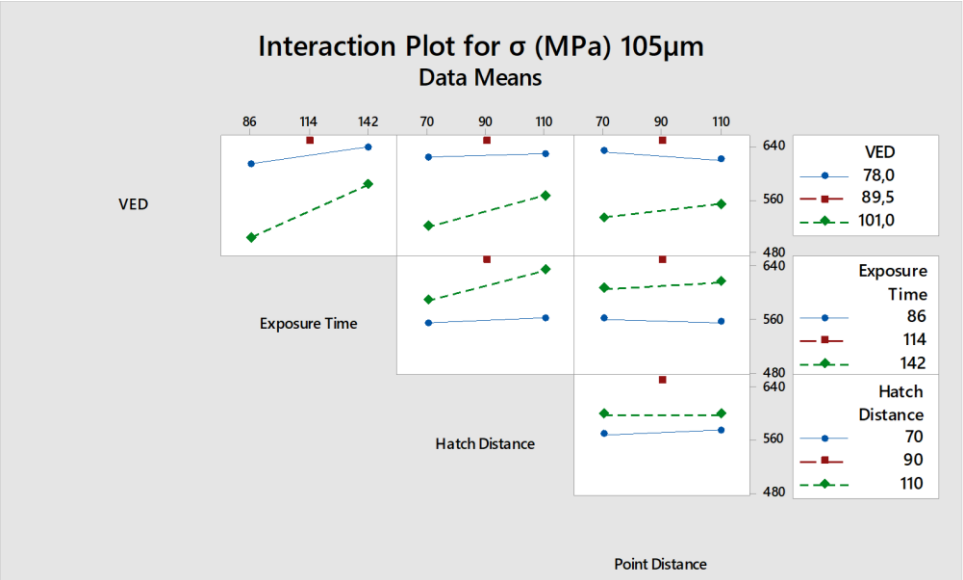

Figure 4-62 Interaction plot of exposure time, volumetric energy density, point distance, hatch distance

4.6.1.12 Control Specimen - Bar (H900)

The control specimen was produced from H900 heat-treated, bar formed in 1,5cm Ø, 17-4 PH stainless steel specimen compatible with ASTM A564 standard. XRD residual stress measurement results of the control specimen are given in Table 4-29, and the graph is shown in Figure 4-63. Residual stress values are very low in values when compared with the additive manufacturing specimens due to the nature of production methods. Control specimen residual stress results show the importance of investigation of residual stresses of additively manufactured parts.

Table 4-29 Control specimen - bar (H900) residual stress results

No of XRD Measurement	Part Name	*Measurement Depth (mm)*	*Principal Stresses*		
			σ max (MPa)	*σ min (MPa)*	*φ(σ max)(°)*
1	Control Bar Specimen H900	0,0000	10	-8	40,4 ± 16,1
2	Control Bar Specimen H900	0,0160	39	31	70,1 ± 47,6
3	Control Bar Specimen H900	0,1040	48	38	-57,2 ± 28,8

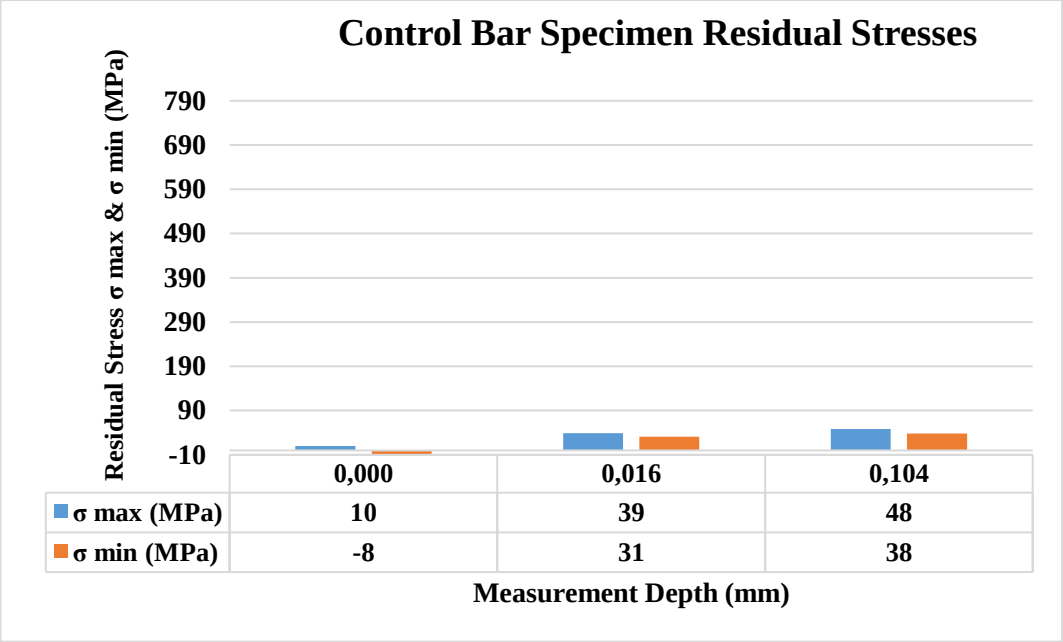

Figure 4-63 Control specimen - bar (H900) residual stress results

4.6.1.13 Retained Austenite Measurement by XRD

Retained austenite content was analyzed to compare with the results of Alnajjar et al. [77]. Retained austenite phase was measured by a Vanadium filter and a 2mm collimator. Any retained austenite could not be detected, as given in Figure 4-64, where retained austenite concentration can be measured as low as 2%. The obtained results are the same as the study of Alnajjar et al., as discussed in Section 4.1.1.

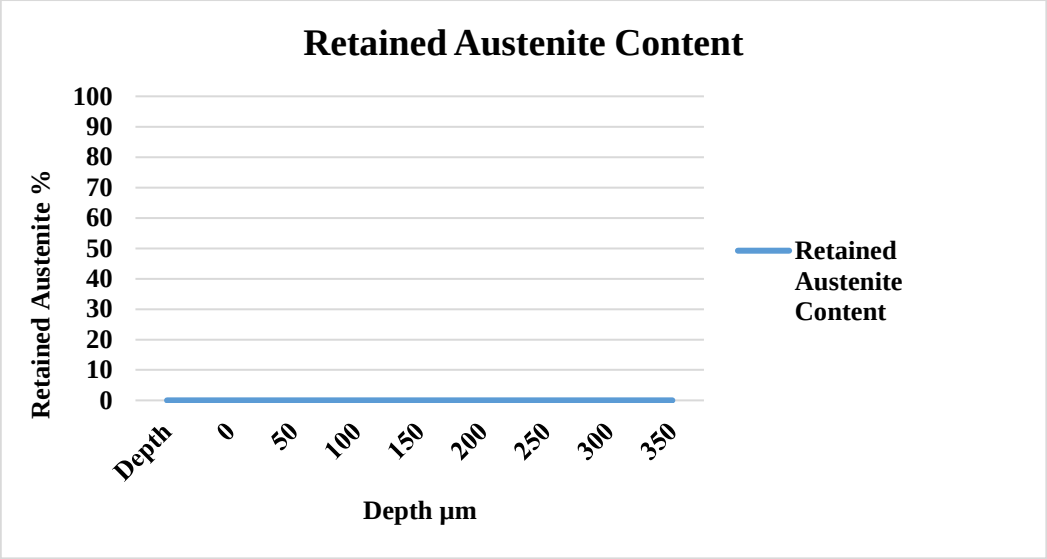

Figure 4-64 Retained austenite content within 17-4 PH LPBF specimen

CHAPTER 5

CONCLUSION

In this study, 17-4 PH stainless steel specimens were produced by pulsed mode laser powder bed fusion additive manufacturing system. The effect of scanning strategies, layer thickness, preheating of the baseplate, laser power, exposure time, volumetric energy density, hatch distance, point distance, and separation from the base plate on surface and subsurface residual stresses were examined by XRD residual measurement method.

Process parameters have very crucial effects on residual stress formation for additive manufacturing parts. Non-uniform thermal plasticity and microstructure formation causes high residual stresses which change materials' mechanical properties. It is essential to produce parts with minimum residual stress formation for design and production optimization. Therefore, understanding the effects of residual stresses on the laser powder bed fusion process parts is essential to avoid unexpected results. The following conclusions can be gathered from this study;

I. Volumetric energy density (VED), laser power, and exposure time optimization played a crucial role in residual stress minimization for pulsed mode additive manufacturing systems. VED parameter was essential for overall penetration and surface residual stress formation on material with high power and less exposure time within the defined parameter range. On the other hand, point distance and hatch distance had a slight influence when compared with the effect of volumetric energy density, laser power and exposure time within the defined ranges. The as-built parts' residual stresses could be reduced up to ~67% by process parameters optimization. However, the mechanical properties of the materials could be decreased by 14% for tensile strength and 12% for yield strength of a material. Therefore, a trade-

off shall be considered between fewer surface residual stress values and mechanical strength from an engineering perspective.

II. Layer thickness effect investigation on residual stresses was performed with meander scanning strategy. There were slight residual stress changes observed between the specimens produced with 30µm and 60µm meander scanning strategies with defined parameters.

III. Residual stress measurements were performed from the surface to through mid-center of the material by XRD and electropolishing method up to about 300µm depth. Residual stresses on materials slightly increase and then gradually decrease through the mid-center. The surface residual stresses were relatively lower than the very close sub-surface residual stresses due to the open surface area. Having relatively more open surfaces could cause residual stress relief.

IV. The 30-S scanning strategy provided relatively fewer surface residual stress values. Shorter vectorial scanning for the 30-S scanning strategy contributed to less cooling of the specimen and fewer residual stresses accumulated on the 30-S specimen compared to the 30-M specimen. Moreover, having relatively less density also contributed fewer residual stress accumulation by stress relaxation.

V. Experimental residual stress measurements and simulation software results showed similarities, particularly in terms of the trend of residual stress changes. Although the simulation could not be taken into consideration for all pulse mode system properties such as hatch distance and point distance, it provided adequate information for the prediction of the residual stress characteristics and trends. The other important point is that simulation software calibration data provision takes too much time. However, simulation software can be used for residual stress predictions on materials before material production.

VI. Residual stress specimens produced by pulsed mode additive manufacturing systems in as-built condition had more than fifty times surface residual

stresses compared to the control specimen produced from H900 heat treated 17-4 PH stainless steel bar parts compatible with ASTM A564 standard. Control specimen residual stress results indicated the importance of investigating the surface residual stresses of LPBF parts.

VII. As built 30µm meander strategy and 170°C preheated 30µm meander strategy surface residual stresses were almost at the same level because of the austenite by-passing effect.

VIII. Support-used structure residual stress results were lower than the support-free structures, particularly at the lower layers of the specimen. However, the surface residual stresses were still very high compared to the control bar specimen.

IX. EDM separated 30µm meander specimen from the base plate material surface residual stresses were lower than the non-separated 30µm meander specimen. EDM separation causes stress relief on materials. However, the surface residual stresses were still very high compared to the control bar specimen.

X. Production of parts with high accuracy with desired mechanical properties is crucial in the LPBF process. Therefore, increasing the reliability of materials is possible by understanding residual stresses on parts. Within this thesis, the influence of additive manufacturing process parameters on residual stress of 17-4 PH stainless steel parts manufactured by the LPBF process was investigated. Process parameters including scanning strategies, layer thickness, laser power, and exposure time were observed as the critical factors for surface residual stress accumulation on 17-4 PH stainless steel produced by the LPBF process. This study can contribute to the quality control gap of additively manufactured parts to take necessary actions regarding safety factor determination, part production, and post-processes for engineering applications.

XI. While producing highly dense materials with better mechanical properties, residual stress minimization shall be taken into consideration by process parameter optimization in pulsed mode additive manufacturing systems.

Future Term Studies

I. Base plate of Renishaw AM400 was chosen as conventional carbon steel (AISI-1026 / 98% Fe), which is a relatively very cheap material compared to 17-4 PH stainless steel. Since the base materials are consumables for the additive manufacturing process, they are usually chosen from relatively very cheap materials to reduce production costs unless they are detrimental to production. However, residual stress might cause unexpected design failures. Therefore, it might be worth investigating similar and different base material effects on residual stresses for future term studies.

II. Base plate thickness was kept at 20mm±2mm level. The base plate thickness effect on residual stresses might also be examined to determine the limit of the base material thickness range.

III. Modulus of elasticity & Poisson's ratio determination was performed by ultrasonic flaw detector as stated in section 3.5.5. The thickness of the 17-4 PH residual stress specimens was measured by a caliper. A Coordinate Measuring Machine (CMM) or more sensitive measurement equipment can be used for future studies

IV. In this study, standard and similarly characterized powder materials were used. Powder materials were regularly checked by SEM and powder size was measured by Camsizer equipment to minimize the other external effects. However, powder material characteristics particularly size and shape, cause crucial changes in material properties for additive manufacturing in real life. Therefore, the impacts of powder characteristics on residual stresses might be investigated during future term studies.

REFERENCES

[1] W. J. Sames, F. A. List, S. Pannala, R. R. Dehoff, and S. S. Babu, “The metallurgy and processing science of metal additive manufacturing,” *International Materials Reviews*, vol. 61, no. 5, pp. 315–360, Jul. 2016, doi: 10.1080/09506608.2015.1116649.

[2] ISO/ASTM 52900, “Standard Terminology for Additive Manufacturing – General Principles Terminology,” 2015.

[3] D. L. Bourell and T. Wohlers, “Introduction to Additive Manufacturing,” in *Additive Manufacturing Processes*, ASM International, 2020, pp. 3–10. doi: 10.31399/asm.hb.v24.a0006555.

[4] B. Ahuja, M. Karg, and M. Schmidt, “Additive manufacturing in production: challenges and opportunities,” *Laser 3D Manufacturing II*, vol. 9353, no. March, p. 935304, 2015, doi: 10.1117/12.2082521.

[5] B. Blakey-Milner *et al.*, “Metal additive manufacturing in aerospace: A review,” *Mater Des*, vol. 209, Nov. 2021, doi: 10.1016/j.matdes.2021.110008.

[6] F. Kerstens, A. Cervone, and P. Gradl, “End to end process evaluation for additively manufactured liquid rocket engine thrust chambers,” *Acta Astronaut*, vol. 182, pp. 454–465, May 2021, doi: 10.1016/j.actaastro.2021.02.034.

[7] W. E. Frazier, “Metal Additive Manufacturing: A Review,” *J Mater Eng Perform*, vol. 23, no. 6, pp. 1917–1928, Jun. 2014, doi: 10.1007/s11665-014-0958-z.

[8] T. DebRoy *et al.*, “Additive manufacturing of metallic components – Process, structure and properties,” *Progress in Materials Science*, vol. 92.

Elsevier Ltd, pp. 112–224, Mar. 01, 2018. doi: 10.1016/j.pmatsci.2017.10.001.

[9] ISO/ASTM 52910, “Additive manufacturing-Design-Requirements, guidelines and recommendations 1,” 2018, doi: 10.1520/ISO.

[10] X. Wang, M. Jiang, Z. Zhou, J. Gou, and D. Hui, “3D printing of polymer matrix composites: A review and prospective,” *Composites Part B: Engineering*, vol. 110. Elsevier Ltd, pp. 442–458, Feb. 01, 2017. doi: 10.1016/j.compositesb.2016.11.034.

[11] J. Jiang, X. Xu, and J. Stringer, “Support structures for additive manufacturing: A review,” *Journal of Manufacturing and Materials Processing*, vol. 2, no. 4. MDPI, Dec. 01, 2018. doi: 10.3390/jmmp2040064.

[12] X. Peng, L. Kong, J. Y. H. Fuh, and H. Wang, “A review of post-processing technologies in additive manufacturing,” *Journal of Manufacturing and Materials Processing*, vol. 5, no. 2. MDPI AG, Jun. 01, 2021. doi: 10.3390/jmmp5020038.

[13] Q. Portella, M. Chemkhi, and D. Retraint, “Residual Stresses Analysis in AISI 316L Processed by Selective Laser Melting (SLM) Treated by Mechanical Post-Processing Treatments,” *Residual Stresses 2018*, vol. 6, pp. 271–276, 2018, doi: 10.21741/9781945291890-43.

[14] S. Cacace, V. Furlan, R. Sorci, Q. Semeraro, and M. Boccadoro, “Using recycled material to produce gas-atomized metal powders for additive manufacturing processes,” *J Clean Prod*, vol. 268, Sep. 2020, doi: 10.1016/j.jclepro.2020.122218.

[15] A. T. Sutton, C. S. Kriewall, M. C. Leu, and J. W. Newkirk, “Powders for Additive Manufacturing Processes: Characterization Techniques and Effects on Part Properties.”

[16] L. Parry, I. A. Ashcroft, and R. D. Wildman, “Understanding the effect of laser scan strategy on residual stress in selective laser melting through thermo-mechanical simulation,” *Addit Manuf*, vol. 12, pp. 1–15, Oct. 2016, doi: 10.1016/j.addma.2016.05.014.

[17] E. Kundakcıoğlu, I. Lazoglu, Ö. Poyraz, and E. Yasa, “Modeling of residual stress and distortion in direct metal laser sintering process: a fast prediction approach,” *Production Engineering*, May 2022, doi: 10.1007/s11740-022-01135-w.

[18] M. F. Zaeh and G. Branner, “Investigations on residual stresses and deformations in selective laser melting,” *Production Engineering*, vol. 4, no. 1, pp. 35–45, Feb. 2010, doi: 10.1007/s11740-009-0192-y.

[19] X. Song *et al.*, “Advances in additive manufacturing process simulation: Residual stresses and distortion predictions in complex metallic components,” *Mater Des*, vol. 193, p. 108779, 2020, doi: 10.1016/j.matdes.2020.108779.

[20] Z. C. Fang, Z. L. Wu, C. G. Huang, and C. W. Wu, “Review on residual stress in selective laser melting additive manufacturing of alloy parts,” *Optics and Laser Technology*, vol. 129. Elsevier Ltd, Sep. 01, 2020. doi: 10.1016/j.optlastec.2020.106283.

[21] L. Zai *et al.*, “Laser powder bed fusion of precipitation-hardened martensitic stainless steels: A review,” *Metals (Basel)*, vol. 10, no. 2, pp. 1–25, 2020, doi: 10.3390/met10020255.

[22] L. Mugwagwa, I. Yadroitsev, and S. Matope, “Effect of process parameters on residual stresses, distortions, and porosity in selective laser melting of maraging steel 300,” *Metals (Basel)*, vol. 9, no. 10, Oct. 2019, doi: 10.3390/met9101042.

[23] J. Robinson, I. Ashton, P. Fox, E. Jones, and C. Sutcliffe, “Determination of the effect of scan strategy on residual stress in laser powder bed fusion

additive manufacturing," *Addit Manuf*, vol. 23, pp. 13–24, Oct. 2018, doi: 10.1016/j.addma.2018.07.001.

[24] A. Ozsoy, E. Yasa, M. Keles, and E. B. Tureyen, "Pulsed-mode Selective Laser Melting of 17-4 PH stainless steel: Effect of laser parameters on density and mechanical properties," *J Manuf Process*, vol. 68, pp. 910–922, Aug. 2021, doi: 10.1016/j.jmapro.2021.06.017.

[25] J. P. Oliveira, A. D. LaLonde, and J. Ma, "Processing parameters in laser powder bed fusion metal additive manufacturing," *Mater Des*, vol. 193, Aug. 2020, doi: 10.1016/j.matdes.2020.108762.

[26] A. American and N. Standard, "Renishaw PLC, AM250/AM400 Reduced Build Volume User Guide, (2017).".

[27] T. Simson, A. Emmel, A. Dwars, and J. Böhm, "Residual stress measurements on AISI 316L samples manufactured by selective laser melting," *Addit Manuf*, vol. 17, pp. 183–189, Oct. 2017, doi: 10.1016/j.addma.2017.07.007.

[28] A. R. Balachandramurthi, J. Moverare, S. Mahade, and R. Pederson, "Additive manufacturing of alloy 718 via electron beam melting: Effect of post-treatment on the microstructure and the mechanical properties," *Materials*, vol. 12, no. 1, Dec. 2018, doi: 10.3390/ma12010068.

[29] W. Chen, L. Xu, Y. Han, L. Zhao, and H. Jing, "Control of residual stress in metal additive manufacturing by low-temperature solid-state phase transformation: An experimental and numerical study," *Addit Manuf*, vol. 42, no. September 2020, p. 102016, 2021, doi: 10.1016/j.addma.2021.102016.

[30] M. Li, W. Du, A. Elwany, Z. Pei, and C. Ma, "Metal binder jetting additive manufacturing: A literature review," *Journal of Manufacturing Science and Engineering, Transactions of the ASME*, vol. 142, no. 9. American Society of Mechanical Engineers (ASME), Sep. 01, 2020. doi: 10.1115/1.4047430.

[31] C. Suwanpreecha and A. Manonukul, “A Review on Material Extrusion Additive Manufacturing of Metal and How It Compares with Metal Injection Moulding,” *Metals (Basel)*, vol. 12, no. 3, p. 429, Feb. 2022, doi: 10.3390/met12030429.

[32] K. Jimbo and T. Tateno, “Shape contraction in sintering of 3d objects fabricated via metal material extrusion in additive manufacturing,” *International Journal of Automation Technology*, vol. 13, no. 3, pp. 354–360, May 2019, doi: 10.20965/ijat.2019.p0354.

[33] Y. Zhang *et al.*, “Additive Manufacturing of Metallic Materials: A Review,” *Journal of Materials Engineering and Performance*, vol. 27, no. 1. Springer New York LLC, Jan. 01, 2018. doi: 10.1007/s11665-017-2747-y.

[34] K. H. Lo, C. H. Shek, and J. K. L. Lai, “Recent developments in stainless steels,” *Materials Science and Engineering R: Reports*, vol. 65, no. 4–6. Elsevier BV, pp. 39–104, May 29, 2009. doi: 10.1016/j.mser.2009.03.001.

[35] Bhabha, “Stress corrosion cracking (SCC) in stainless steels.”

[36] G. Aggen *et al.*, “ASM Handbook, Volume 1, Properties and Selection: Irons, Steels, and High Performance Alloys Section: Publication Information and Contributors Publication Information and Contributors Authors and Reviewers,” 2005.

[37] S. Patra, A. Agrawal, A. Mandal, and A. S. Podder, “Characteristics and Manufacturability of Duplex Stainless Steel: A Review,” *Transactions of the Indian Institute of Metals*, vol. 74, no. 5, pp. 1089–1098, May 2021, doi: 10.1007/s12666-021-02278-7.

[38] A. Sathyanath and A. Meena, “Microstructural evolution and strain hardening behavior of heat-treated 17-4 PH stainless steel,” *Mater Today Commun*, vol. 25, no. December 2019, p. 101416, 2020, doi: 10.1016/j.mtcomm.2020.101416.

[39] J. Nowacki, “Weldability of 17-4 PH stainless steel in centrifugal compressor impeller applications,” *J Mater Process Technol*, vol. 157–158, no. SPEC. ISS., pp. 578–583, 2004, doi: 10.1016/j.jmatprotec.2004.07.117.

[40] H. G. The Graduate Engineer, “Three Stages of Precipitation Hardening”, Accessed: Jul. 31, 2022. [Online]. Available: https://thegraduateengineer.com/precipitation-hardening/

[41] C. N. Hsiao, C. S. Chiou, and J. R. Yang, “Aging reactions in a 17-4 PH stainless steel,” 2002.

[42] ASTM A-564M, “Standard Specification for Hot-Rolled and Cold-Finished Age-Hardening Stainless Steel Bars and Shapes 1,” *ASTM International*, 2013, doi: 10.1520/A0564_A0564M-10.

[43] M. Mahmoudi, A. Elwany, A. Yadollahi, S. M. Thompson, L. Bian, and N. Shamsaei, “Mechanical properties and microstructural characterization of selective laser melted 17-4 PH stainless steel,” *Rapid Prototyp J*, vol. 23, no. 2, pp. 280–294, 2017, doi: 10.1108/RPJ-12-2015-0192.

[44] J. L. Bartlett and X. Li, “An overview of residual stresses in metal powder bed fusion,” *Additive Manufacturing*, vol. 27. Elsevier B.V., pp. 131–149, May 01, 2019. doi: 10.1016/j.addma.2019.02.020.

[45] M. Schmidt *et al.*, “Laser based additive manufacturing in industry and academia,” *CIRP Annals*, vol. 66, no. 2, pp. 561–583, 2017, doi: 10.1016/j.cirp.2017.05.011.

[46] P. Mercelis and J. P. Kruth, “Residual stresses in selective laser sintering and selective laser melting,” *Rapid Prototyp J*, vol. 12, no. 5, pp. 254–265, 2006, doi: 10.1108/13552540610707013.

[47] R. Cottam, J. Wang, and V. Luzin, “Characterization of microstructure and residual stress in a 3D H13 tool steel component produced by additive

manufacturing," *J Mater Res*, vol. 29, no. 17, pp. 1978–1986, Jun. 2014, doi: 10.1557/jmr.2014.190.

[48] L. Parry, I. Ashcroft, D. Bracket, and R. D. Wildman, "Investigation of residual stresses in selective laser melting," in *Key Engineering Materials*, 2015, vol. 627, pp. 129–132. doi: 10.4028/www.scientific.net/KEM.627.129.

[49] W. Chen *et al.*, "Microscale residual stresses in additively manufactured stainless steel," *Nat Commun*, vol. 10, no. 1, Dec. 2019, doi: 10.1038/s41467-019-12265-8.

[50] G. M. Karthik and H. S. Kim, "Heterogeneous Aspects of Additive Manufactured Metallic Parts: A Review," *Metals and Materials International*, vol. 27, no. 1. Korean Institute of Metals and Materials, Jan. 01, 2021. doi: 10.1007/s12540-020-00931-2.

[51] P. Aggarangsi and J. L. Beuth, "Localized Preheating Approaches for Reducing Residual Stress in Additive Manufacturing," 2006. [Online]. Available: https://www.researchgate.net/publication/268402375

[52] D. D. Gu, W. Meiners, K. Wissenbach, and R. Poprawe, "Laser additive manufacturing of metallic components: Materials, processes and mechanisms," *International Materials Reviews*, vol. 57, no. 3, pp. 133–164, May 2012, doi: 10.1179/1743280411Y.0000000014.

[53] J. L. Bartlett, B. P. Croom, J. Burdick, D. Henkel, and X. Li, "Revealing mechanisms of residual stress development in additive manufacturing via digital image correlation," *Addit Manuf*, vol. 22, no. March, pp. 1–12, 2018, doi: 10.1016/j.addma.2018.04.025.

[54] A. S. Wu, D. W. Brown, M. Kumar, G. F. Gallegos, and W. E. King, "An Experimental Investigation into Additive Manufacturing-Induced Residual Stresses in 316L Stainless Steel," *Metall Mater Trans A Phys Metall Mater*

Sci, vol. 45, no. 13, pp. 6260–6270, Oct. 2014, doi: 10.1007/s11661-014-2549-x.

[55] J. Song *et al.*, "Role of scanning strategy on residual stress distribution in Ti-6Al-4V alloy prepared by selective laser melting," *Optik (Stuttg)*, vol. 170, pp. 342–352, Oct. 2018, doi: 10.1016/j.ijleo.2018.05.128.

[56] L. A. Parry, I. A. Ashcroft, and R. D. Wildman, "Geometrical effects on residual stress in selective laser melting," *Addit Manuf*, vol. 25, pp. 166–175, Jan. 2019, doi: 10.1016/j.addma.2018.09.026.

[57] L. Mugwagwa, D. Dimitrov, S. Matope, and I. Yadroitsev, "Influence of process parameters on residual stress related distortions in selective laser melting," in *Procedia Manufacturing*, 2018, vol. 21, pp. 92–99. doi: 10.1016/j.promfg.2018.02.099.

[58] M. Masoomi *et al.*, "Residual stress measurements via neutron diffraction of additive manufactured stainless steel 17-4 PH," 2017, doi: 10.7910/DVN/T41S3V.

[59] M. Leitner, W. Schneller, S. Springer, and F. Grün, "Effect of Surface Layer on the Fatigue Strength of Selectively Laser Melted 17-4 PH Steel," *J Mater Eng Perform*, vol. 30, no. 7, pp. 5383–5391, Jul. 2021, doi: 10.1007/s11665-021-05705-4.

[60] A. Hemmasian Ettefagh, S. Guo, and J. Raush, "Corrosion performance of additively manufactured stainless steel parts: A review," *Additive Manufacturing*, vol. 37. Elsevier B.V., Jan. 01, 2021. doi: 10.1016/j.addma.2020.101689.

[61] B. Vrancken, "Study of Residual Stresses in Selective Laser Melting," 2016.

[62] C. Li, Z. Y. Liu, X. Y. Fang, and Y. B. Guo, "Residual Stress in Metal Additive Manufacturing," in *Procedia CIRP*, 2018, vol. 71, pp. 348–353. doi: 10.1016/j.procir.2018.05.039.

[63] S. Marola *et al.*, “Residual stresses in additively manufactured AlSi10Mg: Raman spectroscopy and X-ray diffraction analysis,” *Mater Des*, vol. 202, p. 109550, 2021, doi: 10.1016/j.matdes.2021.109550.

[64] M. E. Fitzpatrick, A. T. Fry, and P. Holdway, “Determination of Residual Stresses by X-ray Diffraction Metrosion View project Supersonic aircraft fatigue life extension with compressive residual stress and creep stress relaxation View project Fayez Kandil,” 2002. [Online]. Available: https://www.researchgate.net/publication/42795493

[65] J. GUO, H. FU, B. PAN, and R. KANG, “Recent progress of residual stress measurement methods: A review,” *Chinese Journal of Aeronautics*, vol. 34, no. 2. Elsevier B.V., pp. 54–78, Feb. 01, 2021. doi: 10.1016/j.cja.2019.10.010.

[66] G. S. Schajer, *PRACTICAL RESIDUAL STRESS MEASUREMENT METHODS Edited by*. 2013. [Online]. Available: www.wiley.com.

[67] V. I. Mikla, V. I. Rusin, and P. A. Boldizhar, “Advances in imaging from the first X-Ray images,” *Journal of Optoelectronics and Advanced Materials*, vol. 14, no. 7–8, pp. 559–570, 2012, doi: 10.1016/b978-0-12-417021-6.00001-0.

[68] A. American and N. Standard, “ASTM E915 Standard Test Method for Verifying the Alignment of X-Ray Diffraction Instrumentation for Residual Stress Measurement.” [Online]. Available: www.astm.org

[69] “Metallic Materials Properties Development and Standardization-16 (MMPDS-16) 17-4 PH Stainless Steel Material Data page 2-258”.

[70] A. American and N. Standard, “ASTM E 1417-99 Standard Practice for Liquid Penetrant Examination.”

[71] A. American and N. Standard, “ASTM B 311 Test Method for Density Determination for Powder Metallurgy (P/M) Materials Containing Less Than Two Percent Porosity.”

[72] A. American and N. Standard, “ASTM E407 Standard Practice for Microetching Metals and Alloys.”

[73] A. American and N. Standard, “ASTM E 92 Standard Test Method for Vickers Hardness of Metallic Materials.”

[74] A. American and N. Standard, “ASTM E 140 Standard Hardness Conversion Tables for Metals Relationship Among Brinell Hardness Vickers Hardness, Rockwell Hardness, Superficial Hardness, Knoop Hardness, and Scleroscope Hardness.”

[75] A. American and N. Standard, “ASTM E-8m Standard Test Methods for Tension Testing of Metallic Materials”.

[76] A. N. Olympus Industrial Resources, “Elastic Modulus Measurement”, Accessed: Jul. 24, 2022. [Online]. Available: https://www.olympus-ims.com/en/applications/elastic-modulus-measurement/

[77] M. Alnajjar, F. Christien, K. Wolski, and C. Bosch, “Evidence of austenite by-passing in a stainless steel obtained from laser melting additive manufacturing,” *Addit Manuf*, vol. 25, pp. 187–195, Jan. 2019, doi: 10.1016/j.addma.2018.11.004.

[78] C. U. Brown and M. A. A. Donmez, “Microstructure Analysis for Additive Manufacturing: A Review of Existing Standards,” Gaithersburg, MD, Sep. 2016. doi: 10.6028/NIST.AMS.100-3.

[79] A. American and N. Standard, “ASTM E 1417 Standard Liquid Penetrant Examination.”